Industry/University Research Center

NEUP – Final Report

August 2017

Advance High Temperature Inspection Capabilities for Small Modular Reactors: Part 1 - Ultrasonics

Leonard J Bond, Prathamesh Bilgundi and John R Bowler

Program RCD&D: Instrumentation, Control Human Machine Interface

Nuclear Energy University Program – Project # RPA-13-5150

U.S. Department of Energy

CENTER for NONDESTRUCTIVE EVALUATION
IOWA STATE UNIVERSITY

Applied Sciences Complex II 1915
Scholl Road

Ames, IA 50011-3042

515-294-8152

EXECUTIVE SUMMARY

The project objective was to investigate the development non-destructive evaluation techniques for advanced small modular reactors (aSMR), where the research sought to provide key enabling inspection technologies needed to support the design and maintenance of reactor component performance.

The project tasks for the development of inspection techniques to be applied to small modular reactor are being addressed through two related activities. The first is focused on high temperature ultrasonic transducers development (this report Part 1) and the second is focused on an advanced eddy current inspection capability (Part 2). For both inspection techniques the primary aim is to develop in-service inspection techniques that can be carried out under standby condition in a fast reactor at a temperature of approximately 250°C in the presence of liquid sodium.

The piezoelectric material and the bonding between layers have been recognized as key factors fundamental for development of robust ultrasonic transducers. Dielectric constant characterization of bismuth scantanate-lead titanate ($(1\text{-}x)BiScO_3\text{-}xPbTiO_3$) (BS-PT) has shown a high Curie temperature in excess of 450°C , suitable for hot stand-by inspection in liquid metal reactors. High temperature pulse-echo contact measurements have been performed with BS-PT bonded to 12.5 mm thick 1018-low carbon steel plate from 20C up to 260 C. High temperature air-backed immersion transducers have been developed with BS-PT, high temperature epoxy and quarter wavlength nickel plate, needed for wetting ability in liquid sodium. Ultrasonic immersion measurements have been performed in water up to 92C and in silicone oil up to 140C. Physics based models have been validated with room temperature experimental data with benchmark artifical defects.

A novel model assisted probabilty of detection (MAPOD) apporach has been demonstrated to estimate high temperature POD using room temperature experimental data considering a soft piezoelectric material (low Curie temperature) to estimate uncertainity. A significant reduction in POD is predicted for a flaw size equaling two wavelengths in steel at 2.25 MHz. This reduction is due the temperature sensitivity of the material coefficients of the piezoelectric which have been quantified in this project. Hence, using only the room temperature experimental data and temperature dependent material properties, the MAPOD approach connects the microscopic material phenomenon ocurring in piezoelectric ceramics at high temperature to an industrial practice of evaluation of POD.

New insights into the causes of non-ideal performance in a research transducer developed at PNNL, which has limited S:N were obtained. The importance of boundary (interface layers) and interfaces on transducers were highlighted and causes of non-ideal performance quantified. It was found that d_{33} is an inadequate metric for use in predicting tranbsducer performance and making material selection. The full matrix of material properties is needed. The new material BS-PT offers enhanced performance and this material should be considered in an air-backed transducer design. A methodology was developed and is reported for prediction of temperature effects on reduction of POD at elevated temperature.

The eddy current activities are reported in Part 2 of this final report. A fundamental limiting factor of eddy current inspection in fast reactor conditions is the extent to which the eddy current signal is reduced when the inspection takes place under liquid metal. As a surrogate for liquid sodium at a stand-by temperature of 250°C a gallium-indium-tin mixture was used at room temperature. Eddy current inspection at 250° is not expected to present a major problem since on site industrial inspections up to 400°C are performed. Repeat experiments were performed to determine the signal variation with probe lift-off and determined probability of detection (PoD) data from the measurements. Further tests enabled PoD estimates that include a combination of flaw size and lift-off variations. Typically, the signal level is reduced by an order of magnitude when an inspection takes place in immersion conditions using standard coil inspection, the probe lift-off being a critical parameter due to absorption of the electromagnetic field in the coolant.

Tradition heat exchange tube eddy current inspections are performed in order that a reactor is off-line for a short period. However a similar inspection with probes immersed in liquid metal are likely to take a longer time and require close coupling with the tube wall to reduce signal attenuation in the coolant. Measurements with small ferrite cored probes at the surface produce the best performance and to speed up the inspection process these could be used in arrays to reduce inspection times.

This document provides Part 1, ultrasonics, of the final report on the NEUP project on Advanced High Temperature Inspection Capabilities for advanced Small Modular Reactors, that was performed at Iowa State University. Further discussion of the topics, and some additional material will be found in the PhD thesis currently being prepared by Prathamesh Bilgundi, which is expected to be submitted by May 2018.

CONTENTS

Executive Summary

1. Introduction

Generation IV fast nuclear reactors are under development to support sustainable development, economic competitiveness and improve safety (OECD, 2014). In considering liquid sodium cooled reactors past experience, specifically, with regard to long term maintenance experience from the Phoenix reactors (France) has underlined the need to provide effective and reliable inspection of components in any proposed advanced liquid metal cooled small modular, and other advanced reactors (CEA, 2012). In the 1970s, the Hanford Engineering Development Laboratory (HEDL), Richland, Washington (Day and Smith, 1973) developed high temperature transducers using lead zirconium titanate (PZT). This technological capability in the USA was subsequently lost. Studies by Griffin et al. (2012) sought to re-establish this capability and they found that the new high temperature transducers which they developed could operate continuously at about 250^{o}C for 8 hours, but the transducers had a limited signal to noise ratio [Griffin et al. (2012)]. In reviewing more recent studies and in assessing the state-of-the-art there have been recent publications on the selection of piezoelectric material and backing materials for high temperature ultrasonic transducer applications [Lee et al (2013) and Zhang and Fapeng (2011)]. These studies consisted of mainly experimental work which presents challenges in terms of cost, time and ability to investigate the effects of design and material variables, particularly with the need for facilities to operate at high temperature.

The applications of ultrasonic transducers in high temperature and harsh environment is expanding rapidly in the nuclear power industry, for gas turbines and space exploration technology [Bar-Cohen et al. (2015), Lee et al. (2015), Parks et al (2013, 2014), Augereau, et al. (2008), and Kažys (2008)]. These electromechanical sensors play an important role in the performance, efficiency and estimating life extension of critical infrastructure by providing a structural health insight through an ultrasonic scan (Searfass,2016).

A pulse-echo ultrasonic non-destructive testing (NDT) system using longitudinal waves in high temperature liquid media (water, liquid metal or a molten salt) has been proposed for inspection in advanced small modular reactors [Griffin et al (2012), Bond et al. (2012)]. In the past many authors have studied the piezoelectric materials and their performance parameters at high temperature [Bond, et al. (2012), Kazys et al. (2008)]. To validate such methods experiments were performed in a liquid metal at temperature (~250C) which are both experimentally challenging and expensive. To provide greater insight into the transducer performance and to reduce the cost of experimental verification a modeling approach can be adopted.

During the past 40 years, extensive experimental work on high temperature (HT) ultrasonic transducer has been reported, but many transducers demonstrated limits to performance and life [Griffin (2009)]. The metric used in material selection and for monitoring of the transducer performance with aging/operation has been limited to measurement of d_{33} of the piezoelectric material as a function of temperature. This is found to be an inadequate parameter to consider if performance is to be correctly predicted.

The fundamental questions for use of ultrasonics in an advanced SMR's relate to piezoelectric materials properties in ultrasonic transducer and the properties of materials used in eddy current probes and the designs of the sensors in which they are utilized. The sensors then interact with acoustic noise, electromagnetic fields, and the effects of elevated temperature on the materials used in sensors fully immersed in the coolants. The study was structured to understand the limitations of the high temperature performance of piezoelectric materials and components of eddy-current sensors in liquid metals (~250C) and lower conductivity fluids (including molten salts ~600C), with analysis of potential sensitivity and S:N.

The primary objective of this project was to investigate fundamental limitations and to provide proof of concept for NDE techniques and sensor technologies for advanced small modular reactors (aSMR's) employing novel ultrasound (Part 1) and eddy currents (Part 2) approaches which enable in-coolant deployment of probes. The project combined modeling and laboratory experiments to analyze and understand the phenomena that limit sensor performance. The project is also sought to use modeling and laboratory measurements to enable identification and assessment of performance for potential in-service inspection capabilities.

A parametric study for the effect of temperature on ultrasonic transduction is reported in Section 2. Issues found that relate to acoustic cross-talk in piezoelectric based ultrasonic transducers is considered in Section 3. Alternate element materials were considered with an investigation into development of a BS-PT based high temperature transducer, reported in Section 4. Aging and thermal degradation of interfaces was investigated with high temperature in-situ ultrasonic measurements up to 260C for multiple thermal cycles in Section 5. The challenges faced with high temperature ultrasonic immersion measurements using BS-PT based ultrasonic transducer without a delay line are reported in Section 6. A model assisted approach for probability of detection (POD) that enables temperature effects on POD to be estimated is covered in Section 7.

2. Parametric study for the effect of temperature on ultrasonic transduction

The ultrasonic aspects of the current study have been focused on analysis of the transducer designs, including using finite element modelling of the temperature effects in transducers, specifically using data for PZT-5A and also addressing de-bonding phenomenon caused by the thermal expansion at high temperatures. This study employed a combination of models, and experiments to investigate the limits of performance for ultrasonic transducers fully immersed in coolants.

An ultrasonic transducer is comprised of a piezoelectric element, combined with a front face matching layer and the backing, which are bonded together by either a high temperature solder, braze or adhesive. In transmission process, the piezoelectric element converts an electric signal into mechanical motion and when receiving deformation is converted into an electrical signal.

During the project this aspect of the study has mainly concentrated on quantifying the effects of changes in material properties of PZT-5A on the strength of the signal. This involves the effect of temperature variation on the elastic, dielectric and piezoelectric constants and thus on the ultrasonic is signal which is analyzed as the temperature depended problem illustrated in Fig 2.1. Finally, a complete material matrix is simultaneously simulated to observe the effects on the amplitude of the signal when the temperature of liquid sodium is increased from 100 to 200C. Moreover, the attenuation due to the temperature dependent variation of the thermo-physical properties of liquid sodium is simulated and analyzed. Finally, a simplified model of the de-bonding due to thermal expansion is used to investigate the difference between the de-bonding effect and that due to combining piezoelectric material changes with temperature and de-bonding. Finally, initial pulse echo experimental results obtained with PNNL transducer are given.

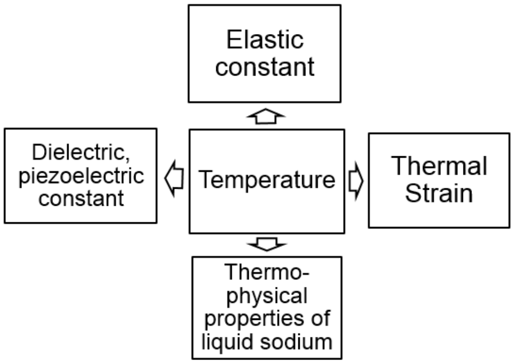

Figure 2.1 Temperature dependent problem

2.1 Finite element model

The initial ultrasonic model used a finite element method for modelling the piezoelectric transducer for application in liquid coupled systems. The model was initially validated against data from room temperature experiments using data for coolant surrogates which, in the initial case was water. For simulating the wave propagation phenomenon, it is necessary to resolve the shortest wavelength and hence the highest frequency in the spectrum. This requires consideration of the maximum element size to be used in the meshing and time step needed to give convergence, while still having models that can be run in a reasonable time.

The model was based on a two-dimensional finite element method implemented using a commercially available package (COMSOL) and solved to give the dynamic equilibrium in the time domain. Three cases were investigated (i) response of a side drilled hole in an aluminum block, (ii) wave propagation in water and (iii) waves in a water-aluminum system. In the past, many authors have studied modelling using absorbing boundary conditions to reduce computational grid size. A brief activity was undertaken to investigate various formulations. Model results for the three geometries were validated with the experimental data [Bilgunde and Bond (2015)].

The accuracy of the finite element model depends upon the constitutive equations of the models, material properties and discretization of the model. The current work considered the piezoelectric device and the wave field with a pressure acoustics module in COMSOL. In this section, the governing equations for these two models are presented.

2.1.1 Constitutive equations: piezoelectric finite elements

Several authors have reported use of a finite element method to model a piezoelectric transducer and measure the performance parameters [Lerch, (1990), Abboud et al. (1998)]. In the piezoelectric device, the governing matrix equation relating to mechanical and electrical quantitates are given by:

$$T = c^{E} S + eE \tag{2.1}$$

$$D = eS + \varepsilon^{s} E \tag{2.2}$$

where T is mechanical stress, c^{E} is the elastic stiffness matrix under constant electric field, S is the mechanical strain, e is piezoelectric stress constant, E is the electric field, D is the electric displacement and ε^{s} is the is the electrical permittivity under constant strain S. This form of equation is called stress-charge equation which has been implemented in this model. The piezoelectric device can also be modelled using strain-charge equations given by:

$$S = S^{E} T + dE \tag{2.3}$$

$$D = dT + \varepsilon^{T} E \tag{2.4}$$

where S^{E} is the mechanical strain under constant mechanical stress T, d is the piezoelectric constant, ε^{T} is the electrical permittivity under constant mechanical stress. During analysis, the mechanical displacement and electric potential are calculated at each nodal point in the piezoelectric device interface. Moreover, it is necessary to describe the continuity for displacement and electric field using polynomial interpolation functions. (Lerch, 1990). Hence, to obtain the discrete finite element equation system a variation principle is applied to equations (2.1) and (2.2), to give [Medina et al. (2006)]:

$$\left[M_{uu}^{e}\right]\frac{\partial^2 u}{\partial t^2}^{e}+\left[C_{uu}^{e}\right]\frac{\partial u}{\partial t}^{e}+\left[K_{uu}^{e}\right]u^{e}+\left[K_{u\phi}^{e}\right]\phi^{e}=F^{e} \tag{2.5}$$

$$\left[K_{u\phi}^{e}\right]u^{e}+\left[K_{\phi\phi}^{e}\right]\phi^{e}=Q^{e} \tag{2.6}$$

where u^e is the mechanical displacement vector, ϕ^e is the electric potential vector, F^e is the mechanical force vector and Q^e is the electric charge vector for each element defined in the piezoelectric device, M_{uu}^{e} is the mass matrix , C_{uu}^{e} is the mechanical damping matrix , K_{uu}^{e} is the mechanical stiffness matrix , $K_{\phi\phi}^{e}$ is the di-electric matrix, $K_{u\phi}^{e}$ is the piezoelectric coupling matrix.

These are terms are completely defined by Lerch, (1990). The complete solution of the response of the piezoelectric elements can then be obtained by solving a set of linear algebraic equations with a symmetric band structure. The values of u, ϕ ,F and Q are the globally assembled field quantities.

Mechanical damping plays an important role in the dynamic response, attenuation of vibration and hence radiated acoustic waveform [Medina (2006)]. Rayleigh Damping can be applied to the time domain and it assumes that the damping matrix C_{uu}^{e} is the linear combination of the mass matrix and mechanical stiffness matrix as defined in equations 2.5 and 2.6. This can be represented as:

$$[C_{uu}]=\alpha[M_{uu}]+\beta[K_{uu}] \tag{2.7}$$

where α and β are the Rayleigh constants for the mass and stiffness matrix respectively. In the current model, viscous damping is considered in which $\alpha=0$ and $\beta>0$. Moreover, the backing material, matching layer and insulating case and steel outer body casing have been assigned nodes where the response is that for a linear elastic material with Rayleigh damping coefficients in the computation model. For these linear elastic materials, the piezoelectric coupling matrix [$K_{u\phi}^{e}$] becomes a null matrix (Abboud et al, 1998) and hence there does not exist any coupling between mechanical force vector and electric charge vector as defined in equations 2.5 and 2.6. As a result, the computational model distinguishes the piezoelectric element from the other materials used and the piezoelectric effect is only applied to this material.

2.1.2 Finite element modeling of wave propagation in fluid

Acoustic problems in COMSOL involve solving for the small acoustic pressure variations p which vary about the nominal static pressure p_0. Mathematically, this represents a linearization (small parameter expansion) of the dependent variables around the stationary quiescent values [COMSOL (2014)]. The governing equations for these problems are the momentum conservation equation (Euler's equation) and the mass conservation equation (continuity equation). In acoustics all processes are assumed to be reversible adiabatic (isentropic). Thus, the medium for wave propagating in the current model is a lossless fluid medium. The governing equation for the acoustics transient analysis problem is given by:

$$\frac{1}{\rho c^2}\frac{\partial^2 p}{\partial t^2}+\nabla\left(\frac{-1}{\rho}\left(\nabla P_t - q_d\right)\right)=Q_m \tag{2.8}$$

$$\nabla P_t = P + P_b \tag{2.9}$$

$$\rho\frac{\partial^2 u}{\partial t^2}-\nabla.T = F_v \tag{2.10}$$

where ρ is the density of the wave propagating medium, c is the speed of sound in the medium, P_b is the gauge pressure , q_d is dipole source, Q_m is the monopole acoustic source [COMSOL (2014)] and F_v is the body force per unit volume. The term ρc^2 represents the bulk modulus of the fluid. The acoustic model consists of the medium for wave propagation and the scattering which is coupled with the piezoelectric device to generate and receive the transmitted wave and reflected signals. The coupling in this case plays an important role which will be discussed later in the boundary condition section.

2.1.3 Material model and Geometric configuration

The piezoelectric material PZT 5A is used as the active element in the transducer. The material properties can be found in the COMSOL user guide and material library [COMSOL (2014)]. The backing material for the piezoelectric element is epoxy loaded with tungsten powder and the front face matching layer consists of a quarter wavelength of epoxy. The insulating layer is nylon and the outer casing is made of stainless steel. Properties for these materials have been given by [Medina (2006)] and are shown in Table 2.1.

Table 2.1. Material properties used in FE model.

Material	Density (Kg/m^3)	Poison Ratio	Elasticity module(N/m^2)	β damping
Araldite	1096	0.34	0.55e10	2.3e-8
Araldite/Tungsten	5766	0.34	1.05e10	1.5e-8
Nylon	1405	0.27	0.74e10	5e-9
Steel	7890	0.29	26.51e10	10e-8

The CAD model was built using the COMSOL geometry build-up tool. There were three cases modelled as shown below in Figure 2.2: (a) the case of a transducer with waves in a solid with a side drilled hole, (b) the case a transducer generating waves in a fluid and (c) the case of a transducer generating waves propagating into fluid-solid media.

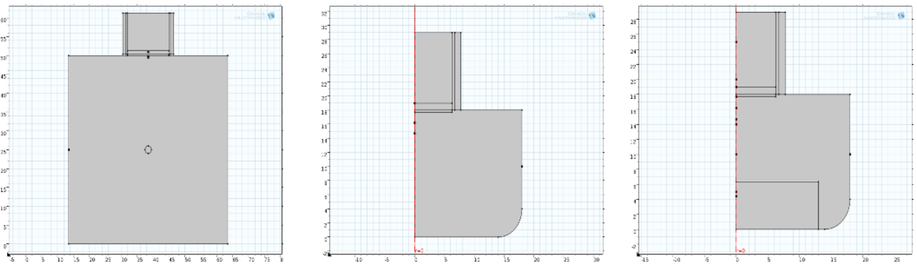

Figure 2.2 a) Waves in Aluminum block b) in water c) in Water-Aluminum

The models include the piezoelectric interface and pressure acoustics interface as shown below:

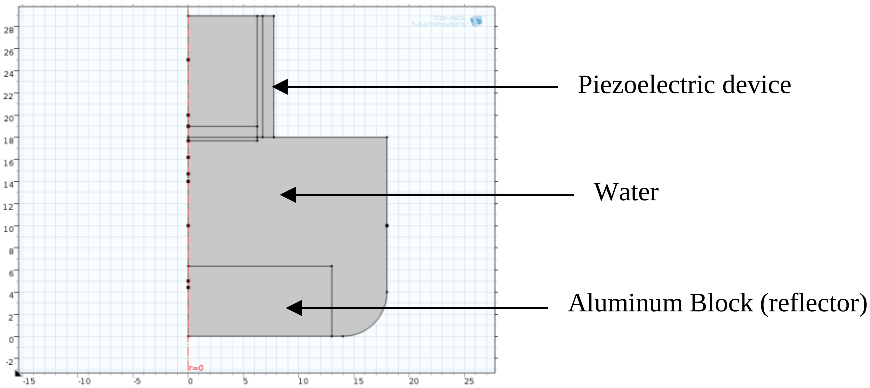

Figure 2.3 Geometric configuration of the model

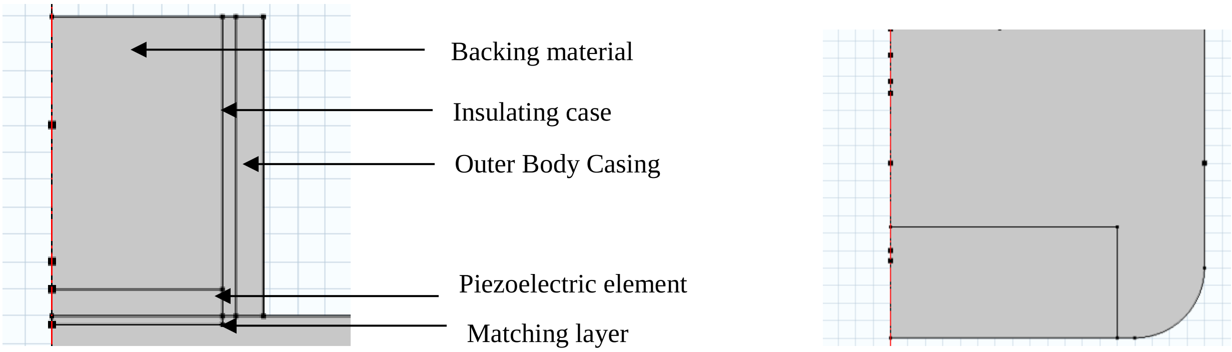

Figure 2.4 Finite element models:
a) Solid mechanics Module *b) Pressure acoustics module*

2.1.4 Boundary Conditions

It is necessary to couple the piezoelectric (PZT) interface with the acoustics model to obtain the generation of waves and the radiation pattern. It is also required that the transducer model accurately simulates both the transmission and reception of the waves. This is made possible by applying boundary load in given in COMSOL “PZD physics” at a boundary common to both interfaces. The same boundary is assigned normal acceleration in the acoustics model.

The acoustic analysis provides the acoustic load to structural coupling and the structural coupling provides acceleration to the acoustic analysis. This interface couples the fundamental physics between the two media in the model. When the case of wave propagation into a solid (case-1) is considered the boundary conditions are different. The boundary shared by the two physics modules in the code is a boundary between media in a solid state. Hence, continuity in the displacement field is required. The models for cases 2 and 3 are two dimensional axial symmetric for which axial symmetry is defined. A floating potential node is defined to give a pulse to the piezoelectric element and receive the echo response. A zero charge node is defined for the boundary with zero charge density. A rigid boundary node has been assigned to boundaries at which normal acceleration is required to be zero [COMSOL (2014)]. Waves reflecting from the side boundaries of the model increase the degrees of freedom [Prozdz (2008)]. Hence as the domain size (grid/element numbers) increases the model becomes computationally more expensive and solution time increases. Absorbing boundaries can be used to reduce edge reflections by allowing the outgoing wave to leave the computational domain with minimum reflection. This is necessary for the well posed solution of the partial differential equations. In a COMSOL model, in the time domain, this can be achieved by using either cylindrical or and spherical wave radiation nodes.

The effect of absorbing boundaries can be shown as follows. Although not perfect Figures 2.5(a) and (b) clearly show the differences in time domain signals seen for the cases of using a boundary with and without the absorbing layer.

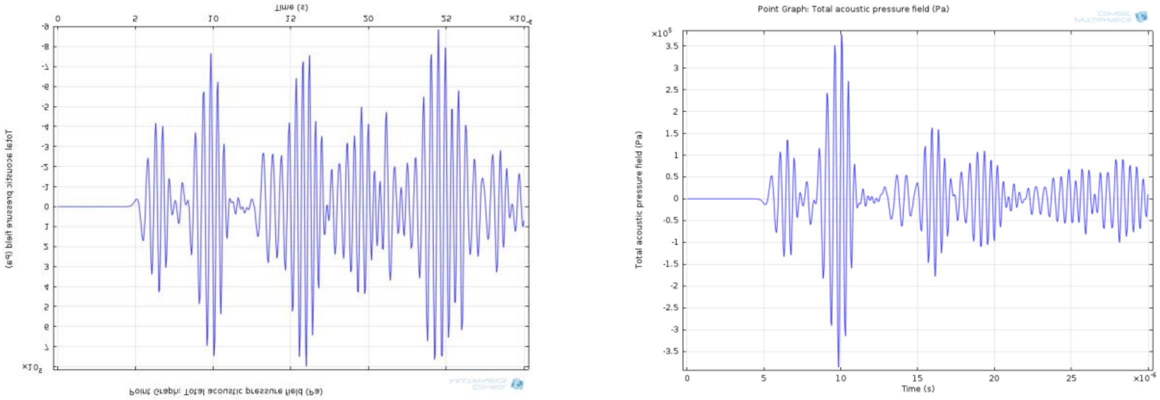

Figure 2.5 FE Model

a)Waveform without absorbing boundaries *b) With absorbing boundaries*

2.1.5 Discretization

For the FE wave propagation model it is important to resolve the shortest wavelength and hence the highest frequency in the spectrum. A second order triangular Lagrange element is used for meshing in COMSOL. For a structured mesh the average resolution differs significantly between the direction parallel to grid lines and directions rotated 45^0 to one of the axes. More importantly, the direction of wave propagation is not known in advance. Hence, an unstructured type of mesh is used instead of structured mesh. The maximum element size in the mesh can be given by [Bilgunde and Bond (2015)]:

$$h = \frac{c}{F_0 N} = \frac{\lambda}{N} \tag{2.11}$$

where

h=maximum element size (m)
c=speed of sound in wave propagating medium
F_0=Highest frequency in the spectrum (Hz)
λ= wavelength of medium
N= number of elements per wavelength

In addition to spatial discretization the temporal discretization is also important for the stability of the numerical model and hence the convergence of the solution. In COMSOL time dependent problems by default use an implicit time method to solve the partial differential equations. Generalized-α [Chung and Hulbert (2000), Jenset et al. (2000)] is the implicit method used in which α parameter controls the numerical dissipation at higher frequencies. It provides relatively less damping as compared to the Backward Differentiation Formula (BDF) which is found to severely dampen higher frequencies [COMSOL (2014)]. The degree of damping can inversely affect the accuracy of the solution at the higher frequencies. The absolute and relative tolerances defined in COMSOL control the error at each integration step. Moreover, for the stability of algorithm in the Generalized-α method, it is necessary for the error growth rate to be constant. This can be achieved by ensuring that space and time steps conform to the CFL number [Courant et al. (1928)] for time step as shown:

$$CFL = \frac{c\Delta t}{h} \tag{2.12}$$

where Δt is the time step (sec), c and h is are defined in equation (2.11).
Hence the time step can be defined as

$$\Delta t = \frac{c * CFL}{h} \tag{2.13}$$

where $0<\mathrm{CFL}\leq 1$

For stability of the algorithm the distance travelled by a wave in one time step should not exceed the length of one spatial step h as defined in equations 2.11 and 2.13. For applications where all shape functions are quadratic, CFL is taken as approximately 0.2 [Abboud et al, (1998)].This condition restricts any acoustic disturbances to propagate no more than 20% of the mesh size h during one time step Δt . But to calculate the optimum CFL for specific cases that are being simulated, iterations have to be performed when varying element size and time step. Using the nominal/theoretical value of speed of sound in the medium [Schmerr (1998)] the percentage difference has been calculated for theoretical speed and computed speed for wave propagation in the medium. The solution time is recorded against N and CFL to estimate computation expenses. These iterations can also help in developing a combination of different time step and element size which can give preliminary results within acceptable accuracy and more importantly in less solution time. This process is illustrated with the case of waves in an aluminum block with a 3mm diameter side drilled hole and t the following is data obtained from such iterations:

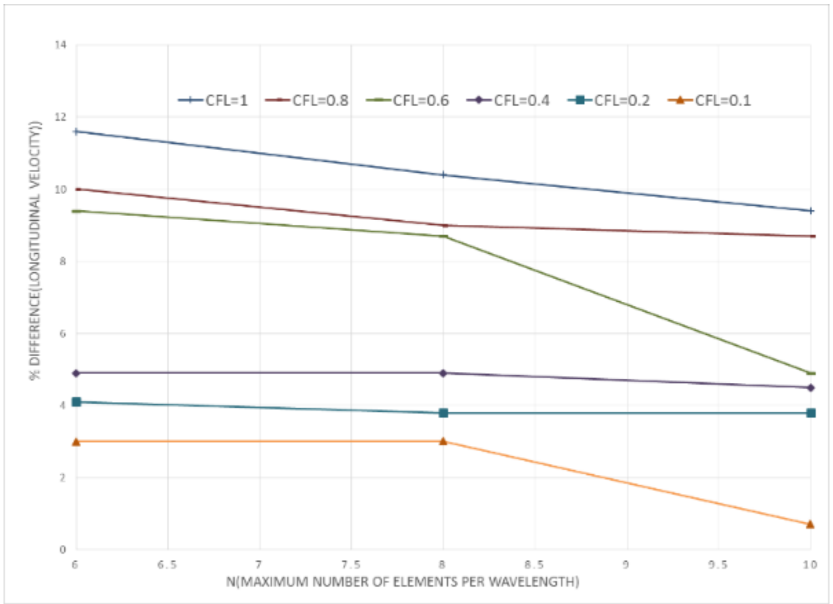

Figure 2.6 percentage difference in wave speed Vs N

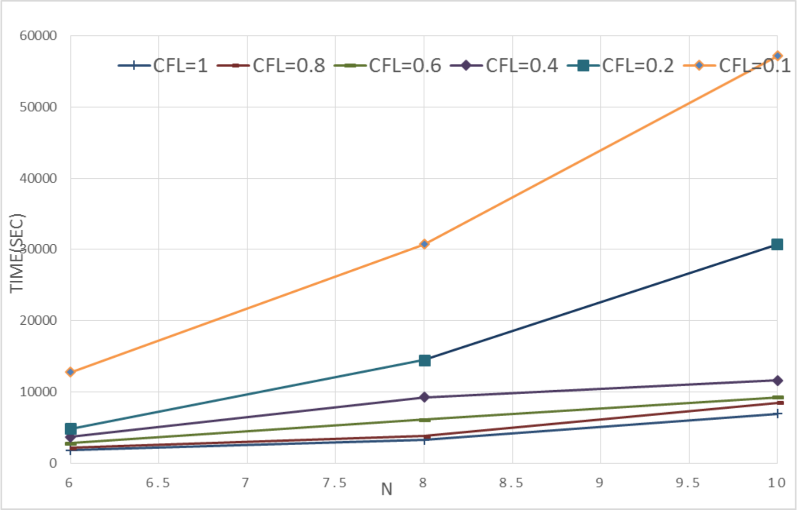

Figure 2.7 Solution time (sec) Vs N

From the results given in Figure 2.6, it can be seen that with increase in number of elements per wavelength and reduction in CFL, the percentage difference between theoretical wave speed and computed wave speed reduces. Less than a 5% difference was considered to be an acceptable result for the all the cases that were run. Hence using CFL<0.4 is observed to give acceptable results. However, from the data given in Figure 2.7 for CFL<0.4, the solution time seems to grow near-exponentially with increase in number of elements. Hence, a tradeoff is needed between number of elements and time step.

To determine this acceptable grid and time increments the difference between theoretical wave speed and computed wave speed with change in CFL was investigated. The resulting data are shown in Table 2.2 and Fig 2.8. From Figure 2.8(a), it is seen that at CFL=0.2, the percentage difference seems to converge irrespective of number of elements. Hence, by considering the data from Figure 2.6 through 2.8, N=8 and CFL=0.2 were selected as optimal and used for running the simulation for validation with the experimental data in all three cases discussed previously.

Table 2.2: Calculated and theoretical wave velocity (C), computing time and with N values

CFL	C theory*	C actual (m/s)			%Difference			Computation time(sec)		
	m/s	N= 6	8	10	N= 6	8	10	N= 6	8	10
1	6420	5673.8	5755.4	5818.2	11.6	10.4	9.4	1831	3263	6960
0.8	6420	5776.2	5839.4	5860.8	10	9	8.7	2211	3849	8507
0.6	6420	5818.2	5860.8	6106.7	9.4	8.7	4.9	2837	6120	9307
0.4	6420	6106.7	6106.7	6130.3	4.9	4.9	4.5	3720	9307	11657
0.2	6420	6153.8	6177.6	6177.6	4.1	3.8	3.8	4860	14520	30691
0.1	6420	6225.6	6225.6	6374.5	3	3	0.7	12774	30717	57109

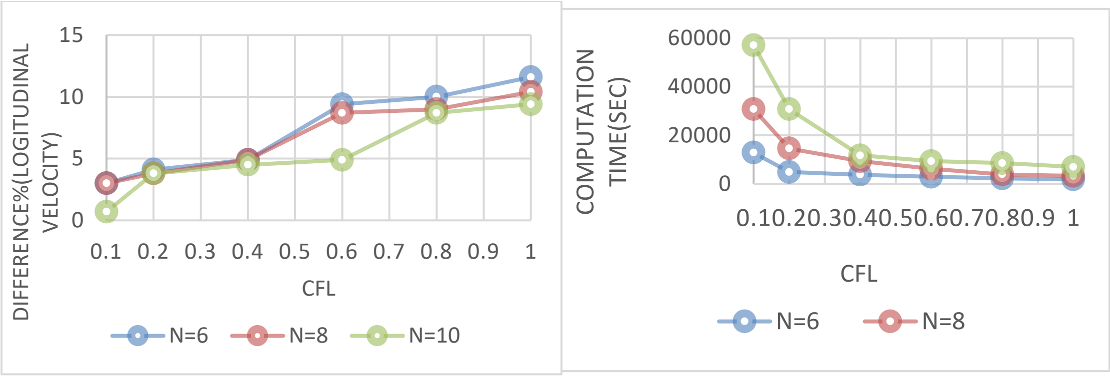

(a) (b)

Figure 2.8 Data investigating CLF parameter: a) percentage difference in wave speed Vs CFL and b) percentage difference in computation time Vs CFL

2.1.6 Validation Procedure

To validate the models and resulting computed data corresponding experimental data were obtained. Pulse-echo measurement were performed using a 2.25 MHz transducer with nominal diameter of 13mm for the active element, together with a Panametrics 5052 pulse-receiver and digital oscilloscope for data recording. The data is normalized for the ease of comparison with the model results. For the Case-1 with a transducer on an aluminum block, Sonotech gel is used as couplant. Case 2 consists of pulse-echo response from the nominal bottom of the fluid (water) and for Case 3 the response is from a 6.35 mm (1/4 inch) thick aluminum plate as shown in Fig 2.9:

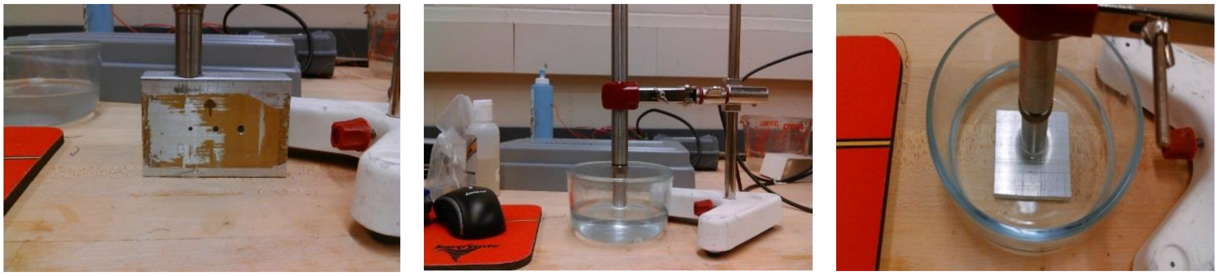

Figure 2.9 Experimental configurations for model validation:
a) Aluminum block *b) water and* *c) Aluminum + water*

2.1.7 Comparison of model and experimental data

The normalized pulse echo-data from experimental and computed measurements for all three cases can be compared as follows:

Case 1: Wave propagation in 50mm thick aluminum block with 3mm diameter side drilled hole.

The RF data measured above the SDH are shown in Fig 2.10. The arrival times are in acceptable agreement; however the amplitudes only show a qualitative agreement. A sequence of numerical visualizations of the elastic wave fields for the wave propagation in aluminum are given in Fig 2.11 and 2.12

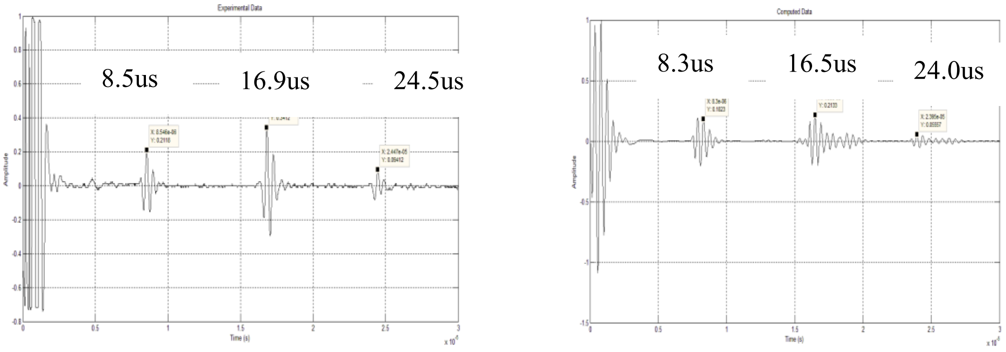

Figure 2.10 Response from a 3mm diameter side drilled hole:
a) Experimental Data and *b) Model results*

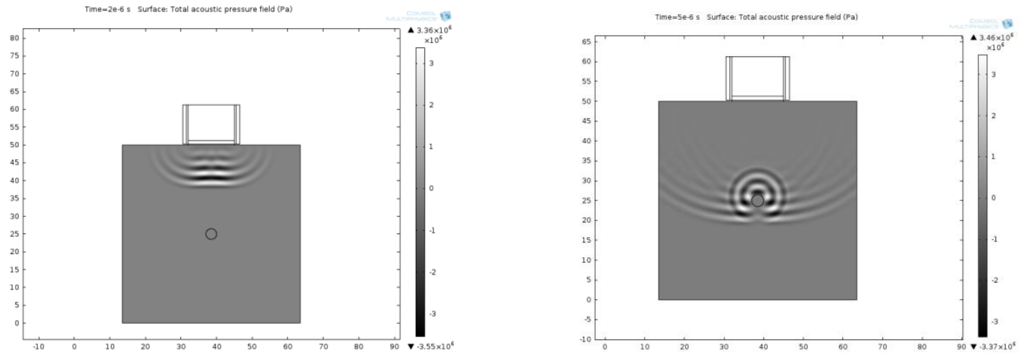

Figure 2.11 a) Incident wave-field from the transducer model *b) Mode conversion at side drilled hole*

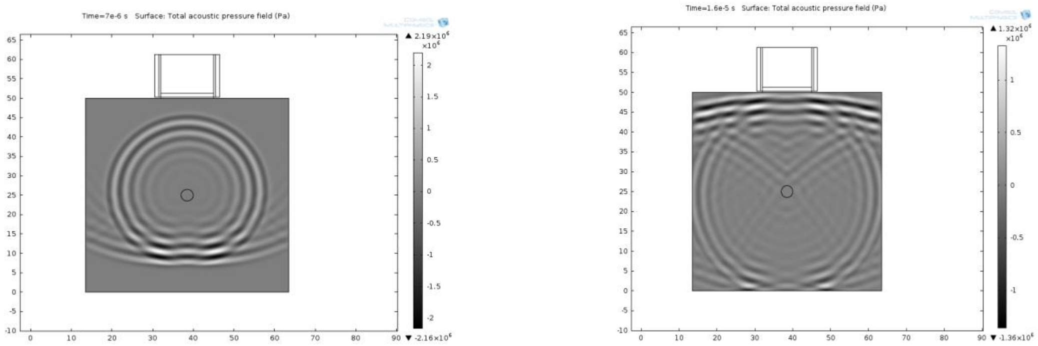

Figure 2.12 a) Mode converted wave-field from the side drilled hole *b) Backwall echo*

The wave fields shown in Fig 2.11 and 12 are in good agreement with those seen in photo-elastic visualizations for this geometry.

Case 2: Wave propagation in water

Pulse-echo data for the measurement configuration shown in Fig 2.9(b) with the transducer into water with the same nominal depth are shown as Fig 2.13. The basic pulse arrival times are in reasonable agreement.

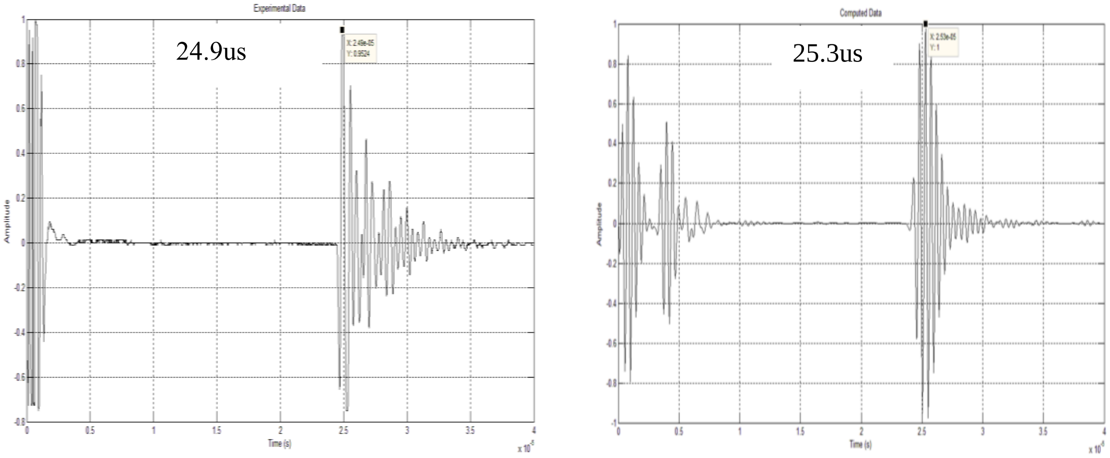

Figure 2.13 Pulse-echo measurements into water
a) Experimental data *b)Model data*

Case 3: Wave propagation in water and 6.35 mm (1/4 inch) thick aluminum block:

Pulse-echo data for the measurement configuration shown in Fig 2.9(c) with the transducer into water with the same nominal depth are shown as Fig 2.14. The primary echo for the aluminum front wall are in reasonable agreement.

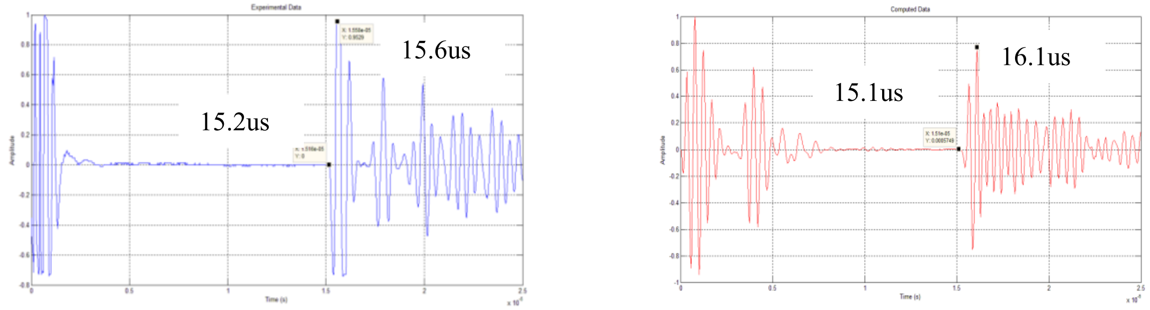

Figure 2.14 a) Experimental data b) Model data

The data was reviewed and the percentage difference for pulse-echo response between experimental and computed data was tabulated for all three cases shown in Table 2.3. The results from the computational model is in agreement with experimental data within 5% for arrival and wave peak times. Hence, the basic cases are considered validated at room temperature. Varying element size and time step for specific model can help to determine optimum element size in the mesh and time step. The present work uses mesh size of 8 elements per wavelength and time step at CFL =0.2. Absorbing can further be explored effective damping of outgoing waves at the sidewalls of computational geometry. By adding the external electric circuit to the transducer model, voltage source can be accurately modelled. Thus, the COMSOL model can now be developed to consider temperature dependency for performance parameters of transducers.

Table I Difference between first front wall-echo arrival time between experimental and computed data

Case	% maximum Difference
Case 1-Aluminum block	2.4
Case 2-water	1.6
Case 3-Aluminum and water	3.2

2.2 Preliminary Parametric study of temperature dependent material coefficients

The basic ultrasonic model using a COMSOL based finite element methods was extended to consider temperature dependence and this required gathering needed temperature dependent material properties. As shown in Figure 2.15, the goal was to include in the model the temperature dependency of the acoustic impedance of the wave propagating medium, d_{33} the piezoelectric charge coefficients of element material, the coefficient of thermal expansions for materials used in transducer assembly and the electrical conductivity of the liquid coolant.

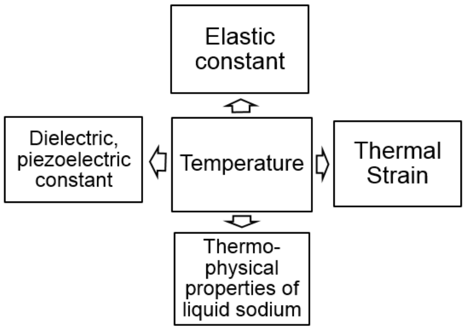

Figure 2.15 Parametric modeling

2.2.1 Attenuation due to thermos-physical properties of liquid sodium

Fast reactors (as well as accelerator-driven reactors) use liquid metal as the core coolant and as the heat transfer fluid from the reactor core to the steam generator. While a variety of liquid metal coolants (e.g., mercury, sodium, lead bismuth) have been used in different system worldwide, the current operating fast spectrum reactors in general use liquid sodium [Griffin et al. (2009)]. The current work includes modeling of the variation in thermophysical properties of liquid sodium, and the effects this has on ultrasound transduction. Previous studies have shown experimental data for the effects of variation in these properties with increasing temperature.

A summary of liquid sodium properties relevant to transducer development are reported by Foust (1972) and Liebowitz et al. (1971). The wave propagating medium for the current model is the liquid sodium-coolant and data are shown in Fig 2.16.

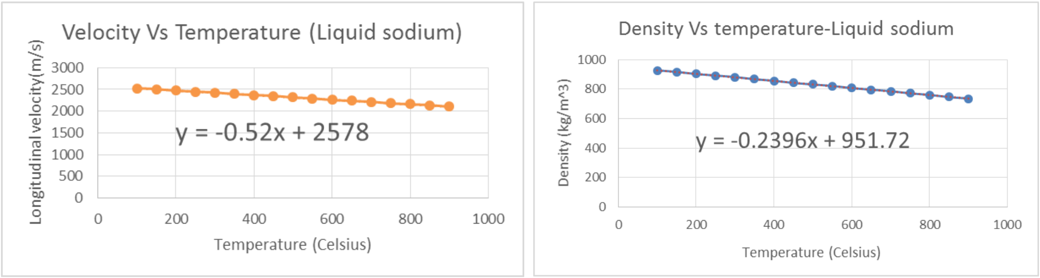

Figure 2.16 Temperature dependent liquid sodium properties
a) Longitudinal wave velocity *b) Density*

The equation which describes the change in longitudinal velocity for waves in liquid sodium with increase in temperature was published by Massacret et al. (2014) who referred to the equation published by Leibowitz, et al. (1971). Liebowitz calculated the speed of sound in liquid sodium up to 1000°C and the equation is given as:

$$C = 2577.6 - 0.536T \tag{2.14}$$

Where C is the velocity of sound in liquid sodium and T is temperature. This equation has been used to provide data for modeling of ultrasonic propagation in turbulent liquid sodium with a temperature gradient by Massacret, et al. (2014). The percentage difference in the speed of sound as measured by Foust and Liebowitz is less than 1%. Furthermore, when the values of speed of sound in liquid sodium at 250° C from Table 2.4 are compared with value given by Dierckx, et al. (2014) there is also less than 1% of difference. By linear fitting the data with coefficients as determination by equation 2.14, the density, thermal conductivity and dynamic viscosity variation in liquid with temperature can be obtained:

$$\rho = 951.72 - 0.2396T \tag{2.15}$$

$$J = 91.862 - 0.0496T \tag{2.16}$$

$$\eta = \ 0.0009 - \ 3*10^{-6}T \ - 2*10^{-12}T^3 + \ 4*10^{-9}T^2 \tag{2.17}$$

Where J is thermal conductivity, η is the dynamic viscosity and T is the temperature in Celsius. To further validate these equations a comparison was made between the latest published data. The speed of sound in liquid sodium at 250 C was calculated and values were compared with the data presented by Dierckx, et al. (2014). The difference between the values was less than 1%.

Pulse-echo finite element model developed is discussed in detail by Bilgunde and Bond (2015a). From the data given in Fig. 2.17, it can be seen that the amplitude of the first and second echo decreases as we increase the temperature of the liquid sodium from 100 to 250°C. The amplitude data are summarized in Table 2.5. This decrease in the amplitude is less than 1dB.

Table 2.4 Thermo-physical properties of liquid sodium

Temperature (°C)	Density (kg/m^3)	Dynamic viscosity (Pa-s)*10^{-4}	Speed of sound m/s	Thermal conductivity (J/kg-K)	Speed of sound m/s
100	9269	6.802	2526	86.9	2524
150	9153	5.415	2500	84.4	2497
200	9036	4.519	2474	82	2470
250	8918	3.900	2448	79.6	2443

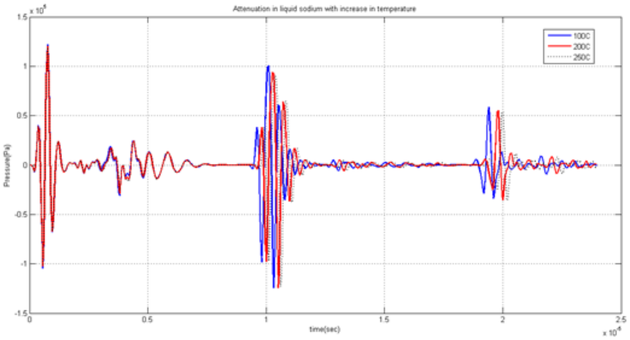

Figure 2.17 change in pulse-echo response with increase in temperature of liquid sodium

Table 2.5 Pulse-echo peak amplitude with varying temperature of liquid sodium

Temperature (Celsius)	1st Front wall Echo (Pa)	2nd Front wall Echo (Pa)
100	9.9e4	5.9e4
200	9.3e4	5.5e4
250	8.8e4	5.4e4

2.2.2 De-bonding due to thermal expansion

Thermal expansion is one potential parameter which can pose a complex problem in the design of high temperature transducers. The backing layer, the piezoelectric element and the matching layer have diverse aspect ratio and thermal expansion coefficients and they can undergo different rates of thermal expansion. The various expansion coefficients can cause thermal strains at interfaces and in the piezoelectric material. This strain and temperature can affect the response of the piezoelectric material and hence the performance of the ultrasonic transducer. Moreover, with high thermal strain the backing material can have a loss of electrical and/or mechanical contact with the piezoelectric element causing loss of damping, adversely affecting S:N ratio and hence, the defect detection capability. The study used the finite element method to model the effect of changes in properties with temperature, thermal shock and hence the thermal strain on the piezoelectric response.

Medina et al. (2006) have reported the material properties shown in Table 2.6 which are those used in the FE model in this work. The study uses the linear thermal expansion coefficient reported by Piezo-technologies (K350) (PiezoTechnologies Indianapolis, IN,) and Duralco 4703[Cotronics New York). The liquid sodium coolant and PZT-5A temperature dependent properties used are those reported in previous studies [Sabat et al. (2007), Leibowitz et al (1971), Dierckx et al. (2014)].

Table 2.6 Material model (Medina et al. 2008)

Material	Density (Kg/m3)	Poison Ratio	Elasticity module(N/m2)	β damping
Araldite	1096	0.34	0.55e10	2.3e-8
Araldite/Tungst	5766	0.34	1.05e10	1.5e-8
Nylon	1405	0.27	0.74e10	5e-9
Steel	7890	0.29	26.51e10	10e-8

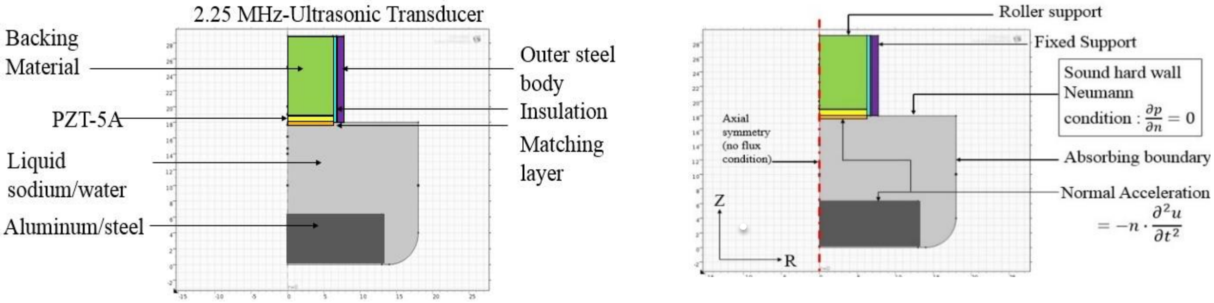

Figure 2.18 a) Geometric configuration of the model *b) Boundary conditions*

The thermal expansion simulation is carried out in ABAQUS™. A solid coupling bonding technique [Kazys et al. (2008)] has been simulated for epoxy bonding between the materials. The bonding agent is modelled as a contact property between the transducer components. The computed deformation due to de-bonding is converted into an equivalent acoustic model by modeling an air gap for the corresponding deformation (20 microns). Hence, the de-bonding process here is basically treated as a special case of a lightly damped ultrasonic transducer in the model. The configuration is shown in Fig 2.19.

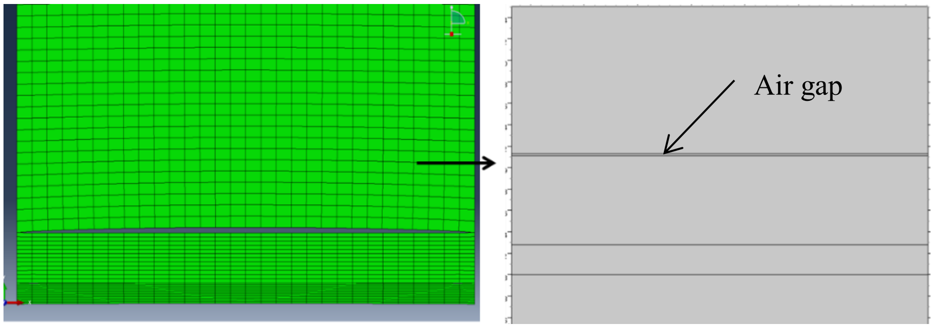

Figure 2.19 a) Deformation of the backing material due to thermal expansion b) Transforming this deformation into an ultrasonic model

The changes in time domain waveform due to temperature effects and due to temperature accompanied by the de-boding effect are compared in Figure 2.20. It can be clearly seen that de-bonding serves as a source of acoustic noise due to "ringing" of the signal. The de-bonding basically makes the transducers lightly damped which causes a reduction in the bandwidth. It was found that further investigation is needed to quantify effect of de-bonding on the signal to noise ratio.

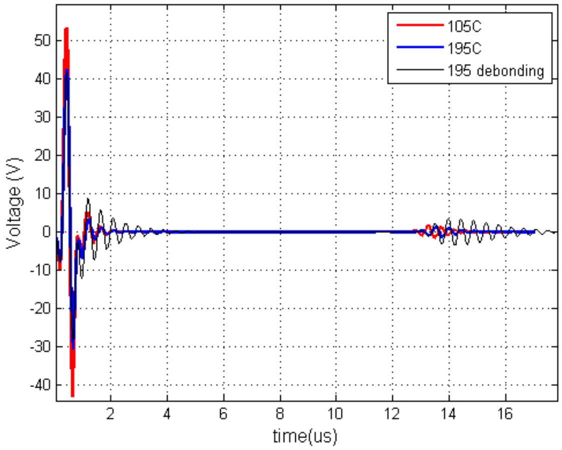

Figure 2.20 Multiple reflection resulting into ringing of the ultrasonic signal due to de-bonding

2.3 Temperature dependent material coefficients of piezoelectric material

An ultrasonic NDE measurement uses what is basically a linear time-shift invariant system comprising of response functions. One such response function is for the conversion of an electric pulse into a mechanical motion which generates a wave. This is called the direct piezoelectric effect which is described earlier by equation 2.1. Due to symmetry of poled piezoelectric ceramics the parameters that form the complete material matrix reduce to the ten independent coefficients for PZT which includes five elastic, three piezoelectric and two dielectric constants. (Sabat et al (2007), Jordan and Ounaies (2001). Temperature variation of these constants impacts the piezoelectric effect and thus it can affect the strength of the transmitted and received ultrasonic signals.

To study the effect of each constant, specifically the dielectric constants and electrical properties of PZT-5A, they were used in the temperature dependent FEA model using values of parameters reported in published data. The resulting sensitivity of the transducer needs to be sufficiently high to differentiate intentionally generated signals from the background noise. This sensitivity is dependent on the piezoelectric charge coefficient (d) and piezoelectric voltage coefficient (g).

For elastic solids, an applied mechanical stress, T, produces mechanical strain, S. However, the piezoelectric effect produces an electric charge Q and with mechanical strain S which is also called as the direct effect. The dielectric displacement due to this effect can be expressed as:

$$D = Q / \mathrm{A} = \mathrm{d}^* \mathrm{T} \tag{2.18}$$

where d is the piezoelectric charge coefficient, A is the area of the material and *D* is the dielectric displacement.

Using the equations(2.1) and (2.2), it can be shown that:

$$d_{33} = k_{33}\sqrt{\varepsilon_0 K_3 S_{33}^E}, \qquad S_{33}^E = \frac{S_{33}^D}{1-k_{33}^{\ 2}} = \frac{1}{4\rho f_n^2 l^2}, \qquad k_{33} = \sqrt{\frac{\pi}{2}\frac{f_m}{f_n}\tan\left[\frac{\pi}{2}\frac{f_n - f_m}{f_n}\right]} \tag{2.19}$$

$$d_{33} = \sqrt{\left(\frac{k_{33}^{\ 2}}{1-k_{33}^{\ 2}}\right)\varepsilon_0\left(K_3\frac{1}{4\rho f_n^2 l^2}\right)} \tag{2.20}$$

where k_{33} is the extensional coupling factor, f_n is the frequency at the maximum impedance, f_m is the frequency at the minimum impedance, S_{33}^E is the elastic compliance constant at constant electric field E, S_{33}^D is the elastic complinace constant at constant electric displacement *D*, K_3 is the dielectric constant, ρ is the density of the piezoelectric material and l is the radius of the circular piezoelectric element. From equation (2.20) it can be seen that the effective d_{33} is a function is of dielectric constant K_3, density of piezoelectric material and radius of the piezoelectric element which can be expressed as:

$$d_{33}\alpha\sqrt{K_3} \quad , \quad d_{33}\alpha\frac{1}{l} \quad , \quad d_{33}\alpha\frac{1}{\sqrt{\rho}} \tag{2.21}$$

where the dielectric constant K_3 is the ratio of permittivity of the piezoelectric material to the permittivity of the free space. Hence, K_3 becomes a material property together with density ρ for the piezoelectric material. d_{33} is inversely proportional to radius l of the circular piezoelectric element

A high value for the piezoelectric voltage coefficient g_{33} is desirable in materials which are intended to generate voltages in response to the applied mechanical stress. The piezoelectric voltage coefficient can be described as

$$g_{33} = \frac{d_{33}}{\varepsilon_0 K_3} \tag{2.22}$$

$$g_{33}\alpha\frac{1}{\sqrt{K_3}} \tag{2.23}$$

Using equations 2.21 to 2.23 it can be shown that the voltage coefficient is inversely proportional to the dielectric constant K_3 which is a material property. The voltage corresponds to the pressure generated when a pressure wave is transmitted into the acoustic medium and received back. In the past many authors have measured the change in electrical properties of PZT-5A with increase in temperature [Gubinyi et al (2008)].

The simulated effects of varying dielectric constant and electrical properties of PZT-5A each at a time is shown in section 2.3.1 and 2.3.2. From the results, it was observed that increase in dielectric constant was a major contributor to the reduction in the amplitude of trasmitted and received pulses. It was also observed that from the resuts in the section 2.3.2 that in the temperature range from 150 to 250 C the voltage across the piezoelectric material reduces significantly, indicating a non linearity in the material properties.

The study of these results helped to understand the effect of varying dielectric contstant K and d_{33} and d_{31} properties of the piezoelectric material. However, it can be clearly seen from equation (2.1) that the elastic constants also play an important role in the the piezoelectric effect and hence the genrated ultrasonic signal. This can illustrated in matrix form as:

$$\begin{bmatrix} S1 \\ S2 \\ S3 \\ S4 \\ S5 \\ S6 \\ D1 \\ D2 \\ D3 \end{bmatrix} = \begin{bmatrix} s_{11}^E & s_{12}^E & s_{13}^E & 0 & 0 & 0 & 0 & 0 & d_{31} \\ s_{12}^E & s_{11}^E & s_{13}^E & 0 & 0 & 0 & 0 & 0 & d_{31} \\ s_{13}^E & s_{13}^E & s_{33}^E & 0 & 0 & 0 & 0 & 0 & d_{33} \\ 0 & 0 & 0 & s_{55}^E & 0 & 0 & 0 & d_{15} & 0 \\ 0 & 0 & 0 & 0 & s_{55}^E & 0 & d_{15} & 0 & 0 \\ 0 & 0 & 0 & 0 & 0 & 2(s_{11}^E - s_{12}^E) & 0 & 0 & 0 \\ 0 & 0 & 0 & 0 & d_{15} & 0 & \varepsilon_{11}^T & 0 & 0 \\ 0 & 0 & 0 & d_{15} & 0 & 0 & 0 & \varepsilon_{11}^T & 0 \\ d_{31} & d_{31} & d_{33} & 0 & 0 & 0 & 0 & 0 & \varepsilon_{33}^T \end{bmatrix} \begin{bmatrix} T_1 \\ T_2 \\ T_3 \\ T_4 \\ T_5 \\ T_6 \\ E_1 \\ E_2 \\ E_3 \end{bmatrix} \tag{2.24}$$

It is thus necessary to understand the temperature dependency of the complete material matrix shown in equation (2.24) to be able to analyse the effect of temperature on the ultrasonic signal. Sabat et. al (2007) reported the variation in elastic, piezoelectric and dielectric properties for PZT-5A. Using this data and equation (2.24), the finite element simulation has helped to understand the significance and interaction between the elastic, piezoelectric and the dielectric constants.

The results obtained from the FE simulation are given in section 2.4. It should be noted that these results indicated that when all the independent material constant are varied as a function of temperature, the loss in amplitude of signal when transitioning from 105C to 195C is expected to be not more than 2dB.

A series of simulations were run to investigate the effects of variation in various material properties, constants and geometry on transducer performance.

2.3.1 Variation in dielectric constant and disc radius of piezoelectric material.

A series of simulations were run to investigate the effects of variation in dielectric constants and disc radius for the piezoelectric material on transducer performance. The observed trends are shown in Figures 2.21-2.23

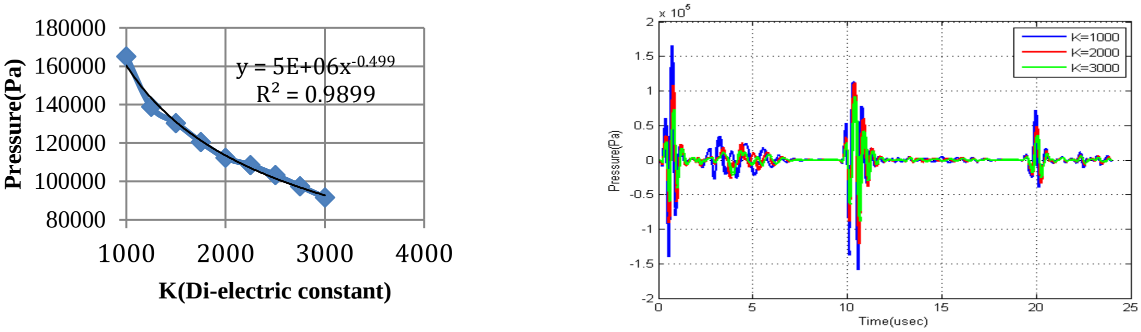

Figure 2.21 Variation in pressure amplitude as function of dielectric constant

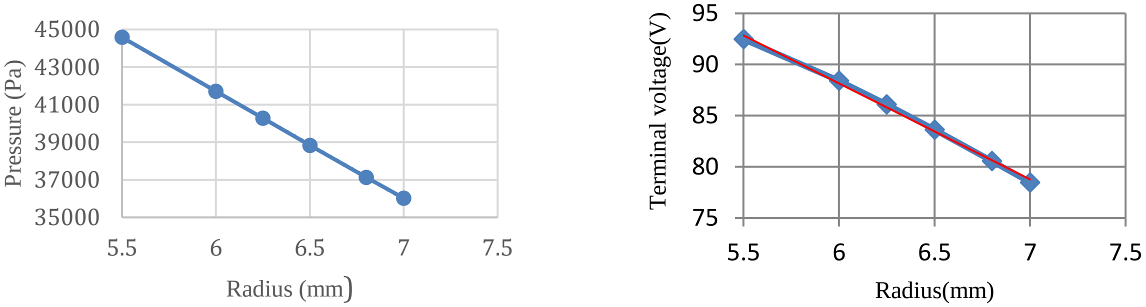

Figure 2.22 Variation in pressure amplitude and maximum terminal voltage as function of disc radius

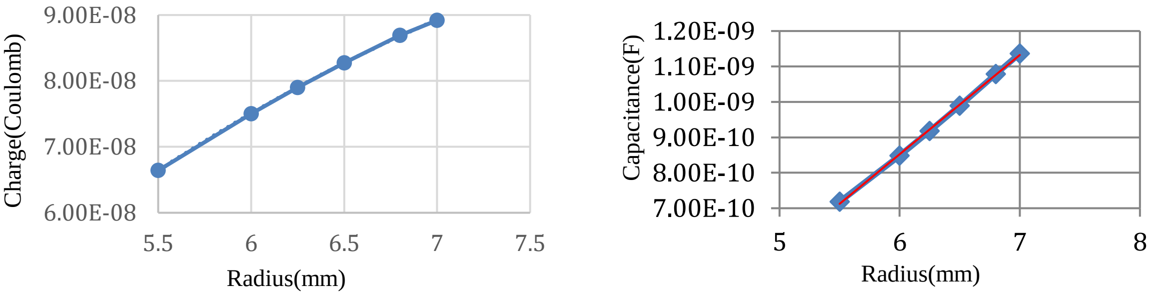

Figure 2.23 Variation in electric charge and capacitance as function of disc radius

As the dielectric constant increases with temperature [Sabat et al. (2007)], the amplitude of the pressure wave transmitted goes down as seen in Figs. 2.21(a-b) which is in agreement with trend predicted using equation 2.23 which states that the pressure and hence the voltage is inversely proportional to the square root of dielectric constant. From the model data reported in Figure 2.22 and 2.23, it is seen that reduction in radius of the circular piezoelectric element from a nominal 6.5mm to 5.5 mm can improve the sensitivity and as the amplitude of voltage increases, the electric charge and consequently the capacitance decreases. This observation confirms the idea that the optimization of the radius of the circular piezoelectric element is one parameter to consider to improve sensitivity and potentially S:N.

2.3.2 Variation in dielectric constants d_{33} and d_{31}

The electrical properties of PZT 5A from -150 to 250° C were measured by Hooker (1998). This data (K, d_{33} and d_{31}) was used in the computational model to determine how these parameters affect the amplitude of the signal, charge and hence the capacitance of the piezoelectric element as the temperature is increased.

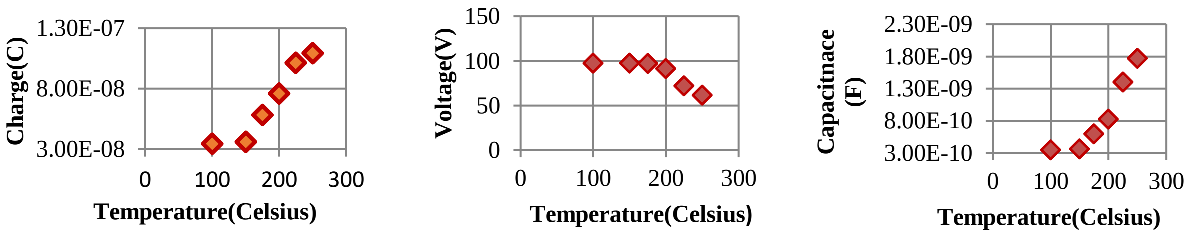

Figure 2.24 Variation in electric charge, voltage and capacitance respectively as a function of temperature

From the data reported in Fig. 2.10 it shows that the voltage at the piezoelectric material decreases as the temperature is increased between 150 and 250°C. Fig. 2.10 shows that as the temperature increases, the capacitance of the piezoelectric material also increases. The increase in capacitance shows that the ability to store charge increases which is also evident from the data in Fig. 2.10. This increase in the capacitance is attributed to an increase in dielectric constant with temperature as given by the equation:

$$C = \frac{\varepsilon_0 KA}{t} \qquad (2.24)$$

2.3.3 Effect of all ten temperature dependent material constants

A series of simulations were run which included the use of all ten independent material constants and also the effects of de-bonding due to thermal expansion. The resulting data are shown in Fig 2.25 (a-b).

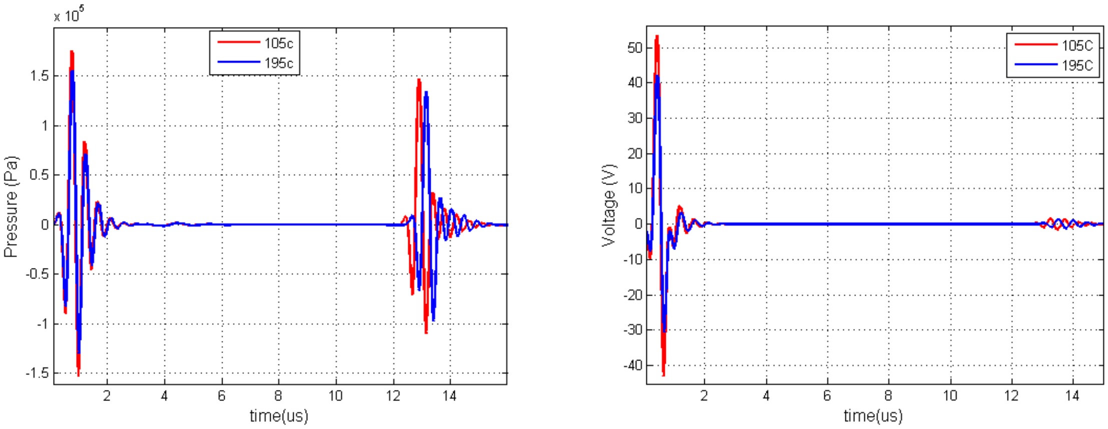

Figure 2.25 Pulse echo response

a) Pressure amplitude at 105 and 195C

b) Voltage across the piezo electric material at 105and 195C

From the data in Fig 2.25 it is seen that as the temperature of simulated liquid sodium coolant is increased from 105°C to 195°C, the pressure amplitude decreases by 1dB and voltage measured across PZT-5A decreases by 2dB. This loss in the amplitude does not seem to be significant. As stated earlier, there are ten temperature dependent coefficients for PZT-5A which includes five elastic, three piezoelectric and two dielectric constants. The changes in amplitude of the simulated signal if only two piezoelectric and two dielectric constant are varied as a function of temperature was discussed in a project conference paper (Bilgunde and Bond, 2016). From the current studies it appears that the temperature dependent variation in elastic constants also play important role in determining losses in the amplitude of the signal

2.3.4 Testing facilities and experimental results

In developing a room temperature facility that can operate with a room temperature liquid metal various safety procedure needed to be followed. Based on the material safety data sheet and discussion with the Industrial Hygiene Manager from the DOE Ames Laboratory (who provided that material), inhalation of both Gallium and Indium may cause renal damage. An animal report documented the fatality associated with gallium chloride inhalation though it was rare. Oxidation of the alloy may be an issue if an inert atmosphere is allowed.

To address safety concerns a system was developed that involved working with an open vessel in a glove box solves that problem. The fume hood used is shown in Figure 2.26. The adjacent area was cleaned, and a scanning systems developed, so that it can be moved inside the hood when liquid metal work was initiated.

Figure 2.26 Fume hood under which the motion stage to be installed

A series of 3-D CAD models were developed to guide the design of the scanning system and to ensure that access and clearances could be met and the design is shown in Fig 2.27. The outer box is the space available in the hood. Using the maximum dimension of the motion stages given by the supplier (including the maximum travel), solid block models were created which represented X-Y-Z stages. A 1 liter Pyrex vessel is used as a nominal surrogate coolant container.

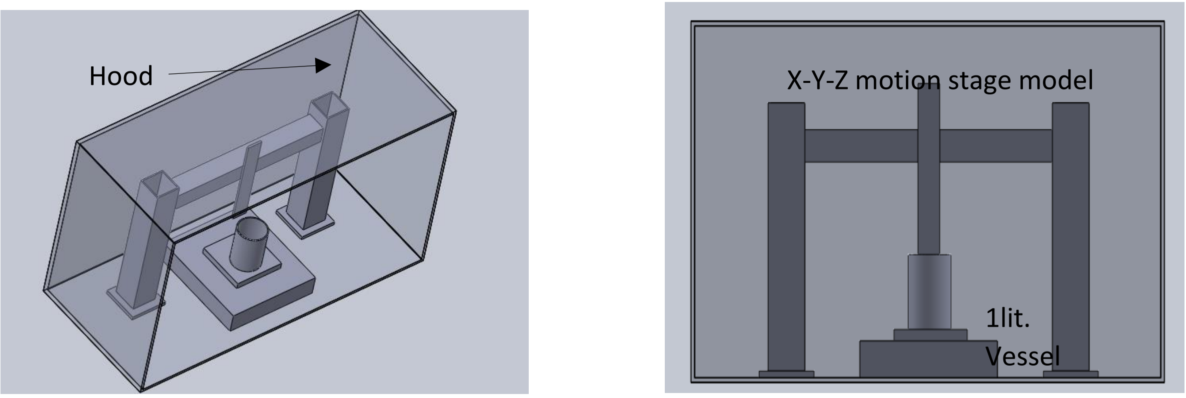

Figure 2.27 Conceptual scanning frame design in fume hood.

The x-y-z motion stage, as delivered is shown in Fig 2.28, together with a pulse-receiver and oscilloscope used in initial testing. The X stage has 100 mm travel while Y and Z stage has 200mm travel. The encoder has 1 micron resolution while the resolution that was actually required for defect is 40 microns. The motor is a brushless servo motor to minimize the electrical noise coming from the Parker systems. The Z axis in Fig 2.28 shows a flat mountings plate. A set of sensor mounts were fabricated to accommodate the PNNL transducer, various commercial and other ultrasonic and eddy current sensors.

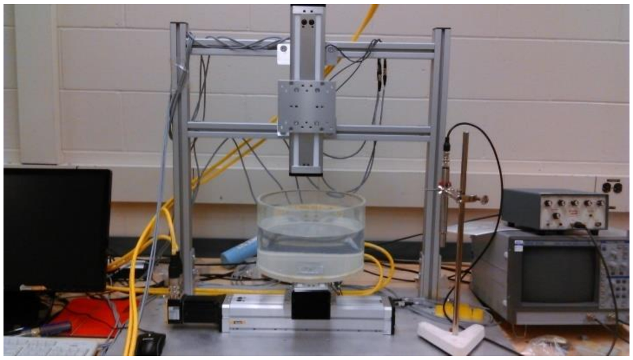

Figure 2.28 Parker-Hannifin x-y-z motion stage

2.3.5 Preliminary Experimental results

One of the original PNNL single element ultrasonic transducers used in immersion testing in sodium was provided to ISU. Basic pulse-echo measurements were performed at room temperature in water with the PNNL high temperature transducer and a commercial (Panametrics V306) transducer. Measurements with both the transducers were performed using the same set-up. Examples of measured signals are shown in Fig 2.29(a-b). As it can be seen, the PNNL high temperature transducer exhibits a long (40 micro-sec) reverberation decay, following initial excitation, which is an indicator of acoustic "ringing" occurring inside the transducer. This phenomena also results in a significant fraction of the acoustic energy emitted being in the form of reverberations, rather than going into the pulse to be used in testing. In addition there was only limited S:N for the initial reflection. These observations highlighted the major goals for the

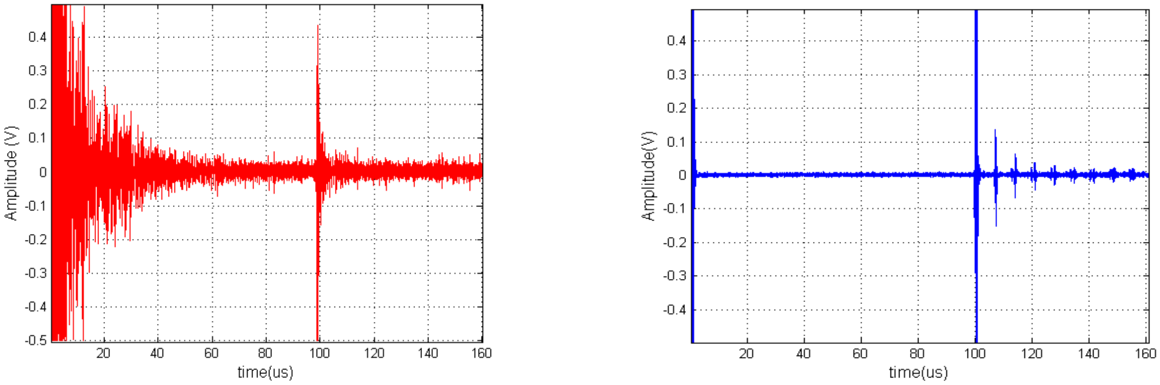

Figure 2.29 Pulse-echo response

a)PNNL high temperature transducer *b) Panametrics V306-SU (commercial) immersion transducer*

project which were to seek to provide a high temperature transducer with performance properties closer to those seen in the signal given as Fig 2.29(b), rather than Fig 2.29(a).

Work continued to better noise the reverberations in the PNNL transducer and to seek to develop design modification that could improve performance. It therefore appears that that the ringing most probably can be attributed to a combination of the internal transducer components (piezoelectric disc, matching layer and backing), in combination with solder layers, and all amplified by potentially de-bonding of backing element or the soldered joint between piezo element and faceplate at temperature

Frequency response analysis of the transient signal is necessary for further analysis of the transducer which will be discussed in the next chapter.

3. Study of acoustic cross-talk in piezoelectric based Ultrasonic transducers

In section 2, RF data for the PNNL transducer and the commercial Panametrics transducer was acquired, with the later showing significantly better signal to noise ratio than the PNNL research transducer. Unfortunately, the design concept used in the commercial immersion transducer cannot be simply adapted and used at high temperature: the materials don't have the required properties. A design with a complete metal case, including a metal front face matching later/wear plate is needed for immersion in liquid sodium.

A basic part of the current study was to look at the causes of noise in transducer signals, together with factors that limit the signal strength of the signal output. Two components considered were the electrical noise and acoustic reverberations/cross-talk and its potential contribution to the limited signal to noise ratio that is achievable.

The time domain data acquired with PNNL and commercial transducer (Panametrics Type V306) in a pulse-echo experiment in water giving a reflected signal from a 25.4mm thick circular disc are shown in Figure 3.1 (a-b). The experiments were performed in sequence and the data was recorded using a digital oscilloscope. The damping, energy and gain settings of the Panametrics pulsar-receiver (Type 5052) were kept same for both the experiments which were performed using the same BNC cable to eliminate differences due to system characteristics (pulsar, cable, and oscilloscope) from signals shown in Figure 3.1.

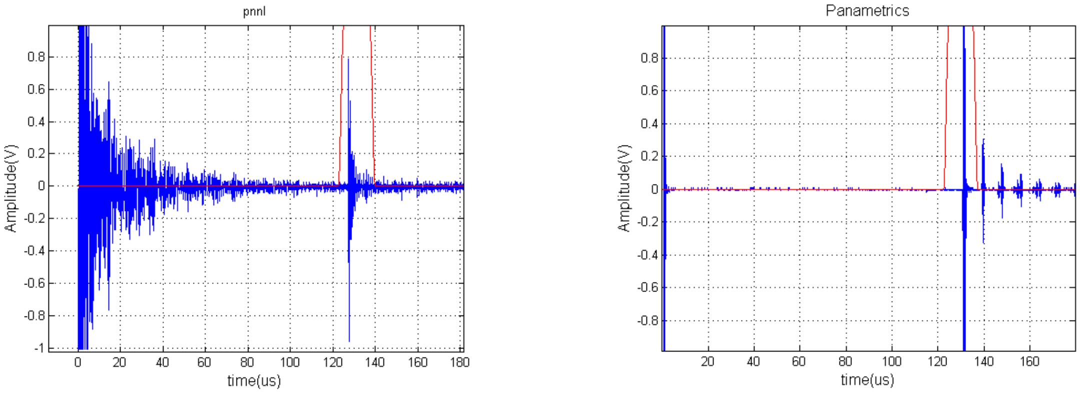

Figure 3.1 Time domain data for
a) PNNL research Transducer *b) Commercial Panametrics transducer V 306*

The gates (shown in red on Fig 3.1) were set to extract data for further analysis. An FFT was applied to the front wall echo. The resulting spectra for the PNNL and commercial transducer are shown in Figure 3.2. In reviewing data it is seen that the peak for the commercial transducer the peak is at the 2.1 MHz, which close to the manufacturers specified frequency of 2.25MHz. The nominal design operating frequency of the high temperature transducer is also 2.25MHz. However, the spectrum of the PNNL high temperature transducer is more complex and exhibits several peaks at 1.3, 2.97, 4 and 7.8 MHz as shown in figure 3.2(a). It is believed that these peaks are due to the effect of backing and matching layer on the resonance of piezoelectric material and this was investigated further.

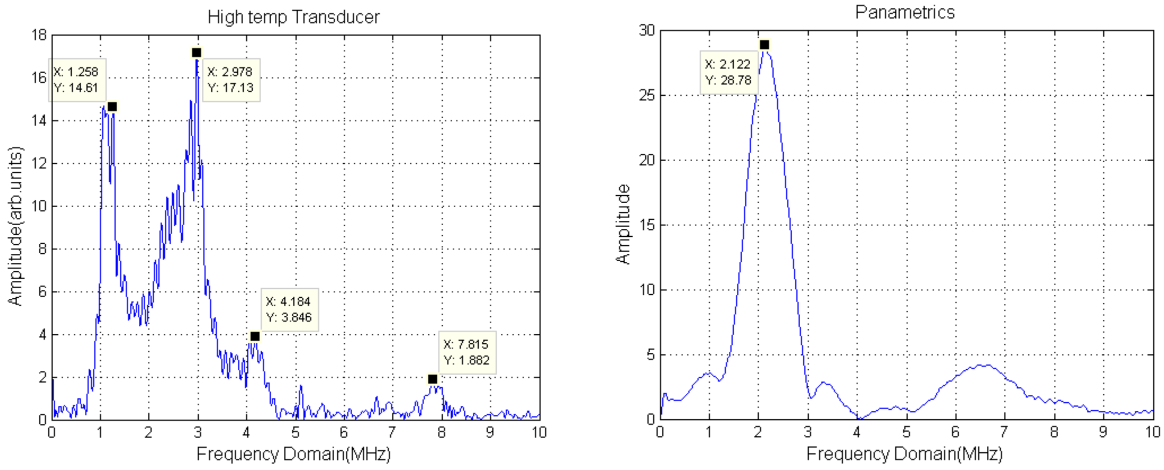

Figure 3.2 Frequency response of

(a PNNL high temperature transducer *(b Commercial (Panametrics V306) transducer*

By definition, center frequency of band-pass filter is the geometric mean of the lower and upper cut off frequencies. For the high temperature transducer (PNNL) there are two peaks at 1.258 and 2.978 MHz peaks as shown in figure 3.2(a), which have a mean value of 1.9MHz which is closer to the nominal center frequency than either peak. In analysis the center frequency is related to quality factor of the transducer given by Kinsler and Frey (1962):

$$Q = \omega_o / Bw \qquad (3.1)$$

where Q is the quality factor, ω_o is the resonant frequency and B_w is the 6dB bandwidth of the transducer. Mathematical treatment is required for further investigation of the observed bimodal phenomenon.

3.1 Analysis of bimodal response

A tone-burst of 5 cycles of sine wave is set as the input function, shown in Figure 3.3(a)

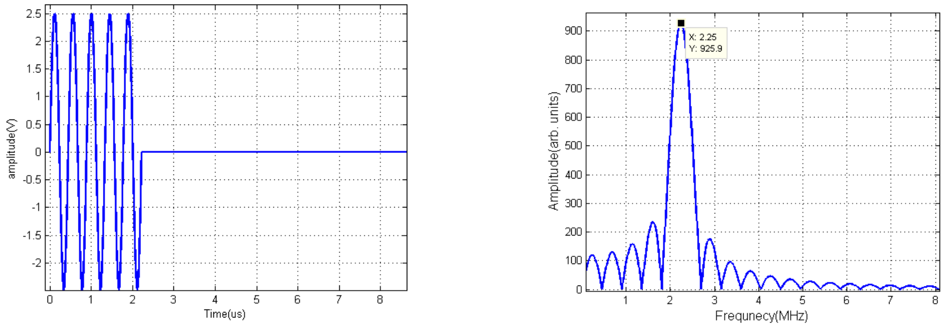

Figure 3.3 Five cycle tone burst a) Time domain signal and b) Frequency domain

The spectrum given by application of Fast Fourier Transform (FFT) to the tone burst of 5 cycles sine wave is shown in figure 3.3(b) which shows the peak amplitude at the nominal center frequency 2.25MHz.

The source function is modified using the relationship:

$$y=a.\sin(\omega\ t)*(a.\sin(\omega\ /2)*t) \qquad (3.2)$$

where a is the initial amplitude, ω is angular frequency, t is time. Equation (3.2) represents the convolution of the original source function with a source function corresponding to a signal with half the angular frequency. The original angular frequency ω = 2*π*2.25e6 rad/s is the actual angular frequency of the high temperature transducer.

Convolution of two sine function $a\sin(\omega t)$ and $a\sin(\omega\ /2)t$ in time domain results into superposition of sine waves as shown in Fig 3.4. The corresponding spectrum is shown in Figure 3.5, where there are peak amplitudes at 1.17 and 3.36 MHz. The geometric mean of these peak amplitudes corresponds to 1.98MHz.

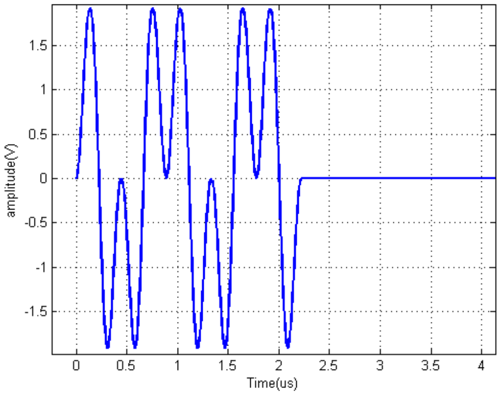

Figure 3.4 Time domain signal for convolved fundamental and sub-harmonic.

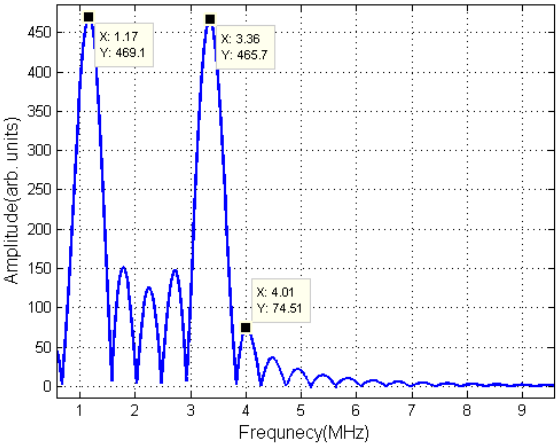

Figure 3.5 Spectrum for signal shown in Fig 3.4.

When Figures 3.2 and 3.5 are compared it can be observed that both the spectra demonstrate a bimodal response. Also, the frequency at which peak amplitude is observed is similar in both figures. The convolution shown in equation (2) physically represents particle motion at an angular frequency half of the center frequency of the transducer in addition to the center frequency of the transducer. Convolution of this two response functions results in the peak amplitudes of 1.17 and 3.36 MHz and not the 2.25 MHz which is the nominal design center frequency of the transducer.

Removal of the bimodal response in the spectrum could potentially significantly improve the signal to noise ratio for the high temperature transducer.

The potential physical causes for the bimodal response were investigated. One of the possibilities for causes for such a response reported in previous literature is the de-bonding at high temperature. Kazys et al. (2008) reported that 60% of high temperature transducer have an adhesion problems. It was therefore decided to investigate this phenomena further using the finite element method [COMSOL™ (2015)]. The model treated de-bonding as a reduction in the damping or increase in the Q factor of the transducer as explained in section 2.2.2 and described with equation 3.1.

Results from an experiment and the and FE model [Bilgunde and Bond (2015a)] are shown in Fig 3.6 and both sets of data show decaying nature of incidence pulse. An FFT was used to give the spectrum of the model data and the result is shown in figure 3.7:

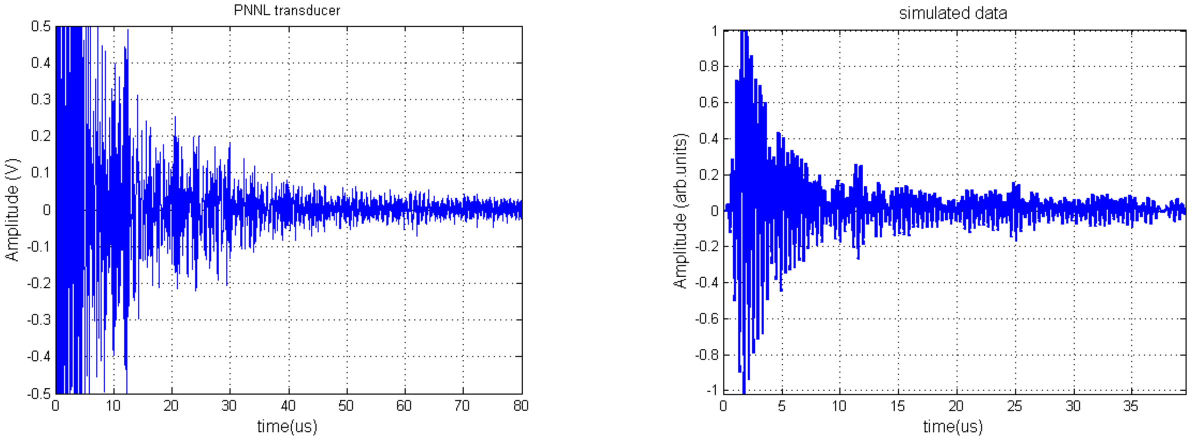

Figure 3.6 a) Experimental data *b) Model data*

The data given in Figure 3.7 indicate that the reduction in the damping which occurs causes a reduction in bandwidth of the transducer. It does not however show peak amplitudes at frequency other than the center frequency of the transducer. To investigate this observation further additional signal processing was performed.

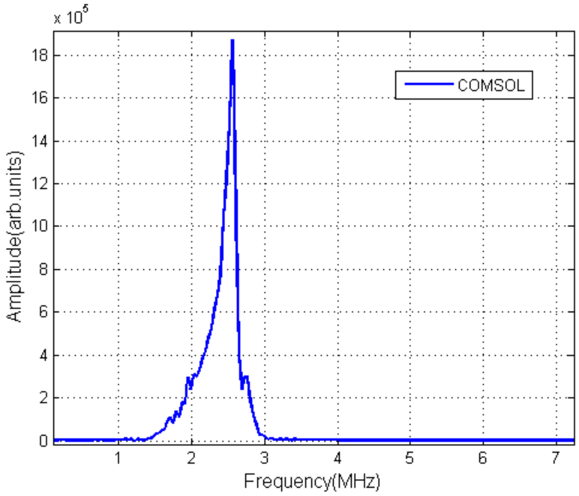

Figure 3.7 Fast Fourier transform of the simulated data

The reduction in the damping of transducer causes an exponential decay in the envelope of the resulting signal from the transducer as shown in figure 3.6(b). This exponential decay can be described by $e^{-\alpha t}$ where α is the attenuation coefficient:

$$\alpha = \omega_0/2Q \tag{3.3}$$

where ω_0 is the resonant angular frequency and Q is the quality factor of the transducer.

If this response in the form of an exponential decay is convoluted with the source function described by equation 3.2 the function then becomes:

$$y=a.sin(\omega t)*(a.sin((\omega/2)*t))*exp(-\omega_0 t/2Q) \tag{3.4}$$

The time domain signal given using equation 3.4 is shown in Fig 3.8 and the exponential decay can be clearly seen in addition to the superposition of waves.

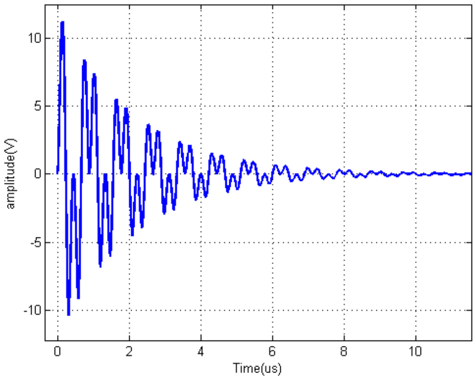

Figure 3.8 Time domain signal for the source function

The spectrum of the data obtained when equation 3.4, and shown in Fig 3.8, is shown as Fig 3.9. When these data and that obtained with equation 3.2 and shown in figure 3.5 are compared it can be seen that the bandwidth of the curves corresponding to the peaks reduces in figure 3.9 as compared to figure 3.5. Also, the frequency lobes between the peaks of bimodality in figure 3.5 reduce in magnitude in figure 3.9. It is also seen that the spectrum derived from data calculated using equation 3.4 shows similar characteristics to the experimental data shown in figure 3.2(a)

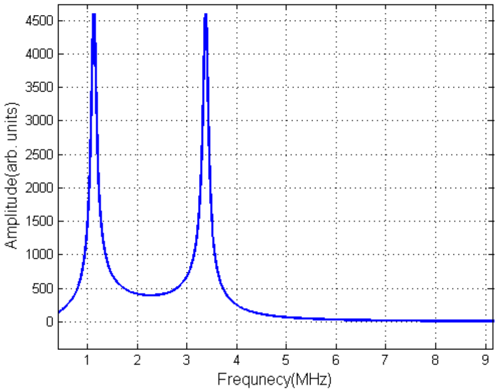

Figure 3.9 Frequency spectrum of source function from equation 3.3

To summarize, a pure sine wave tone burst will produce spectrum as shown in Figure 3.3b. Thus, equation 3.2 and 3.3 demonstrate that spectrum of transmitted pulse from the transducer will change if the source function is modified. Figure 3.5 shows the effect on resonance spectrum when the original source function is convoluted by response function at frequency half the center frequency of the transducer. Lastly, figure 3.9 shows the spectrum when equation 3.2 is convoluted by exponential decay response function which physically represents the increase in the Q factor or reduction in the damping of the transducer. Such analysis can help designing a novel high temperature transducer for determining the required Q value for the transducer. Solid mechanics approach towards describing this bimodal phenomenon is discussed in the next section to study the effect of acoustic impedance and thickness of the sensor elements on the resonance spectrum.

3.2 Transmission phenomena through three media; Normal Incidence

In an ultrasonic transducer, electrodes are typically made from gold, silver or nickel are deposited on the piezoelectric disc. The change in the transmission coefficient due to these layers is often not considered due to their small thickness. The thickness of the piezoelectric element is half-wavelength based on the centre frequency of the transducer. In NDT, typically broad bandwidth is required for which minimizing ring-down of the initial incidence pulse is a critical issue; specifically for the acoustic impedance mismatch between piezoelectric and sample medium as shown in figure 3.10. Thus the generated wave is reflected back and forth in the layers which decreases the quantity of energy transmitted.

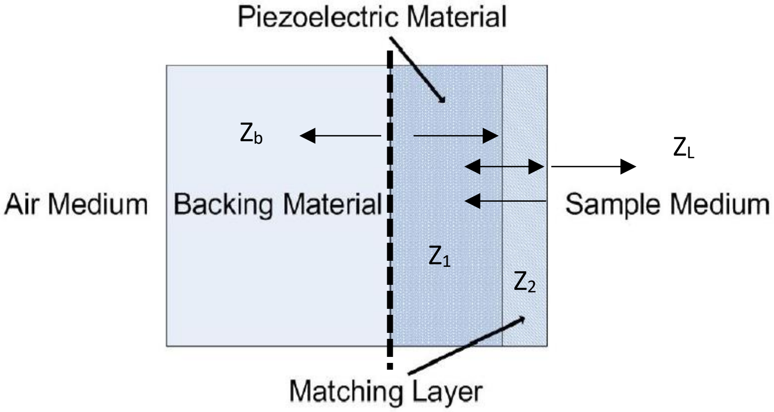

Figure 3.10 Schematics of ultrasonic transducer in contact with the sample medium[Zhu, (2008)]

To reduce the ring-down, a damping material or backing is added behind the piezoelectric element as shown in the fig.3.10. Ideally, the acoustic impedance of the backing material should be equal to that for the piezoelectric material. In such a case, the wave travelling into the backing will be attenuated due to the damping coefficient of the backing material which can reduce the resulting ring down. However, adding backing reduces Q and this reduces the energy transmitted into the sample, limiting the input power and hence the S:N. The impedance mismatch into the sample also reduced energy transmission. To maximize the energy transmitted into the sample medium shown in figure 3.10, it is necessary to perform impedance matching which can be performed using a front surface matching layer.

Matching can be investigated for a plane wave. Consider a wave reflected normally from the interface between two media of different acoustic impedances Z_{01} and Z_{02} and the geometry shown in Fig 3.11. (Kino,1970).

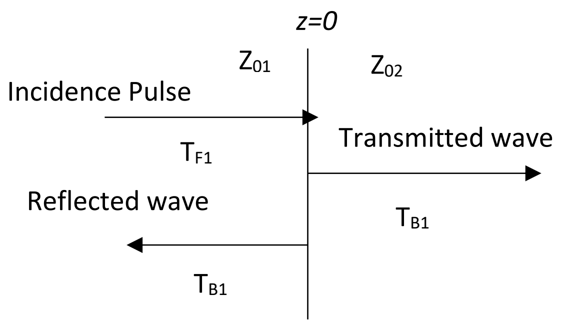

Figure 3.11 Schematic for plane waves normal to an interface

At an interface the mechanical stress T and velocity V will be continuous at the interface. Thus T_1(z) and V_1 (z) on the left side of the interface at z=0 can be written as

$$\begin{aligned} T_1 &= T_{F1}e^{-j\beta_1 z} + T_{B1}e^{j\beta_1 z} \\ V_1 &= V_{F1}e^{-j\beta_1 z} + V_{B1}e^{j\beta_1 z} \end{aligned} \tag{3.5}$$

where β_1 is the propagation constant of medium 1, T_{F1}, T_{B1} are the amplitudes of forward and backward travelling wave on the left side of z=0.

Thus the reflection ratio at z=0 is given by

$$R = \frac{T_{B1}}{T_{F1}} \tag{3.6}$$

From equation 3.5 and 3.6, it can be written as

$$\begin{aligned} T_1 &= T_{F1}(e^{-j\beta_1 z} + Re^{j\beta_1 z}) \\ V_1 &= -\frac{T_{F1}}{Z_{01}}(e^{-j\beta_1 z} - e^{j\beta_1 z}) \end{aligned} \tag{3.7}$$

Similarly, in the region to the right of the interface, there is only an excited wave propagating in the forward direction which can be written as/;

$$\begin{aligned} T_1 &= T_{F2}e^{-j\beta_2 z} \\ V_1 &= -\frac{T_{F2}}{Z_{02}}e^{-j\beta_2 z} \end{aligned} \tag{3.8}$$

The boundary for equation 3.7 and 3.8 at the plane z=0 is that the stress T and velocity V must be continuous. In this way the reflection ratio R and transmission ratio T_R can then be written as

$$R = \frac{Z_{02} - Z_{01}}{Z_{02} + Z_{01}}$$
$$T_R = \frac{2Z_{02}}{Z_{02} + Z_{01}} \tag{3.9}$$

Thus the equivalent input impedance of layer Z_{01} when it is in contact with the Z_{02}, can be given as:

$$Z_{in} = Z_{01} \frac{(e^{j\beta_1 l} + Re^{-j\beta_1 l})}{(e^{j\beta_1 l} - Re^{-j\beta_1 l})} \tag{3.10}$$

Where *l* is the thickness of layer $Z_{01.}$ Equation (3.10) can further be modified as

$$Z_{in} = Z_{01} \frac{(Z_{02} \cos \beta_1 l + jZ_{01} \sin \beta_1 l)}{(Z_{01} \cos \beta_1 l + jZ_{02} \sin \beta_1 l)} \tag{3.11}$$

If the thickness of input layer is quarter wavelength then $\beta_1 l$ from the equation 3.11 becomes π/2; then the equation 3.11 becomes

$$Z_{in} = \frac{Z^2_{01}}{Z_{02}} \tag{3.12}$$

The system described with equation 3.11 forms the basis of the KLM model [Krimholtz et al. (1970)] which will be discussed later. In liquid sodium, the selection of matching layer is also driven by the need to have a material with the ability to give rapid wetting between the surface by liquid sodium. Here, the case of nickel is considered which is used as a faceplate for high temperature ultrasonic transducers due to better wettability in liquid sodium fast reactors [Griffin et al. (2009)]

Using a finite element model, the thickness of the faceplate is varied from quarter of a wavelength to 1/16 of the wavelength and variation in the dynamic response is investigated. Figure 3.12 shows the effect of changing the thickness on the resulting spectrum of the transducer. It can be seen that as the thickness reduces, the resonance frequency increased from 2 to 3MHz. Moreover, the magnitude reduces with the reduction in the thickness of the plate. When the thickness of the plate is quarter wavelength, it can be seen that, at 4 MHz, a minor peak is observed. This peak diminishes in terms of amplitude as the thickness of the plate reduces. There is a visible increase in the -6dB bandwidth of the transducer as the thickness of the faceplate is decreased, but this is at the cost of a shift in the peak frequency and reduction in the amplitude as shown in Figure 3.13.

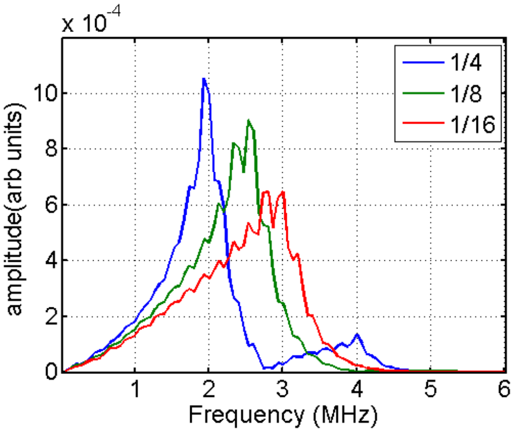

Figure 3.11 Variation of matching layer thickness

The effect of changing front face thickness when the thickness is increased from the quarter wave length to half wavelength and one wavelength is shown in Fig 3.13. It can be seen that as the thickness increases the initial unimodal response becomes a multimodal response with several having significant amplitudes as compared to the amplitude of the peak frequency.

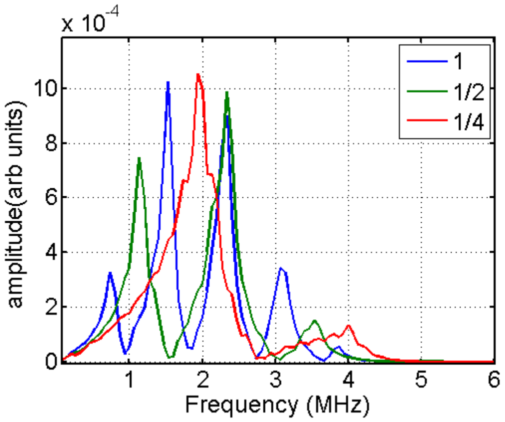

Figure 3.12 Variation in matching layer thickness

3.3 Transmission phenomena through four media; Normal Incidence

In the previous section, the effect of nickel matching layer thickness on the amplitude of the frequency spectrum was studied. An assumption made in calculating the results was that the bonding between the piezoelectric material and the matching layer is perfect and that the thickness of the bond agents does not affect the frequency response of the transducer. The validity of these assumptions is now investigated.

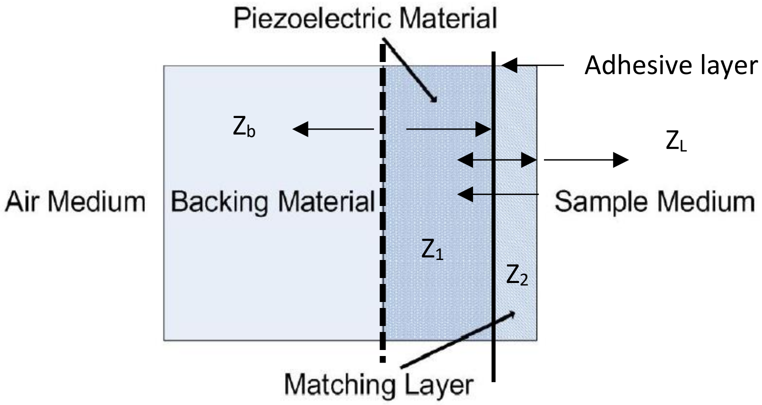

Figure 3.13 Adhesive layer to bond piezoelectric material with the matching layer [after Zhu (2008)]

As stated previously it has been reported in the literature that 60% of high temperature transducers have an adhesion problem between layers. It is therefore necessary to select adhesives and/or other bonding techniques which can provide structural integrity at high temperature. When reviewing the literature there are three different concepts commonly used for acoustic coupling in transducers (Kazys, 2008):

- Dry coupling: High quality surface finish is required. Intimate contact with at worst very small air gaps (>0.01 micron) between a piezoelectric element and a front faceplate. Even a small gap can cause a substantial reduction in energy of the transmitted wave. Moreover, a half-wavelength thick piezoelectric element may not withstand high pressure that may be needed for dry coupling.

- Liquid coupling: Silicon oil has been used successively up to 250C although it evaporates gradually. During long term operation of an ultrasonic transducer, the liquid may flow out of the interfaces due to vibrations of a piezoelectric element. Couplant E (ultra-therm) has already been used in the temperature range of 260C to 540 C. A major issue with using the specialized high temperature couplant’s is that they tend to solidify which reduces the energy being transmitted.

- Solid coupling: In this type of coupling several approaches can be used: soldering, diffusion bonding, cementing, epoxy bonding. The toughness of elastic solder should be able to compensate for differential thermal expansion due to the piezoelectric element, backing element and matching layer.

Thus, it is clear that for high temperature transducers coupling agents are needed between the piezoelectric material and front faceplate. Hence, instead of emphasizing eliminating a bonding the study focused on understanding the frequency response for interfaces with different acoustic impedances. An example of such structure is illustrated in Fig 3.15.

Figure 3.14 Adhesive layer to bond piezoelectric material with the matching layer [Bond, (2013)]

To understand the effect of adhesive on the frequency spectrum of the ultrasonic transducer, the frequency analysis of the pulse echo measurements from the PNNL high temperature transducer was performed as shown in Figure 3.2 and a model to simulate the configuration was developed.

As seen from figure 3.15, solder is used to bond the piezoelectric material to the faceplate. Since the acoustic characterization of solder is difficult, the individual acoustic impedance of the elements in the solder were used in a 1D- KLM model [Krimholtz et al. (1970)] and 2D finite element model in COMSOL™. Comparing figure 3.2 with 3.16(a-b), the frequencies corresponding to the bimodality are in good agreement with the experimental data.

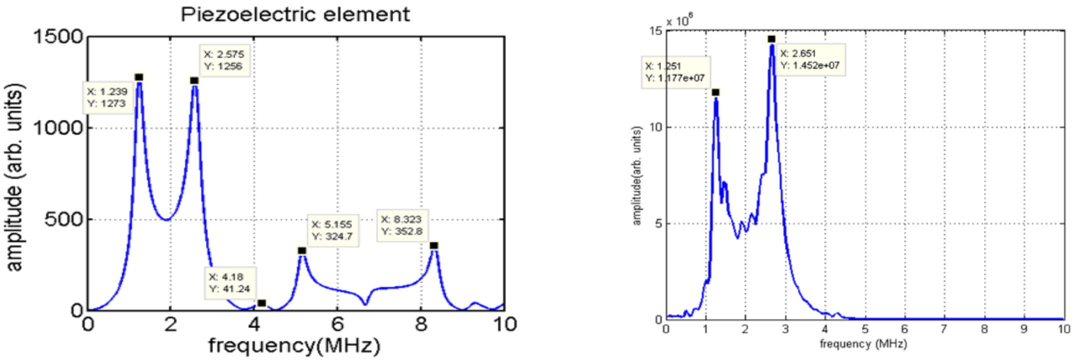

Figure 3.15 Spectral response for a transducer with a multi-layer structure: a) MATLAB™ 1D KLM model and b) Finite element model with interfacial layer containing acoustic impedance of lead (to simulate a solder 0.1 mm thick)

3.4 Transmission phenomena through four media; Normal Incidence, Backing layer effect:

The combination of layers in a transducer were investigated further and compared with some recently published data. The effect of variation of backing acoustic impedance on the bi-modal spectrum was investigated using a 1-D KLM model [Krimholtz et al. (1970)] Resulting data are shown in Fig 3.17. These data show that it is possible to reduce the bipolar nature of the spectrum by increasing the acoustic impedance of the backing material. However, it can be seen that, as the acoustic impedance increases the acoustic energy transmitted decreases. Despite of this, increasing acoustic impedance can be useful since increases the bandwidth of transducer is desired for some applications. The results from the present study are consistent with the work of

Haasz et al (2014) and exhibit similar trends and are in good general agreement. It can be seen that for Zb = 45 MRayls, which is closer to acoustic impedance of stainless steel, this diminishes the bi-modal nature of the response and increases the bandwidth. However, the attenuation coefficient of steel is low, so other approaches are needed to address attenuation and scattering in the backing geometry.

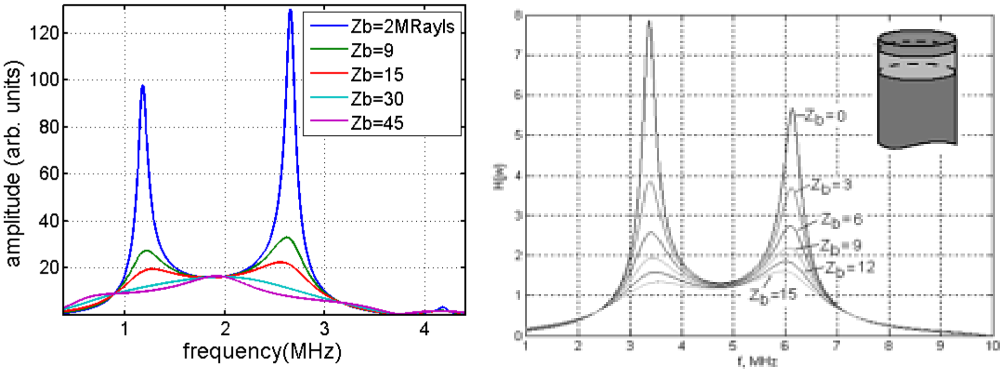

Figure 3.16 Effect of acoustic impedance of backing on bi-modal frequency response (a) KLM model (b) Haasz et al.(2014)

4. Development of BS-PT based High Temperature Ultrasonic transducer

The piezoelectric element is the "eyes and ears" of an ultrasonic transducer. Material selection therefore become critical, particularly for high temperature (200C+) applications. Some materials, such as lithium niobate, although they have some attractive properties they are not considered suitable for in-reactor applications.

In looking at material selection much work just considered d_{33} the electro-mechanical conversion coefficient. However, characteristics of temperature dependence are found to be dependent upon the full-material property matrix of piezoelectric ceramics which have been reported by some researchers [Sabat et al.(2007), Kim et al. (2015), Tang and Cao (2015), Hooker, (1998)]. Such data needs to be utilized to quantify the performance of high temperature (HT) piezoelectric transducers. Eitel et al. (2001) first reported the (1-x) $BiScO_3$-$xPbTiO_3$ at its morphotropic phase boundary (MPB) (x=0.64) as a promising candidate for high temperature applications because of its relatively high piezoelectric response as compared to PZT-5A. Moreover, it has a high Curie temperature due to the small Perovskite tolerance factor of $BiScO_3$ in the solid-solution system with $PbTiO_3$, where Eitel et al. (2007), Gotmare et al. (2008) and Gotmare et al. (2010) reported the thermal degradation and aging of BS-PT material with MPB and tetragonal compositions. Recently, Li et al., (2014) used BS-PT material for high temperature structural health monitoring applications.

In 2014, Roy et al. (2014) developed a temperature dependent, physics based model using experimental data up to 80 C. The objective of this work was to propose a temperature compensation strategy for guided waves. The need to use computer of simulations to predict performance of a HT electro-mechanical device was reported by Tang and Cao (2015).

This section discusses the temperature dependence of BSPT piezoelectric material and acoustic coupling, with physics based model data and pulse-echo contact measurements up to 260 C. An axisymmetric solution for the temperature dependent dynamic response of BS-PT piezoelectric material disc is reported up to 300 C. The physics based model was developed using the frequency domain finite element (FDFE) method in COMSOL software. This work is reported in three sections. Section 4.1 presents fundamental theory regarding the temperature dependence of piezoelectric materials. Section 4.2 describes governing equations and boundary conditions for the predictive modeling of temperature effect on dynamic response of BS-PT piezoelectric material. Section 4.3 reports an experimental set-up and results of pulse echo contact measurements with spectral analysis of the data followed by a conceptual design of transducer.

4.1 Temperature dependence of piezoelectric materials

The strain charge form of linear theory of the piezoelectric effect as given by Jaffe et al. (1971) is described by equation 2.3 and 2.4. The piezoelectric ceramic considered in this section is BS-PT for which equations 2.3 and 2.4 can be represented in matrix form as equation 2.24. Due to the $C\infty$/ C_{6v} symmetry and polarization of BSPT, the complete material matrix reduces to the five elastic, three piezoelectric and two dielectric coefficients as shown in equation (2.24). Thus, the temperature dependent data [Chen et al. (2012), Chen et al. (2014)] for these ten coefficients completely describe the linear theory for the piezoelectric effect under the assumptions that: a) the piezoelectric material remains linearly elastic, and b) the applied electric field and mechanical stress are small which thus implies that this theory is not applicable for large deformations of the piezoelectric material. Sherrit and Mukherjee (2012) have shown that:

$$s_{lk}{}^{E} = s_{lk}{}^{'E}(\omega, E_i, T_j, T, t) + i\ s_{lk}{}^{"E}(\omega, E_i, T_j, T, t) \tag{4.1}$$

$$d_{ij} = d_{ij}{}^{'}(\omega, E_i, T_j, T, t) + i\ \ d_{ij}{}^{"}(\omega, E_i, T_j, T, t) \tag{4.2}$$

$$\varepsilon_{ij} = \varepsilon_{ij}{}^{'}(\omega, E_i, T_j, T, t) + i\ \ \varepsilon_{ij}{}^{"}(\omega, E_i, T_j, T, t) \tag{4.3}$$

Where equations 4.1 to 4.3 show that $s_{lk}{}^{E}$, d_{ij}, ε_{ij} are functions of angular frequency ω, applied mechanical stress T_j, temperature T and time t. The current work considers only the temperature dependency of the elastic, piezoelectric and dielectric coefficients for the finite element model. If the frequency dependent, and electric field dependent data is available, it can be fitted with a polynomial function of the dependent variables to give corresponding values for the material coefficients. From equation 2.24 the temperature dependent piezoelectric response function can be given by:

$$a(t) = f[S_{11}{}^{E}(T), S_{12}{}^{E}(T), S_{13}{}^{E}(T), S_{33}{}^{E}(T), S_{55}{}^{E}(T), d_{15}(T), d_{31}(T), d_{33}(T), \varepsilon_{11}(T), \varepsilon_{33}(T)] \tag{4.4}$$

To evaluate equation 4.4, a physics based model was formulated in COMSOL using a Lagrangian formulation. Reduction in the computational size is achieved by the assumption that the displacement field is symmetric over an axis passing through center of the piezoelectric disc. Further details on modeling of dynamic response of piezoelectric material are discussed in the next section.

Hence, current approach considers temperature dependency of ten material coefficients given by equation (4.4) instead of only d_{33} which was reported previously by Parks and Tittmann (2011) to quantify performance of HT piezoelectric transducers.

4.2 Frequency domain finite element (FDFE) approach

Using time domain finite element techniques, electrical impedance of a piezoelectric material can be computed from transient data of output voltage and current. Using a fast Fourier transform, the dynamic response of the electrical impedance can then be calculated. However, wave-propagation studies in the time domain are computationally costly and require a convergence study to set the time step and the maximum element size. By contrast the FDFE approach is basically a pseudo-static problem that requires no time stepping, Chillara et al. (2016). In current work FDFE approach is used to simulate the temperature dynamic response of piezoelectric material. The geometric configuration of the problem is given by Figure 4.1

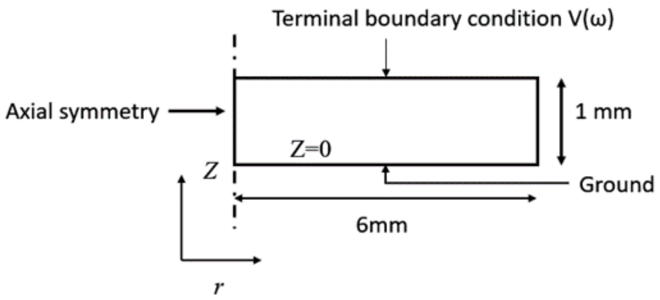

Figure 4.1 Geometric configuration of the problem

4.2.1 Linear momentum balance for piezoelectric material in frequency domain

The direct and converse piezoelectric effects are modelled using equations 2.1 and 2.2 respectively which were discussed in Section 2. The mechanical displacement field $u(r,\emptyset,z)$ is symmetric about axis Z. The FDFE approach assumes a time harmonic nature for the displacements $u=u(r,\emptyset,z)\ e^{iwt}$ and stress $\sigma=\sigma(r,\emptyset,z)e^{iwt}$ in the cylindrical space co-ordinate system. The e^{iwt} describes the harmonic nature of the variable. Thus, the equation of linear momentum balance in the frequency domain is given by

$$\rho\omega^2 u + \nabla\cdot\sigma = F_v e^{i\phi} \tag{4.5}$$

where ρ is the assigned material density, ω is the circular frequency for frequency sweep, F_v is the body force. The poling axis of the BSPT is aligned with z axis of the model. Z=0 and Z=1 surfaces, shown in Fig. 4.1 are kept traction free ($\sigma_{zx}=\sigma_{zz}= \sigma_{xx}=0$).

4.2.2 Electrostatics

For the piezoelectric material, as stated previously the electric field is assumed irrotational. Thus, the electric field *E* is related to the scalar electric potential *V* given as [COMSOL (2014)]

$$E = -\nabla V \tag{4.6}$$

$$n \cdot D = 0 \tag{4.7}$$

Zero charge constraint is assigned in the domain $\mathbf{\Omega}_{\text{piezo}}$ at boundaries x=0 and x=3. Charge density ρ_v in the domain $\mathbf{\Omega}_{\text{piezo}}$ is given by [COMSOL (2014)]

$$\nabla \cdot D = \rho_v \tag{4.8}$$

4.2.3 External electrical Circuit for the instrumentation impedance

In experimental resonance measurements the piezoelectric material is connected to an impedance analyzer using lead wires soldered to the metal electrodes. This introduces potential electrical impedance mismatch between the piezoelectric material and the impedance analyzer. This effect is modelled by introducing a resistor of impedance equal to the impedance analyzer. In the current study, the impedance value of resistor is set to an ideal 50 **Ω** between node 1 and 2. The electric circuit module in COMSOL is then used to evaluate global variable voltage as a function of frequency sweep. In this model an AC voltage of amplitude 1V is applied to the piezoelectric material using an external current coupling of the terminal boundary condition assigned to piezoelectric material.

The current on the piezoelectric electrode surface $\partial^D \Omega_{piezo}$ is defined as [COMSOL (2014)]

$$\int_{\partial^D \Omega_{piezo}} D \cdot n = Q_0, \frac{dQ_0}{dt} = I_{cir} \tag{4.9}$$

Hence, the voltage on the electrode surface $\partial^D \Omega_{piezo}$ is given by [COMSOL (2014)]

$$V_{pz}(\omega) = V_{source}(\omega) - I_{cir} R \tag{4.10}$$

Using the frequency dependent voltage and current, the electrical admittance can be calculated and plotted as a function of frequency.

4.2.4 Discretization

Quadrilateral elements of size 0.01mm were used for the mapped meshing of the complete domain $\mathbf{\Omega}_{\text{piezo}}$. Total number of elements are 32,000 with average growth rate and average element quality equal to 1. The maximum grid element size is related to other parameters using the relationship [Bilgunde and Bond (2015)]

$$h_{\max} = \frac{c}{f_0 N} \tag{4.11}$$

where h_{max} is the maximum element size, c is the shear wave speed in the piezoelectric material, f_0 is the highest frequency in the desired spectrum, N is the number of elements per wavelength. The frequency step for the sweep is set to 1/500 of the highest frequency in the sweep. This increases the number of sample points in the impedance spectra and hence improves the resolution of the simulated data.

4.3 Model results

Ferroelectric ceramics exhibit both intrinsic and extrinsic contributions to the piezoelectric effect [Li et al. (1991)]. This effect, described by equations 2.1 and 2.2, is dependent upon the elastic, dielectric, and piezoelectric coefficients. Hence, the magnitude of these coefficients is dependent on the extrinsic and intrinsic properties of the ceramics [Randall et al. (1998)]. In the FDFE approach electrical admittance, capacitance and electric charge are evaluated to quantify the temperature dependence of intrinsic and extrinsic contribution to the piezoelectric effect.

The current physics based model utilizes the temperature dependent experimental data for the BS-PT material given by Chen et al. (2012) in the morphotropic phase boundary condition (MPB). The MPB is an almost-temperature-independent phase boundary that separates tetragonal crystal structure (P4mm) and a rhombohedral structure (R3c) [Randall et al (1998)]. Batch simulations are performed in COMSOL to change the material matrix of the BSPT material corresponding to the predefined temperature. The temperature dependent dynamic response of real and imaginary part of electrical admittance are shown in Fig 4.2 (a-b). As the temperature increases the conductance of the piezoelectric material increases. The data shows an increase by a factor of 2.7 from 15 to 300C.

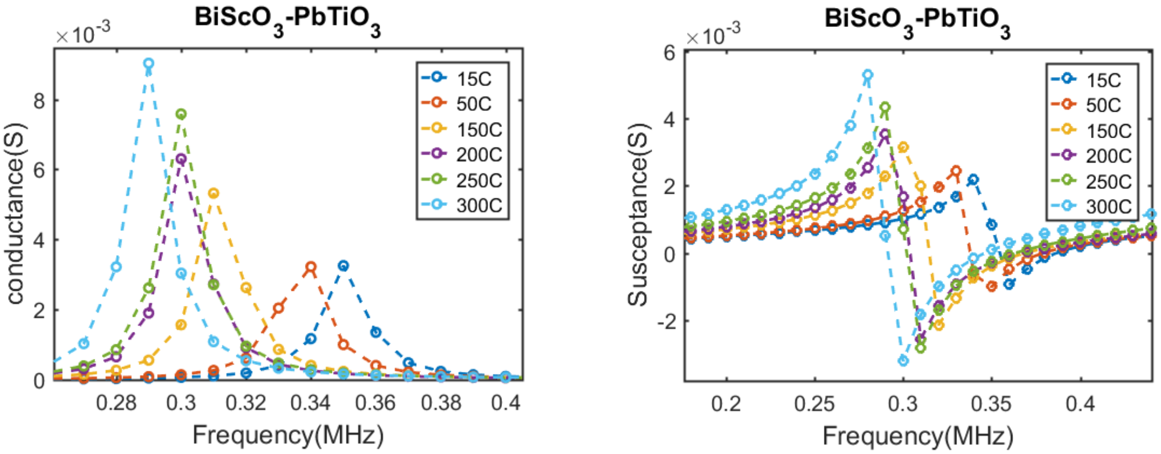

Figure 4 2 Dynamic response of a) conductance b) susceptance due to temperature dependent piezoelectric material matrix

Model results given in Fig.4.2(b) shows an increase in the susceptance as a function of temperature. Admittance is a reciprocal of electrical impedance. This indicates that as the temperature increases the electrical impedance of the BSPT material decreases.

The spontaneous polarization P of the piezoelectric material is related to electric field E and electric displacement D and there relationships are described by Haun et al. (1987)

$$D_m = \varepsilon_0 E_m + P_m \tag{4.12}$$

$$P_m = \varepsilon_0 (\varepsilon_r - I) E_m + e\varepsilon \tag{4.13}$$

$$P_m = \varepsilon_0 \chi E_m + e\varepsilon \tag{4.14}$$

where χ represents the dielectric susceptibility of the piezoelectric material.

Experimental data obtained with equipment in the Department of Material Science at Iowa State University for the dielectric constant of BSPT piezoelectric ceramic disc as a function of frequency and temperature is shown in Fig 4.3. The dielectric constant increases with temperature indicating an increase in the dielectric susceptibility which can be understood from the relationships given in equations 4.13 and 4.14. Capacitance of the piezoelectric disc is directly proportional to dielectric constant for a constant area and thickness of the disc. Thus, it can be expected from the relationships given as equations 4.13 and 4.14 and as seen in the experimental data in Fig. 4.3(a), an increase in dielectric susceptance due to temperature increase should increase the capacitance of the BSPT disc. The predictive model developed using the FDFE approach estimates this increase in the capacitance of BSPT disc as a function of temperature shown by Fig.4.3(b).

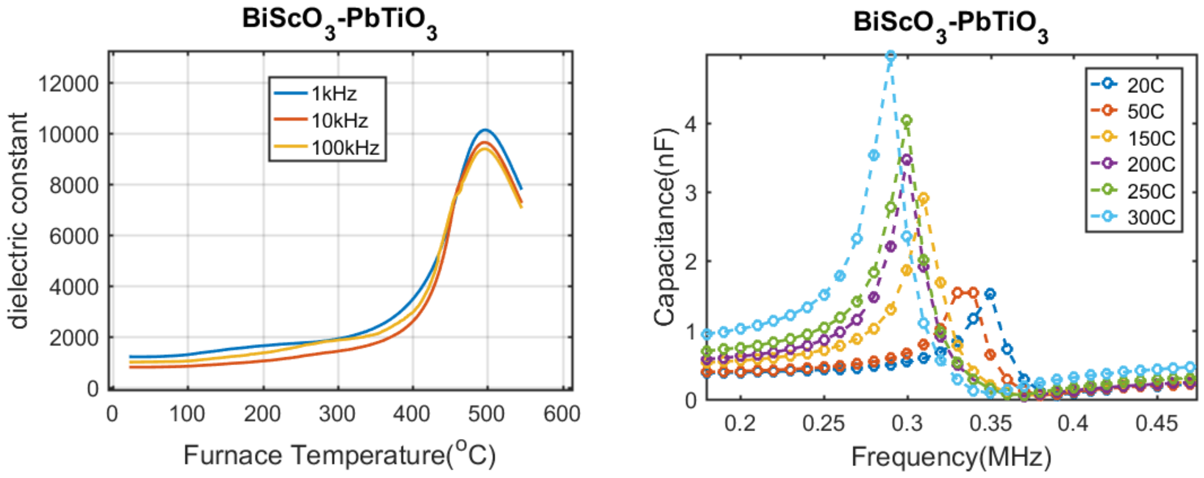

Figure 4.3 Temperature dependent

a) Experimental data of dielectric constant

b) Capacitance (model data)

The model data given in Fig 4.3 shows an increase in the capacitance magnitude from 15 to 300C by a factor of 2.2. This increase in the capacitance of the dielectric indicates that an increase in electric charge storage will be seen. From the previous discussion, this implies that, with BSPT, the increase in the temperature will increase the electric charge stored by the piezoelectric material. Figure.4.4 shows increase in the electric charge computed from model definition (*es.Q0_1*) in COMSOL for BSPT from 15C to 300 C. The electrical charge was calculated for a range of frequencies as a function of temperature. The data show an increase in charge and a frequency shift to lower frequencies as temperature increases.

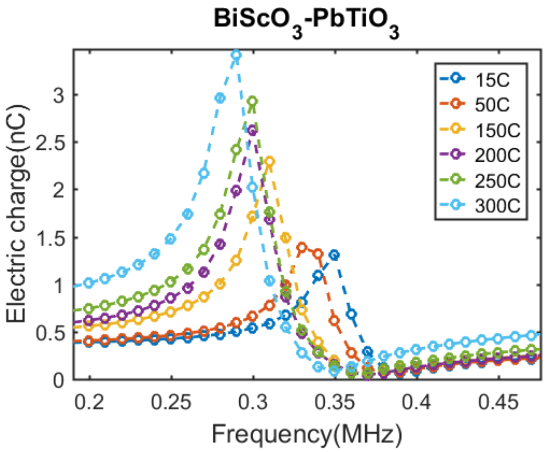

Figure 4.4 Simulation data for dynamic response of BSPT for temperature dependence of electric charge

The transducer model and pulse-echo response for the 2D axisymmetric time domain finite element model described in Section 2 was calculated using data for BSPT and this was compared with base-line data for the case of PZT-5A. Using temperature dependent data for PZT-5A (Sabat, 2007), responses were calculated and results are given in Fig 4.5a. It is estimated that a 4 dB reduction in the amplitude of transmitted pulse is estimated as the temperature of PZT-5A is increased from 15^0C to 195^0 C.

Temperature dependent property data published by Chen et al. (2014) were used to estimate signals to 300C and data are given in Fig 4.5b. The simulated response for a transducer using a BSPT [[(1-x) $BiScO_3$-x$PbTiO_3$] element in the morphotropic phase boundary composition, shows only 2dB transduction loss when the temperature is increased from room temperature to 300^0C. Moreover, the amplitude of the transmitted pulse shows negligible loss till 200^0C which indicates that the BSPT potentially has larger range of temperature over which transduction ability remains stable, as compared to the response with PZT-5A [Bilgunde and Bond (2016)].

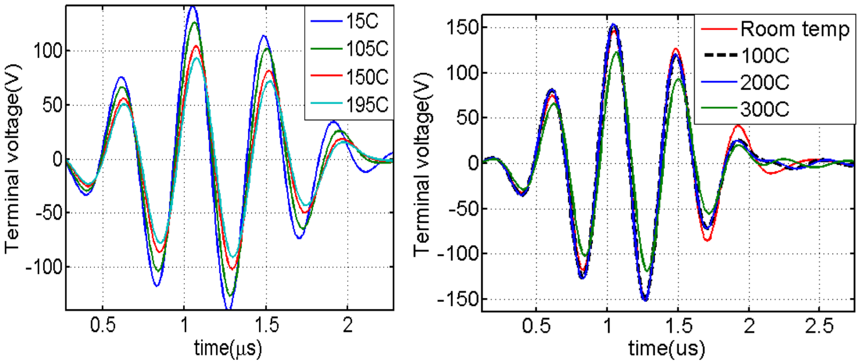

Figure 4. 5 Temperature dependent incidence pulse for a) PZT-5A b) (1-x) BiScO3-xPbTiO3

Using the numerical study discussed in chapter through 4, fundamental parameters in ultrasonic transduction which affect signal strength were studied. Using the simulation results, BS-PT piezoelectric material was selected for preliminary high temperature ultrasonic measurements which will be discussed in detail in next section.

5. High temperature in-situ ultrasonic measurements up to 260C for multiple thermal cycles

In Section 4 a predictive modeling methodology was used to estimate dynamic and transient response of a transducer fabricated using a piezoelectric material BSPT [(1-x) $BiScO_3$-$xPbTiO_3$]. The model predicted only a 2dB loss in the amplitude of the ultrasonic signal up to 200C. The experimental data on measurement of dielectric constant demonstrated the *surge point* of more than 300C [Bilgunde and Bond (2017)] which meets the hot stand by temperature requirement for liquid sodium fast reactors of 260C. In addition to element material the temperature dependent performance of interfaces is also a critical issue [Kažys, (2008)] which affects the transmissivity of the ultrasonic signals as quantified in the Section 2. To investigate performance a series of measurements were performed to investigate high temperature dry contact.

5.1 Experimental Set-up preparation

The schematic of the experimental set-up for the high temperature pulse-echo contact measurements is shown in Fig 5.1. The thickness of BSPT material is 0.9mm and diameter is 19.0 mm (0.75 inch). A 0.2 mm (0.008-inch) diameter nickel lead wire is connected to the top electrode of BSPT using Duralco 124 [Dhutti et al. (2016)] which is a silver based conductive two components epoxy paste. The bond is cured in an oven at 120 C for two hours with post cure heating of the bond for additional two hours at the same temperature. The conductivity is tested using the electrical continuity mode on a digital multi-meter.

The ground connection is established by using Pyroduct-597A [Giurgiutiu et al. (2010), Amini et al. (2016)] which connects the nickel wire to a 12.5 mm thick, cold drawn low-carbon steel block. The bond is cured at 120C for two hours. High temperature alumina ceramic tube is used as insulation/separation in the top of the furnace to prevent electrical short circuits between the nickel lead wires.

The critical challenge of the experiment is to investigate acoustic coupling between the BSPT and carbon steel block. A two-part epoxy (Epotek 353ND) is used as a coupling agent for high temperature. The maximum rated temperature of Epotek 353ND for continuous operation is 250 C and 350 C for intermittent operation. The bond using Epotek 353ND is cured at 150C for one hour in the oven.

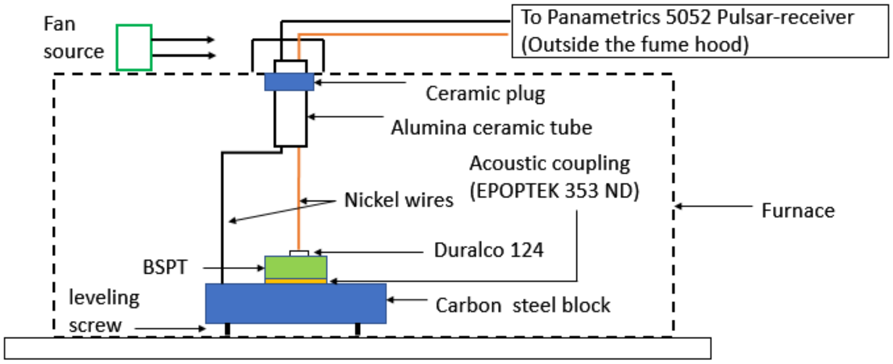

Figure 5.1 Schematic of the Experimental set-up for high temperature Pulse echo contact measurements

A simplified circuit diagram for the pulsar receiver (P-R) is shown in Fig 5.2 [Schmerr (1998)]. The transmitted and received pulse data acquired from the transducer is dependent upon the energy, damping gain and filter settings of the P-R. In the current experimental set-up a Panametrics 5052x P-R is used to excite the transducer with a spike of 100V (energy setting). The damping resistance (R_d) is adjusted to 50Ω. Gain setting is set to 16dB and the high pass filter is adjusted to the *out* setting. The pulse repetition frequency was set to the 4 setting. The pulse-echo data from the transducer is monitored, displayed and recorded using an oscilloscope (LeCroy HDO 4034) with 450 MHz sampling frequency and 12-bit verical resolution. The data was averages 512 times averaging to filter random electrical noise.

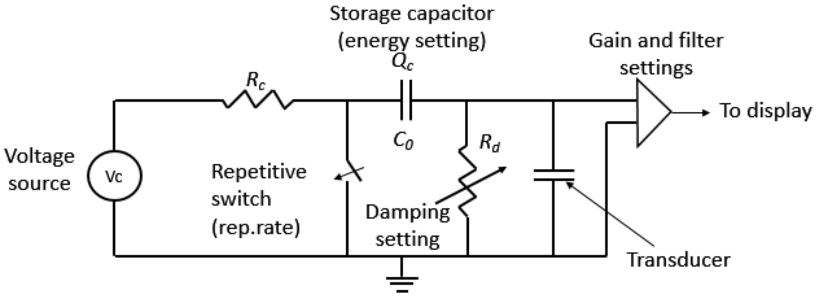

Figure 5. 2 Simplified diagram of pulsar -receiver (recreated from Schmerr,1998)

5.2 In-oven pulse-echo measurements of BSPT attached to the 1018 low carbon steel block

The high temperature pulse-echo contact measurements are performed in an electrical furnace [Barnstead Thermolyne furnace type 47900]. The set point of the furnace was defined as 260 C. The temperature is increased from 20 C to 260C at a 5 C/min rate. The hold (dwell) time at 260C was set to be 20 minutes.

As the experiment proceeded the P-R settings were not modified during the contact ultrasonic measurements. The averaged waveform is saved in the oscilloscope memory in the comma separated values(CSV) file format for every 10C increase in the furnace temperature. The resulting data were transferred to a PC and the results showing the temperature effect on the averaged waveform representing the first backwall echo from the carbon steel block are given as Fig 5.3a. It can be seen that the arrival time of the first back-wall echo increases with longitudinal velocity change of BSPT, acoustic coupling and the steel block as a function of temperature

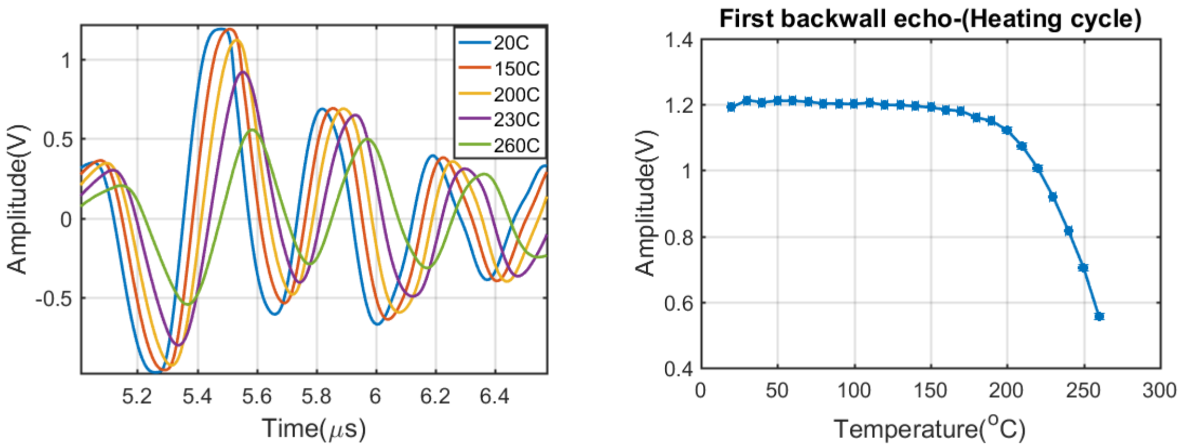

Figure 5.3 Pulse-echo signal - First back wall echo a) time domain signals b) Peak amplitude as a function of temperature

Peak amplitude was considered as a function of temperature and in reviewing data given in Fig.5.3(b) it exhibits a reduction in the amplitude of the first back-wall echo as the temperature is increased from 20 to 260C during the heating cycle. The magnitude of the signal reduction is 6dB between 20 and 260C. The magnitude is nearly constant up to 150C and then the rate of reduction in the amplitude increases considerably above 200 C. The spectral characteristics of the time domain data were investigated using an FFT and the data given in Fig. 5.4 shows the effect of temperature on the spectral content of the first back-wall echo.

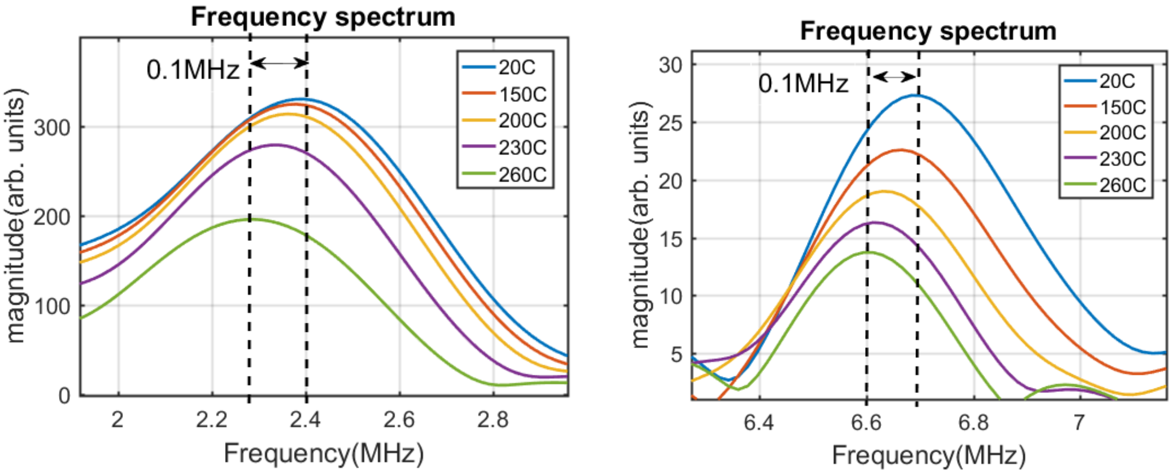

Figure 5.4 Temperature effect on a) Fundamental frequency resonance b) partial third harmonic resonance

The data in Figure 5.4(a) exhibits a shift to a lower frequency of 0.1 MHz at 260C when compared with the fundamental resonance frequency of the structure at 20C. Similarly, a 0.1 MHz shift to a lower frequency is observed for the partial third harmonic of the structure at 260C as shown in Figure 5.4(b). The observance of partial third harmonic might be due to the absence of backing layer (damping material) on the top of back electrode increasing the sensitivity of the 3rd harmonic.

The ultrasonic dry contact measurements were repeated for five thermal cycles with the same experimental set-up as shown in Figure 5.2. The peak amplitude for the second back-wall echo was measured. For the 4th and 5th thermal cycle 10 dB gain is added to the pulsar-receiver to improve signal resolution above the system noise. and the data are shown in Fig 5.5. Interestingly, the amplitude of second back-wall reduced by at least 6 dB after the first heating to 260 C.

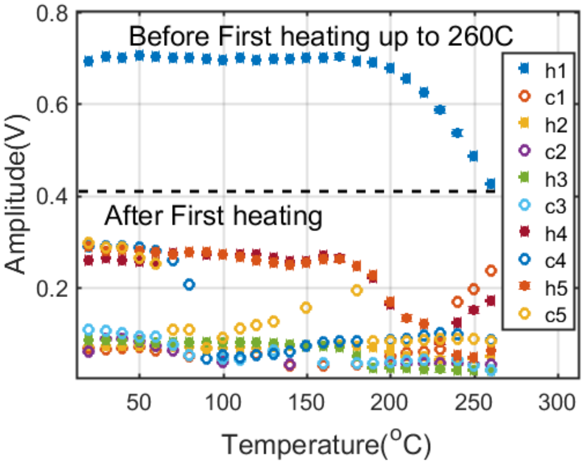

Figure 5.5 Peak amplitude of second back-wall echo for five thermal cycles (Heating+ cooling)

The amplitude of second back-wall after the first heating was measured and exhibited similar trends. After the fourth cycle amplitudes reduced and 10 dB gain was added to the receiver.

To investigate potential structural changes both longitudinal and shear wave C-scans of the interface were performed using the experimental set-up shown in Figure 5.6. The pulse-echo measurements are performed with Panametrics 311, 10 MHz, 12.2 mm (half inch diameter) transducer with a nominal 50.8 mm (two inch) focal length in water The transducer is set with the focal spot on the interface and the transducer operated with a Panametrics model 5077PR square wave pulsar-receiver. The pulse-receiver settings were 18dB gain and 100V pulsar voltage. The low pass filter setting is set at full bandwidth and the high pass filter is not used

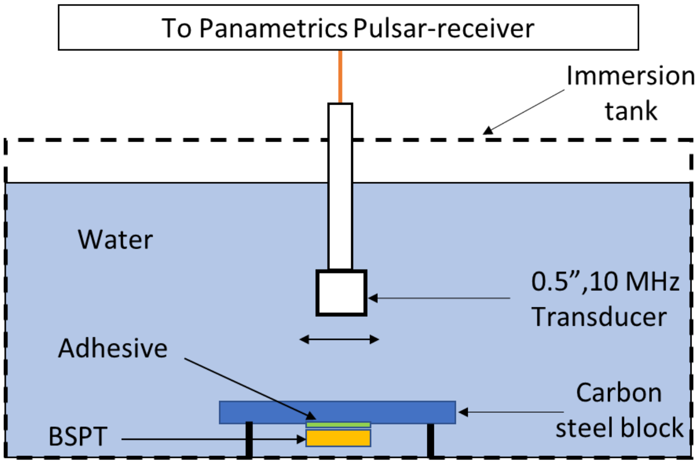

Figure 5.6 Experimental set-up for the acoustic scan of the BSPT-steel interface

The longitudinal wave C-scan image using amplitude data is shown as Figure 5.7(a) with a photograph of the element attatched to the steel shown as Figure 5.7(b). Figure 5.7(a) show no significant change in the amplitude of reflected signal in the spatial location of the interface at room temperature. The C-scan does not indicate any significant disbonding in the interface region after cooling the interface to room temperature (20C).

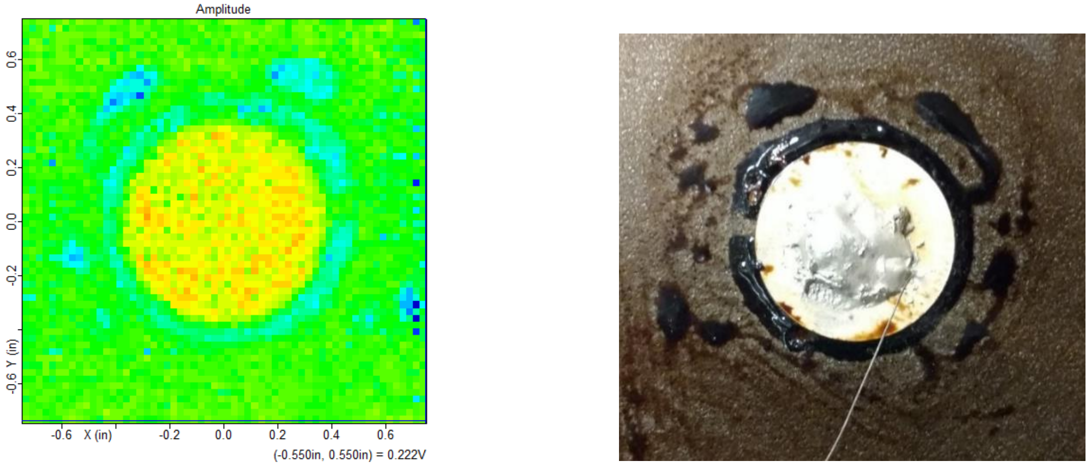

Figure 5. 7 BSPT c-steel interface image
a) Longitudinal wave C-scan of the interface *b) image of the element on steel interface*

SUMMARY AND CONCLUSION

The transduction ability of the active element in an ultrasonic transducer is due to the piezoelectric effect and is usually considered in terms of the d_{33} coefficient. Transducer materials have multiple constants which contribute to estimating transducer performance. In this study a predictive model was developed using a frequency domain finite element (FDFE) approach that includes the temperature dependency of all ten material coefficients and this was used to evaluate the electrical admittance, capacitance and electric charge. The model gave data that were used to quantify the temperature dependence of the intrinsic and extrinsic contributions to the piezoelectric effect. It was seen in the data that as the temperature increased from 15C to 300C there are increases in the conductance and susceptance when data for BSPT material are used.

The model results also show an increase in the capacitance as the temperature increases and these data are in agreement with the experimental data which shows an increase in the dielectric constant. The model shows that from 15C to 300C as the capacitance increased the electric charge also increases.

High temperature pulse-echo contact measurements were performed up to 260C which is the hot stand by temperature for liquid metal cooled reactors, to study the performance of the acoustic coupling agent and the BS-PT piezoelectric material bonded to a low-carbon steel specimen. Experimental measurements indicate a 6dB reduction in amplitude of the first back-wall echo for contact measurement from 20 to 260C. A significant reduction in the amplitude of the signal is seen to occur with an increase from 200C to 260C. In reviewing the data, a 0.1 MHz reduction in peak frequency is seen for the spectral content of the first back-wall echo. The acoustic C-scan of the interface did not indicate any significant dis-bonding. However, detail spectral and transient analysis of the waveform is required for the assessment of BSPT material and bond state during heating and cooling.

6. High Temperature Ultrasonic Immersion Measurements Using BS-PT Based Ultrasonic Transducer Without Delay Line

In previous section dry contact ultrasonic measurements were performed up to 260C. The experimental data exhibited a reduction in the peak amplitude above 200C and by 260C dropped to be -6dB below the room temperature amplitude. In this chapter, the development a single element of high temperature transducer is discussed in Section 6.1. Section 6.2 describes experimental immersion measurements and section 6.3 shows the effect of temperature ultrasonic measurements in terms of time of flight change and peak of amplitude of front wall-echoes.

6.1 Development of high temperature immersion transducer

The schematic of the transducer design and a photograph of the resulting transducer which was developed are given in Figure 6.1 (a-b)

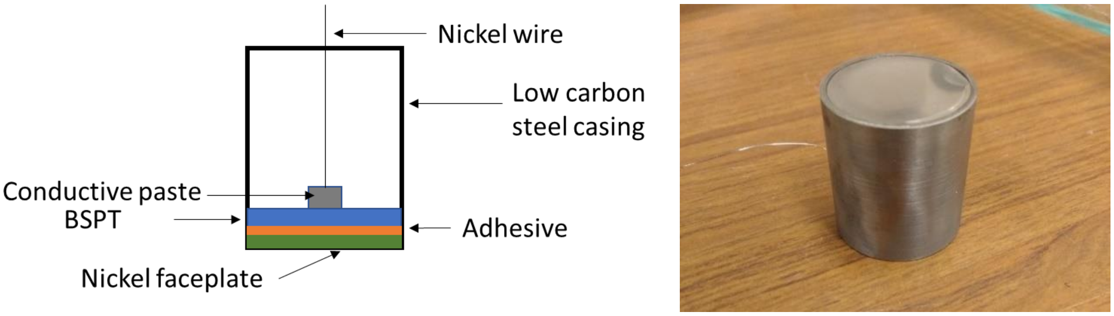

Figure6.1 a) Schematic of the transducer design *b) Photograph of final transducer developed*

6.1.1 Piezoelectric material selection

In section 2 a pulse-echo model gave simulated results for a 2.25 MHz resonant frequency and 19mm diameter transducer which exhibited a 2dB reduction in amplitude for a BSPT based transducer due to material property changes with temperature at 300 C. Using the data by Sabat et al. for PZT-5A upto 195C, a similar transducer model exhibited a 4dB reduction at 195C. The experimental data for dielectric constant variation as a function of temperature also showed a surge point at a temperature above 300 C for BSPT [Bilgunde and Bond (2017)]

6.1.2 Faceplate material

For operation of a transducer in liquid sodium efficient wetting of the front face is critical. Other studies (Griffin et al., 2012) have shown that nickel has the required wettability and mechanical properties, and this is the front face material used in the PNNL high temperature transducer. In the current study nickel was selected as the face-plate and a quarter wavelength thick disc is bonded to the BSPT piezoelectric material [Bilgunde and Bond (2017)]

6.1.3 Bonding/Adhesive

In the prototype transducer development, a two-part epoxy (Epotek 353ND) is used as the bonding agent between the element and front face matching layer for high temperature experiments. The maximum rated temperature of Epotek 353ND for continuous operation is 250C and 350 C for intermittent operation.

6.1.4 Backing layer and casing

The transducer design shown in Figure 6.1 is air-backed and it does not contain a backing layer. An air-backed design increases the acoustic energy transmitted into the load or liquid which is necessary for maximizing capabilities for NDT and imaging. It also eliminates a potential interfacial bonding issue between the piezoelectric element, the need to identify and implement a backing material with appropriate damping and scattering/attenuation properties.

A transducer based on a piezoelectric transducer needs to be mounted and attached to a suitable case. The theory for such a transducer and the theory to predict the resulting wave field is well established [Kino (1987)]. In the current study, a 24mm diameter and 2mm thick steel casing is used for outer body of transducers. The nickel shim is attached to the casing using epoxy.

6.1.5 Electrical connectivity

For the air backed transducer a 0.20 mm (0.008-inch) diameter nickel lead wire is connected to the top silver electrode of the piezoelectric using a silver based conductive two components epoxy paste [Duralco 124]. The effectiveness and electrical conductivity was measured by checking resistance using a digital multi-meter. Electrical ground is achieved by directly attaching the ground of a BNC cable to the casing. Alumina ceramic tubes were used to provide insulation between the nickel wire attached to the back electrode and the transducer casing. A final transducer incorporates an end cap and a BNC or other connector rated for high temperature operation.

6.1.6 Fabrication of transducer

Each transducer is assembled in a specific sequence and tests performed at each step to ensure proper function. The piezoelectric element is first selected and electrodes are cleaned to avoid issues with bonding due to contamination, such as that due to oils from handling.

Of primary importance is ensuring the electrical connection between the piezoelectric element (BSPT) and the pulsar receiver. The first step is to join a nickel lead wire to the electrode on the piezoelectric element using the silver based conductive paste. The bonding compound is cured in oven at 120 C for two hours with post-cure heating of the bond for additional two hours at the same temperature. This is followed by the bonding of nickel faceplate to the front electrode of the piezoelectric material (BSPT) using a thin layer of high temperature epoxy. The bond using Epotek 353ND is cured at 150C for one hour in an oven. Using same high temperature epoxy the assembly of nickel, BSPT and the lead wire is attached to the casing at the final stage. An alumina ceramic tube placed around the wire attached to the back electrode. A final transducer incorporates an end cap and a BNC or other connector rated for high temperature operation.

6.2 Experimental set-up

A schematic which shows the experimental set up used for the immersion measurement is given as Fig 6.2. A borosilicate glass vessel was used to contain the liquid used in the measurements. A K type thermocouple is immersed in the liquid for the temperature measurement of the liquid at a fixed spatial region of the vessel.

The target specimen is a 7mm thick 1018 low carbon steel material. The specimen is kept on a stand to avoid reflection from the bottom of glass vessel. This also provides a flat surface for the normal incidence-reflection measurements.

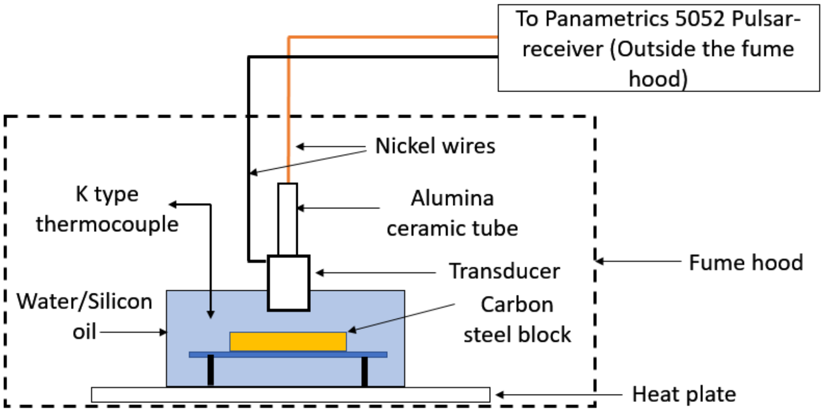

Figure 6.2 Schematic of the experimental set-up for high temperature ultrasonic immersion measurement

The glass vessel is heated using a Thermo-Fischer™ heat plate set in a fume hood as shown in the figure 6.3. The temperature is increased by 5 C/min rate until the temperature of liquid measured by K type thermocouple ($\pm 5C$) achieves desired temperature.

The transducer is set normal to the reflector at a range of 15 mm for water and 20mm for oil. A Panametrics 5052 pulsar receiver is used with energy setting at 1, damping at 5, gain of 40dB and repetition rate at 4. A high pass filter is set at 0.3MHz to remove low frequency noise. Pulse-echo ultrasonic data is collected at 10 C interval and sampled at 500MHz using the HDO 4034 oscilloscope at a fixed spatial location. The data is averaged 256 times to reduce random electrical noise

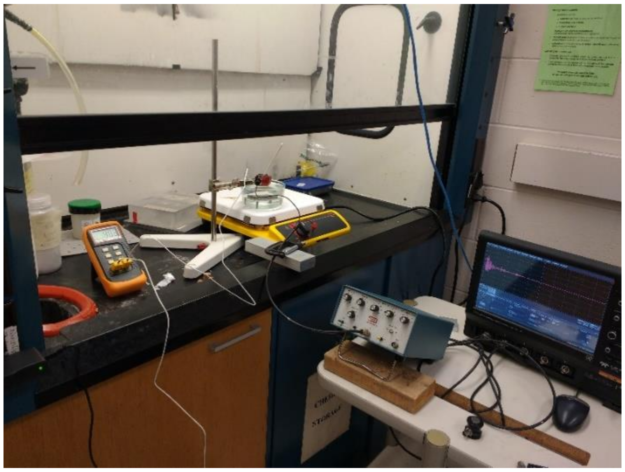

Figure 6.3 Actual experimental set-up

6.2.1 Ultrasonic immersion measurements in water

Initial measurements were performed with water. Examples of A-scan data for the first heating cycle of the transducer in water at 32, 52 and 92 C are shown in Fig 6.4. It can be seen that the amplitude for first, second and third echoes reduces significantly at 92C and this is believed to be due to bubbles which appeared on the transducer front face To further investigate the significant reduction in the echo amplitude at 92C further thermal cycles of measurements were performed with the same transducer.

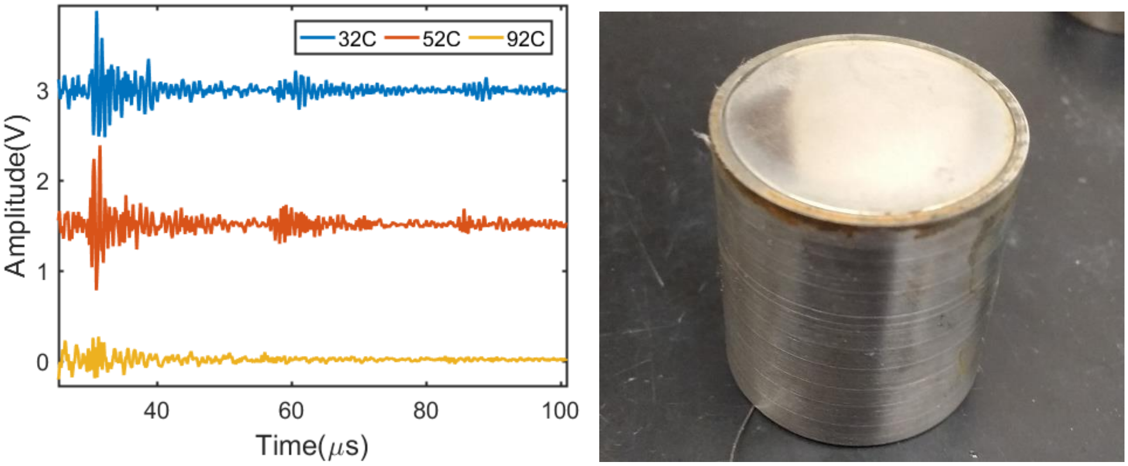

Figure 6.4 a) Immersion measurements in water during first heating b) Rust developed due to oxidative reaction of low carbon of steel with water

It was also found that some rust developed on the transducer casing after the first heating measurements are completed and this is shown in the photograph given as Fig 6.4.b. This rust is due to the oxidative reaction between water and low carbon steel. The rust was removed using a sand paper before next cycle of measurements were performed. It was observed that heating of the water caused dissolved gases to form bubbles as shown in the Figure 6.5(b) and these adhered to the faceplate of the transducer. The gas bubbles highly attenuate the transmitted energy into the liquid reducing the amplitude of the echo. This is also evident from the A scan data for the third heating cycle as shown in Figure 6.5(a).

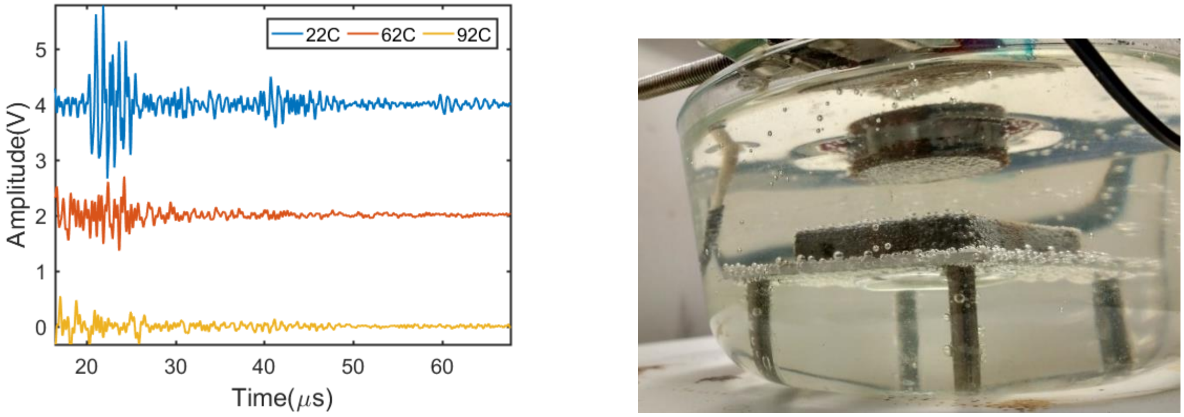

Figure 6.5 Attenuation due to degassing in 3rd cycle a) A-scan data b) Actual degassing during the measurement at 82C

The rust which developed on the ultrasonic transducer after the third heating cycle is shown as Fig 6.4 and Fig 6.6. To avoid further potential damage to the transducer and to address the bubble formation, as well as increase the test temperature range the liquid was changed to be silicone oil for which results will be discussed in next section.

Figure 6.6 Rust developed on the Ultrasonic transducer after third heating cycle due to the oxidative reaction of low carbon steel casing with water

The immersion measurements in water were repeated for three thermal cycles. Examples of data are given in Figure 6.7 shows peak amplitude of the first front wall echo for 3 thermal cycles.

The increase in peak amplitude shown in the data in Fig. 6.7 for cycle-1 at 62C and for cycle 3 at 82C was due to external cleaning of gas bubbles from the faceplate of the transducer.

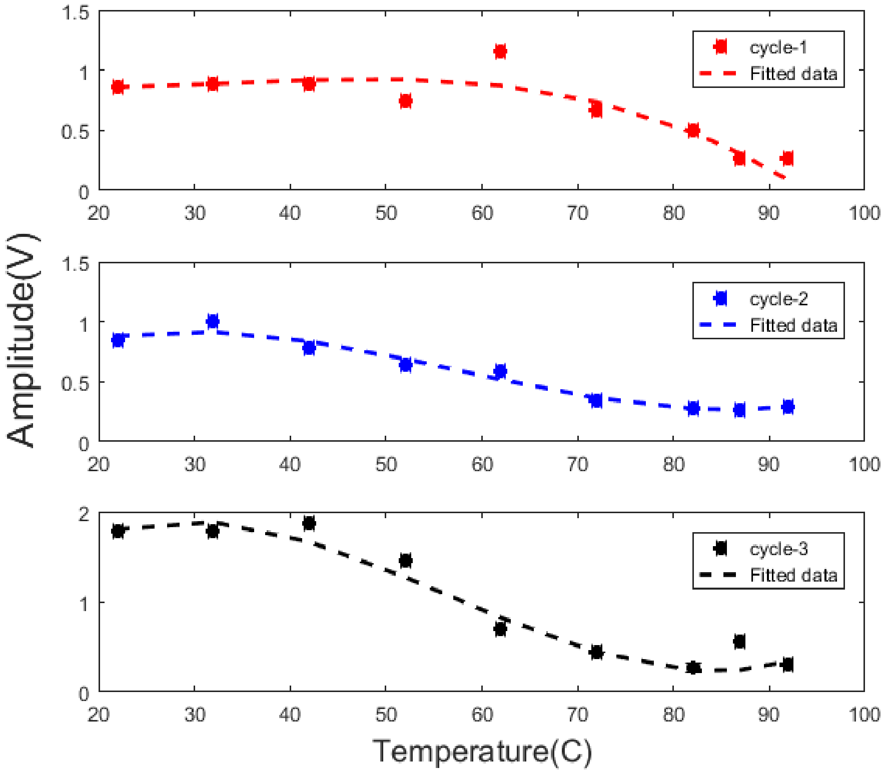

Figure 6.7 Pulse-echo measurement in water for three thermal cycle indicate non-linear drop in the first-wall echo amplitude due to the generation of gas bubbles adhering to the faceplate of the transducer

Fig. 6.8(a) shows the mean value of peak amplitude from three thermal cycles with error bars. The variation in amplitude at lower temperature is influenced by the alignment of the transducer, distance between transducer and reflector for each thermal cycle. At temperatures above 90C the error is as the gas bubbles adhere to the faceplate in each thermal cycle in this temperature range indicating the strong influence on the peak amplitude. The sensitivity of the transducer is given by Kibe et al. (2015)

$$sensitivity = -\left(20\log_{10}\frac{V_1}{V_2} + gain\ of\ pulsar\ receiver\right)dB \qquad (6.1)$$

The sensitivity of the ultrasonic transducer was calculated in water as a function of temperature with a reference voltage *(V_2)* as 1 Volt. V_1 is the peak amplitude of the first front wall echo from the RF signal. The mean of sensitivity of transducer from three thermal cycles reduces as the temperature increased and data are shown as Fig. 6.8.

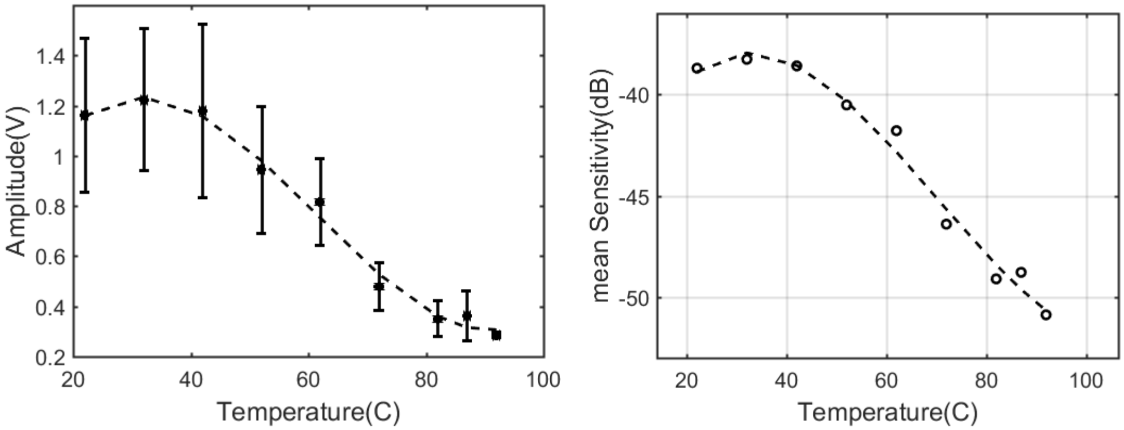

Figure 6.8 Sensitivity of the Ultrasonic immersion transducer in water as a function of temperature

6.2.2 Ultrasonic immersion measurements in oil

The experimental procedure and instrumentation used reported for water was repeated but using a silicone oil (85409 SIGMA-ALDRICH™) and data recorded at 22, 82 and 142 C. The RF data for immersion measurements in silicone oil for five thermal cycles using the same transducer as used in the water, for three thermal cycles are given in Figure 6.9(a) through 6.11.

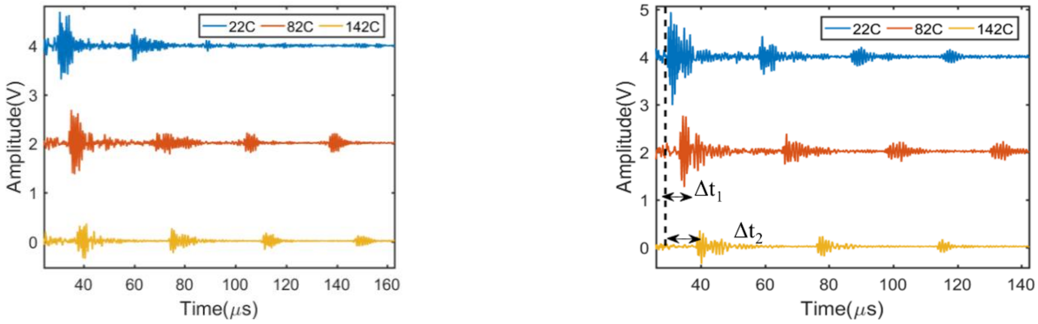

Figure 6.9 Immersion measurements for a) Heating cycle-1 *b) Heating cycle-2*

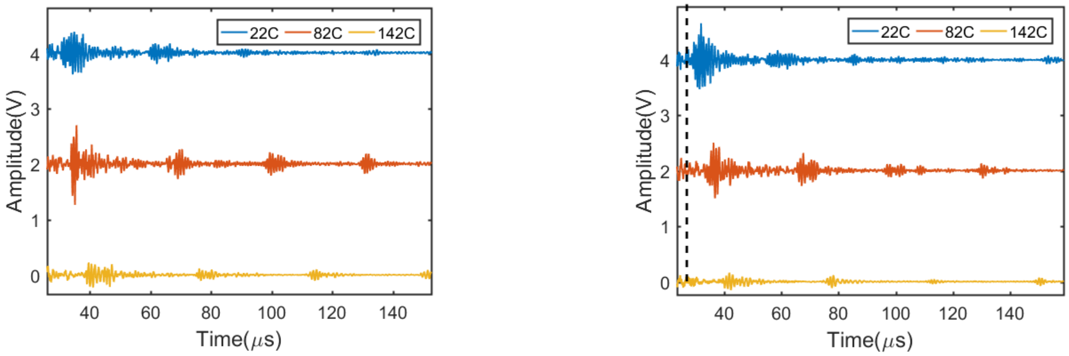

Figure 6. 10 Immersion measurements for a) Heating cycle-3 *b) Heating cycle-4*

Examples of RF data records for the 5th heating cycle are shown in Figure 6.11. The data shows clearly that the time of flight change from 22 C to 142C due to temperature dependent longitudinal velocity of silicon oil. The Oil and transducer were allowed to cool at natural cooling rate. As shown in Fig. 6.9(a-d), time of arrival of first front wall echo changes as a function of temperature. This can be given by $\Delta t = t_{22C} - t_T$ where t is the time of arrival of first front wall echo at temperature T. Fig. 6.12(a) shows Δt for each thermal cycle.

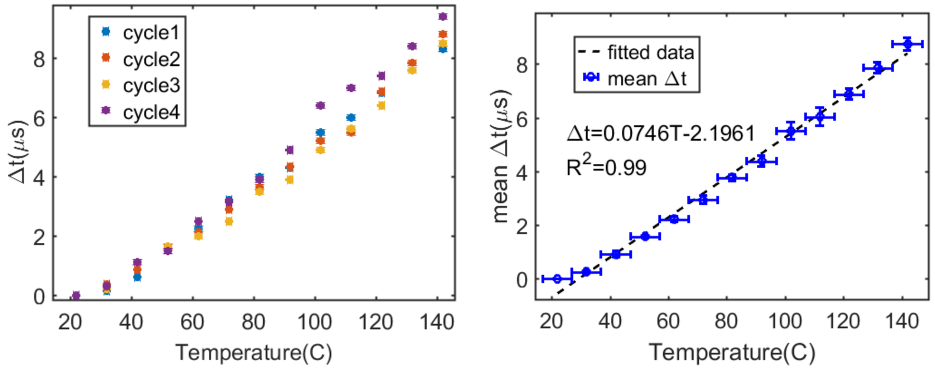

Figure 6. 11 Δt a) for four thermal cycles b) mean time Δt shows linear increase up to 142C

As seen from Fig. 6.11(b), the mean value of mean value Δt calculated using experimental data from cycle 1 through 4 shows linear increase up to 142C. This information can also be expressed as time of arrival of first front wall echo instead of Δt as shown in Fig. 6.12(a).

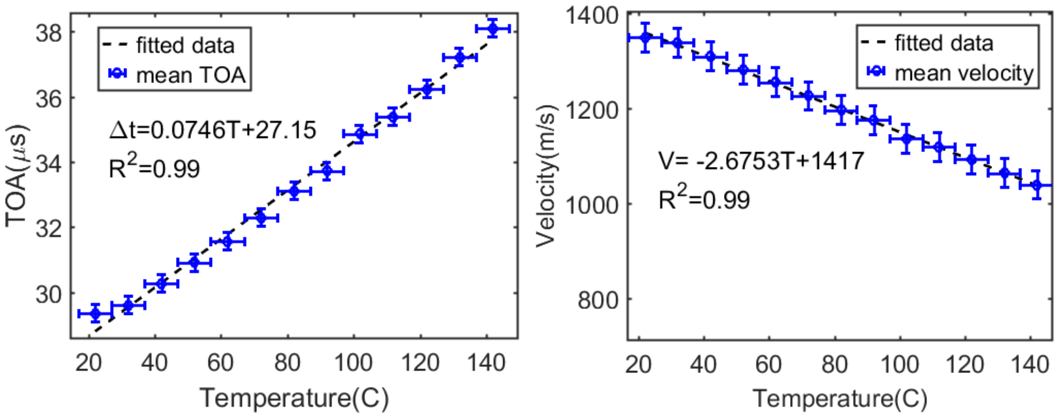

Figure 6.12 a) Mean time of arrival (TOA) of 1st Front wall echo b)average speed of sound in silicon oil as a function of temperature using the developed 2.25MHz ultrasonic transducer

Using the mean time of arrival (TOA) from Fig.6.12 (a), the average speed of silicon oil computed for total travel path of 40mm. The speed of sound in silicon oil reduces linearly from 22C to 142C. The magnitude of speed of sound is reduced by 23% as temperature is raised from 22C to 142C.In addition to the time of arrival, the peak amplitude of first front wall echo as a function of temperature are also studied as shown in Fig6.13(a) through (d). Increase in the mean amplitude from 22C to 52C in Fig. 6.14(a) is consistent with the results by Kibe et al.(2015). This can be attributed to improved wetting of silicon oil with faceplate of the transducer. Figure 6.14(b) shows sensitivity of transducer in silicone oil using equation (6.1) which indicates 8 dB reduction as a function of temperature up to 142C.

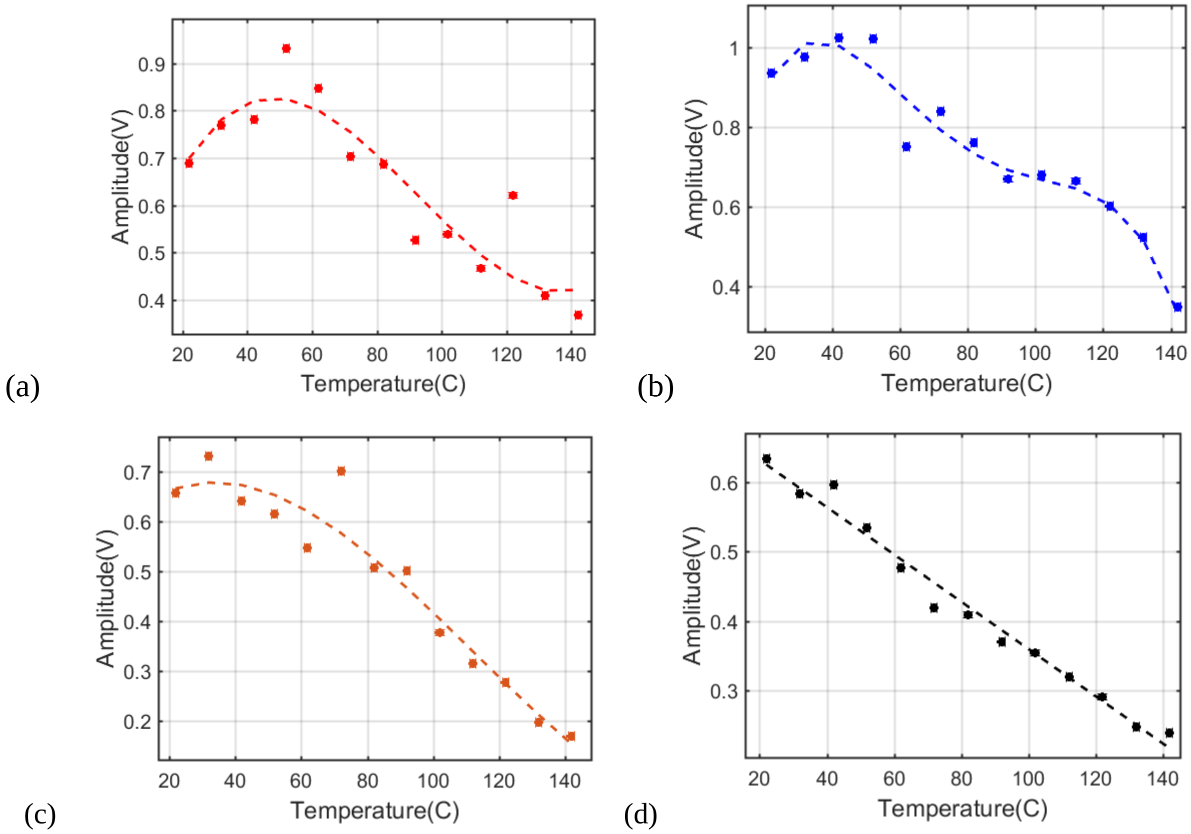

Figure 6.13 Front wall echo amplitude reduction as function of temperature of silicon oil for thermal (a) cycle-1 (b) cycle-2 (c) cycle-4 (d) cycle- 5. Dashed line indicates fitted experimental data

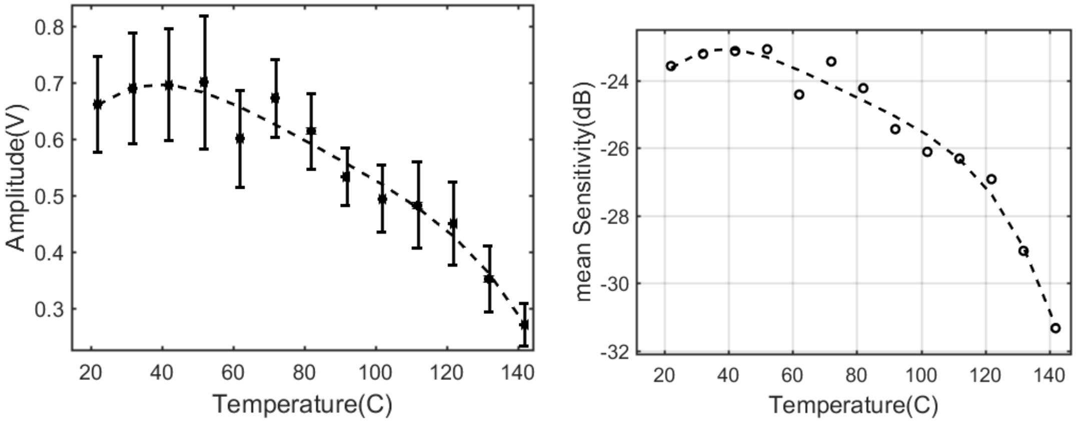

Figure 6.14 a) Mean first front wall echo amplitude b) mean sensitivity of transducer as a function of temperature for immersion measurements in silicone oil

In this work, a new 2.25MHz BSPT immersion transducer was developed and tested for immersion measurements in silicon oil up to 142C. The time of flight measurements showed 23% decrease in speed of sound in silicone oil as a function of temperature. The mean sensitivity of transducer reduced by 8dB from 22C to 142C. These conclusions will be verified again with a new set of BSPT transducers.

7. Model Assisted approach for Probability of Detection (PoD) at High Temperature

Previous studies have shown that signal to noise ratio (S:N) in ultrasonic measurements becomes a critical issue for ultrasonic transducers operating in liquid sodium at a hot stand-by temperature of 260 C [Griffin et al. (2009)]. Particularly, the reduction in the signal strength as a function of temperature reduces the ability to identify and distinguish between an ultrasonic response from the defect and the measured noise signals. In seeking a metric for performance, the efficacy of the NDT inspection is often quantified and displayed using a probability of detection (POD) curve. At high temperatures transducers are seen to have a reduction in signal strength which can cause a reduction in POD and such performance change needs to be assessed.

From a performance perspective, non-destructive inspections are required by codes and standards to be “reliable and repeatable,” and such performance required to be measured and needs to address human factors, equipment and related experimental limitations as well as the limits set by the underlying physics for the inspection modality, in the context of part geometry, material properties and defect population (including type, shape, size and orientation). [MIL-HDBK-1823A (2010)]

In assessing performance of an NDT inspection, the experiments are, in general, time consuming and expensive, due to the cost of fabricating appropriate sample sets which include representative populations of defects. A more cost-effective approach, which can also be used to supplement a more limited experimental program, and to increase confidence is using physics based modeling to predict POD, and this has been demonstrated in a series of studies performed over many years [e.g. Thompson et al., (2008), Meeker et al., (2012)].

The basic idea behind MAPOD is to use an understanding of the effects of physical factors on the measurement results and this has been investigated in various studies using different approaches. Examples of such studies include work by Sarkar et al. (1998) who proposed a modeling methodology to estimate POD as a function of known fixed effect parameters. Smith (2005) presented a transfer function approach that correlated the responses from an artificial defect to that of a real crack geometry. This was followed by further work where Smith et al. (2007) developed the Full Model-Assisted (FMAPOD) approach. These models have become an integral part of a unified approach for model assisted probability of detection (MAPOD) [Thompson et al.,(2008)].

Cobb et al. (2009) advocated development of hybrid finite element models to use in the MAPOD approach with crack geometry being the primary source of variability. The thesis of this work states that predictive modeling should be multi-domain including considering the sensor, electronics, and power management. The use of NDE Models has seen increased use. Jensen et al.(2010) explored uncertainty propagation through CIVA simulation models. Wirdelius et al. (2012) also developed POD based on synthetic data obtained from simSUNDT software. Pavlovi et al. (2012) reported POD data as a function of multiple parameters in contrast to the conventional signal response analysis.

The use of POD is being expanded from conventional NDE to looking at data for structural health monitoring. For example Aldrin et al. (2011) reported simulation-based POD studies for reliability assessment of structural health monitoring (SHM) systems within the framework of MAPOD.

.

Li et. al. (2014) developed a statistical model for estimating POD based on the physical mechanisms of ultrasonic inspection. This work successfully demonstrates the intersection of statistical and physical modeling of ultrasonic wave propagation for the purpose of estimating POD.

In a harsh operating environment, such as a nuclear reactor, POD can be expected to reduce over time due to deterioration of sensor performance. Subair et al., (2014) reported finite element modeling for the estimation of POD of nuclear components at room temperature. Roy et al. (2014) developed temperature dependent, physics based modeling using experimental data up to 80 C. The objective of this work was to propose a temperature compensation strategy for guided waves. Similarly, Wang et al. (2014) reported an adaptive filtering technique for temperature compensation of Lamb waves. Recently, Salmanpour et al. (2016) proposed a new method of temperature correction and used it in conjunction with a delay and sum damage detection algorithm. The proposed method is based on baseline signal stretch with an improved minimum residual allowing correction over a larger temperature range. Gianneo et al. (2016) reported the FMAPOD approach for inspection of a copper canister to plot the POD curve for flat bottom holes (FBH) where data were calculated using CIVA. In this work, the primary source of variability was structural attenuation. Recently Gianneo (2017) extended this work using finite element models for a multi-parameter POD formulation for a Lamb waves–based SHM for light alloy aeronautical plates. Yusa et al. (2016) evaluated general effects of flaw parameters on the ultrasonic response using the numerical simulations and experimental measurements on 316L steel specimens.

Performance quantification is seeing increased attention and recently, Janapati et al. (2016) discussed the role of POD in NDE and SHM. The focus of this work was quantifying the effect of transducer parameters on damage detection sensitivity. However, the effect of temperature dependency of piezoelectric material performance on the POD is not sufficiently quantified. In the current work, the temperature dependency of piezoelectric material is modelled with regards to its effect on the POD, specifically considering the case of performance of PZT-5A. The objective of this work is to connect a microscopic material phenomenon that occurs within piezoelectric ceramics at a high temperature to an industrial practice of evaluating POD for quantifying performance of NDT inspections. This was achieved by use of a physics based model using finite element (FE) software [COMSOL(2014)] and temperature dependent material coefficients for PZT-5A which were determined by Sabat et al., (2007). Using the results from the FE model, temperature correction and transfer factors are proposed to estimate POD value at high temperature, when only a POD that is determined from room temperature experimental data is available.

7.1.1 Problem description

The problem geometry considered is a planar compression wave transducer transmitting at normal incidence through a solid-solid interface as shown in Fig. 7.1. The elastic waves are scattered by the side drilled hole (SDH) in the solid and the response is received by the same transducer in a pulse-echo contact experiment. It is assumed that the plane of the transducer is perpendicular to the axis of the SDH.

The assumptions for the physics based model are: a) plain strain condition, b) the material behavior is linearly elastic, c) small deformation of the plate, d) material is continuous and homogenous, d) damping variation due to temperature is negligible, d) the thermoelectric coupling resulting in a pyroelectric effect is not considered, and e) electric field of the piezoelectric material is irrotational (quasi-electrostatic field which implies absence of magnetization). Thus, the frequency dependence of the piezoelectric material is caused only by the mechanical displacement.

Let Ω be the domain of the problem connected by the Lipschitz boundaries $\partial\Omega$. The low carbon steel block with 50mm x 50 mm cross section and the piezoelectric transducer are represented by domain Ω_{steel} and $\Omega_{\text{transducer}}$ respectively. The piezoelectric material is PZT-5A and the domain has a length of 6.0 mm and a thickness of 1.0 mm. Hence, the computational domain is given by $\Omega = \Omega_{\text{Steel}} \cup \Omega_{\text{transducer}}$. In this approach, the amplitude of the signal reflected from SDH's is computed in terms of the vertical component of the displacement field in the finite element model.

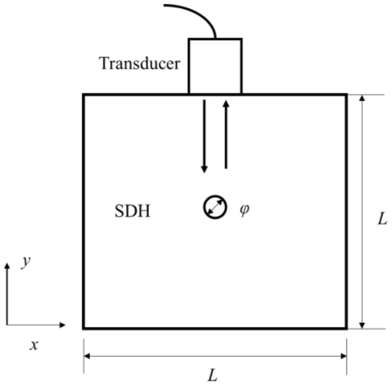

Figure 7.1 Problem configuration to predict the response from SDHs at normal incidence

7.1.2 Constitutive equations of piezoelectric material for temperature dependence:

The equations for piezoelectricity can be obtained using Gibbs thermodynamic potential which is given as [Baptista et al. (2014)]

$$S_i = s_{ij}^{E,H,\theta} T_j + d_{mi}^{H,\theta} E_m + d_{mi}^{H,\theta} H_m + \alpha_i^{E,H} d\theta \tag{7.1}$$

$$D_m = d_{mi}^{H,\theta} T_i + \varepsilon_{mk}^{T,H,\theta} E_k + m_{mk}^{T,\theta} H_k + p_m^{T,H} d\theta \tag{7.2}$$

Where S_i is the Cauchy's total mechanical strain tensor, D is the electric displacement tensor, $\varepsilon_{mk}{}^{T}$ is the absolute permittivity at constant mechanical stress T_i , $s_{ij}{}^{E,H,\theta}$ is the elastic compliance coefficient at a constant electric field E, constant magnetic field H and constant temperature θ and d_{mi} is the piezoelectric charge coefficient. The thermal expansion coefficient and pyroelectric constant are given by α and p respectively. The magneto-dielectric coefficient is given by m. Phase velocity of elastic waves for piezoelectric ceramic is significantly less than the electromagnetic waves. This implies time derivative of magnetic field $H \approx 0$ indicating absence of magnetization effect and presence of a quasi-static field. Thus magneto-dielectric coupling from (7.1-7.2) can be ignored. In the current work, the temperature difference $d\theta$ is assumed to be small representing a gradual increase in the temperature of a piezoelectric based sensor. Thus, for a quasi-thermal change in the piezoelectric material, the thermal expansion and pyroelectric effect can be ignored. This reduces (7.1-7.2) to a strain charge form of linear theory of the piezoelectric effect can be given by

$$S_i = s_{ij}{}^{E} T_j + d_{mi} E_m \tag{7.3}$$

$$D_m = d_{mi} T_i + \varepsilon_{mk}{}^{T} E_k \tag{7.4}$$

The piezoelectric material modeled in this study, PZT 5A, exhibits a crystal structure with a symmetry of a hexagonal 6mm class [Sabat et.al (2007)]. The piezoelectric material is considered transversely isotropic if the poling axis aligns with one of the material symmetry axes [Sabat et al. (2007)].

For a 2-D physics based model, the material matrix reduces to 4 elastic coefficients, 3 piezoelectric coefficients and 2 dielectric coefficients. Hence the piezoelectric stiffness matrix can be given as

$$S = \begin{bmatrix} s_{11} & s_{13} & 0 & 0 & d_{31} \\ s_{13} & s_{33} & 0 & 0 & d_{33} \\ 0 & 0 & s_{44} & d_{15} & 0 \\ 0 & 0 & d_{15} & \varepsilon_{11} & 0 \\ d_{31} & d_{33} & 0 & 0 & \varepsilon_{33} \end{bmatrix} \tag{7.5}$$

Further information regarding the temperature dependence of a piezoelectric material is given by [Sabat et al. (2007)]. In the current FE model, the in-plane deformation problem is considered in the x-y plane as shown in Fig.1. Poling axis of the soft PZT-5A coincides with the y-axis of the model. Assumed electromechanical load for the in-plane problem is given by: a) $E_1 \neq 0, E_3 \neq 0, E_2 = 0,$ also implies $D_1 \neq 0, D_3 \neq 0, D_2 = 0$ b) mechanical displacement $u_1 \neq 0, u_3 \neq 0, u_2 = 0$. Thus, the non-zero stress and strain components are given by $\sigma_{11}, \sigma_{33}, \sigma_{13}$ and s_{11}, s_{13}, s_{33}. The assumption (b) of non-zero mechanical displacement, strain, and stress also applies to linear elastic solids in the physics based model.

7.1.3 Constitutive equation for the wave propagation in a linear elastic material

The equation of linear momentum balance in the time domain is given by (Rose,1994)

$$\rho \frac{\partial^2 u}{\partial t^2} = \nabla . s + F_v \tag{7.6}$$

where ρ is the assigned material density, u is the displacement, s is second order Piola-Kirchoff stress tensor, and F_v is the body force. The top boundary (set at y = 30) for the Ω_{steel} shown in Fig. 7.1 is kept traction free ($\sigma_{31}= \sigma_{33}= \sigma_{11}=0$). A low reflection boundary condition is applied to the Ω_{steel} at x=0 and x=L boundaries to reduce reflection of the waves from side walls which also reduces the degree of freedom for which the model is solved, and this is given as [COMSOL (2014)]:

$$\sigma \cdot n = -pC_p\left(\frac{\partial u}{\partial t} \cdot n\right) - pC_s\left(\frac{\partial u}{\partial t} \cdot t\right)t \tag{7.7}$$

The vertices x=0 and x=L on the bottom boundary (y=0) of the Ω_{steel} are modelled as fixed constraints (u=0) representing the fixed support used to ensure flatness of the structure during ultrasonic contact measurements.

7.1.4 Piezoelectric Material-Electrostatics

As previously stated, for the piezoelectric media, the electric field (piezoelectric media) is assumed to be irrotational. Thus, the electric field E is related to the scalar electric potential V given by equation (4.6) . The terminal boundary is assigned to the top electrode of the piezoelectric material which is coupled to the external electrical circuit discussed in the next section. The bottom boundary of the Ω_{PZT} is grounded (V=0). Zero charge constraint is assigned in the domain Ω_{PZT} at boundaries without terminal or ground boundaries given by equation (4.7). Charge density ρ_v in the domain Ω_{PZT} is given by equation (4.8)

7.1.5 External circuit for the instrumentation electrical impedance

In the experimental measurements, the piezoelectric transducer is connected to the pulsar-receiver circuit using BNC cables and lead wires. This introduces an electrical impedance mismatch between the piezoelectric transducer and the pulse-receiver instrumentation. This is modelled in a finite element model by introducing a resistor with impedance equal to that of pulsar-receiver. In the current study, the impedance value of resistor is set to an ideal 50 Ω.

The electric circuit module in COMSOL is used to evaluates global variables, voltage, and current as a function of time. In the model, a Hamming windowed sinusoid signal of 160V is applied to the piezoelectric material. The current at the back electrode of the piezoelectric element $\partial^D \Omega_{PZT}$ is given by [COMSOL (2014)]:

$$\int_{\partial^D \Omega_{PZT}} D \cdot n = Q_0, \frac{dQ_0}{dt} = I_{cir} \tag{7.8}$$

Hence, the voltage on the electrode surface $\partial^D \Omega_{piezo}$ is given by:

$$V_{pz}(t) = V_{source}(t) - I_{cir} R \tag{7.9}$$

7.1.6 Discretization

A triangular element of maximum size 0.05mm was used for meshing the complete domain $\Omega = \Omega_{SS} \cup \Omega_{Transducer}$. The total number of elements is 256662 with an average growth rate of 1 and an average element quality equal to 0.99. The region inside the SDH is not meshed and boundaries are kept traction free. This simulates the defect as a geometric discontinuity. The maximum element size is determined by the minimum shear wave speed of the material assigned to the computational domain given by [Bilgunde and Bond (2015a)]:

$$h_{\max} = \frac{c}{f_0 N}, \; t = \frac{CFL}{f_0 N} \tag{7.10}$$

where h_{max} is the maximum element size, c is the shear wave speed in the material, f_0 is the highest frequency in the desired spectrum, N is the number of element per wavelength, t is the time step, and CFL number [Courant et al. (1928)] is set equal to 0.2 [Bilgunde et al. (2015)]

7.1.7 Probability of detection (POD) formulation

In determining the POD the reflected signal displacement data from the physics based model corresponds to response $\hat{a}$. The true size (here, diameter) of the flaw a is related to response $\hat{a}$ by MILHDBK-1823 A (2010)

$$\hat{a} = \beta_0 + \beta_1 a \tag{7.11}$$

Which is of the form

$$\hat{y} = \beta_0 + \beta_1 x \tag{7.12}$$

Equation (7.12) is also of the form Ax=b. Using the theory of least square solutions from linear algebra, the estimate for β_j is given by as:

$$\begin{bmatrix} \hat{\beta}_0 \\ \hat{\beta}_1 \end{bmatrix} = \left(A^T A\right)^{-1} A^T b \tag{7.13}$$

If system noise, n, is added to the terms in equation (7.12), the modified equation is then given as:

$$\hat{y}_1 = \beta_0 + \beta_1 x + n \tag{7.14}$$

Where system noise n has a normal distribution N(0, τ^2). Using Bessel's correction, τ^2 is given by:

$$\tau^2 = \frac{1}{n-1}\sum\left(\hat{y}^2 - \hat{y}_1{}^2\right) \tag{7.15}$$

Using the Wald method, which is given in Appendix G of the standard handbook, MILHDBK-1823 A (2010) is described by the relationship:

$$\mathrm{var}(\hat{y}) = \mathrm{var}(\hat{\beta}_0) + x^2 * \mathrm{var}(\hat{\beta}_1) + 2x * COV(\hat{\beta}_0, \hat{\beta}_1) \tag{7.16}$$

$$\mathrm{var}(\hat{y}_1) = \mathrm{var}(\hat{y}) + \tau^2 \tag{7.17}$$

The decision threshold for y_{th} is set-up is set to exhibit a conventional nature observed in measurements based POD curves. The detection threshold is expressed as the amplitude of vertical displacement field from the model data. The upper and lower 95% confidence bounds are plotted using the Probit function. The POD curve is computed by the relationship given as,

$$POD = \Theta\left(\frac{\hat{\beta}_0 + \hat{\beta}_1 x - y_{th}}{\sqrt{\mathrm{var}(\hat{y}) + \tau^2}}\right) \tag{7.18}$$

where Θ is the cumulative distribution function. It should be noted that $\hat{y}$ is the displacement amplitude response from the SDHs computed using the physics based model described previously.

7.1.8 Model validation and Experimental verification

For the experimental verification, SDHs are machined into a 1018 low carbon steel test blocks at a depth of 25mm as shown in Fig.2. V306 Panametrics 2.25 MHz planar piezoelectric transducer with 12.5 mm nominal element diameter is used for normal incidence contact measurements. For the near field length (N) of 15.6mm, 6dB beam width in the steel at the measured depth of SDHs (1.6N) is 5mm. As the defect size approaches the transducer beam width, the response is not only a function of size of defect, but also a function of reflection ratio and beam width [Sarkar et al. (1998)]. Hence, the largest flaw size is limited to 3.9mm to reduce the beam width limitation effects. The minimum distance between two adjacent SDHs (22mm) is also greater than the 6dB beam width at a given depth (1.6N) of SDHs.

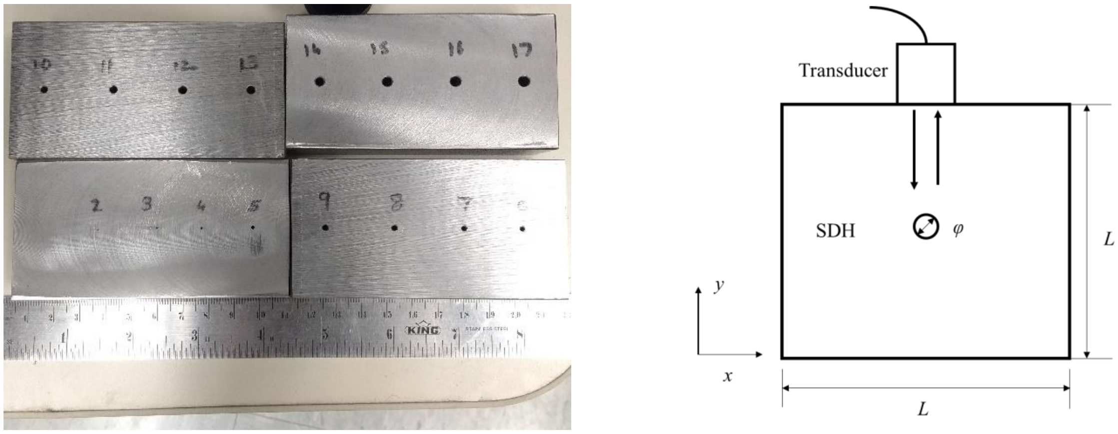

Figure 7.2 Side drilled holes with diameter varying from 0.46mm to 3.9 mm in a 1018 low carbon steel block

The Panametrics 5052 pulsar receiver with energy setting at 2, repetition rate at 4, 40 dB gain and damping set at 5 is used with a 1m coax cable and BNC connectors. The experimental data acquired using LeCroy HDO 4034 oscilloscope with sampling frequency of 450MHz is averaged 512 times to minimize random electrical noise in the A-scan. Contact measurement for each SDH is repeated 6 times for all 16 SDHs to minimize the variability due to contact pressure. Mean of the six measurements for each SDH response $(\bar{x})$ is computed to compare with simulation data.

The experimental error for each SDH response is given by $e = \sigma / \sqrt{N}$ where σ is the standard deviation and N is the number of measurements for each SDH. Mean value of experimental error $(\bar{e})$ is assigned to the data as shown in Fig. 7.3(a).

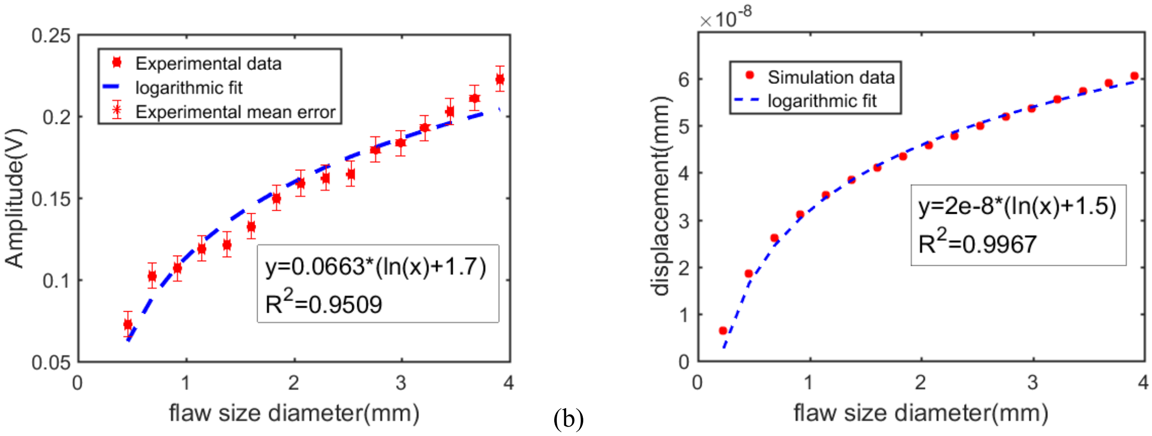

(a) (b)

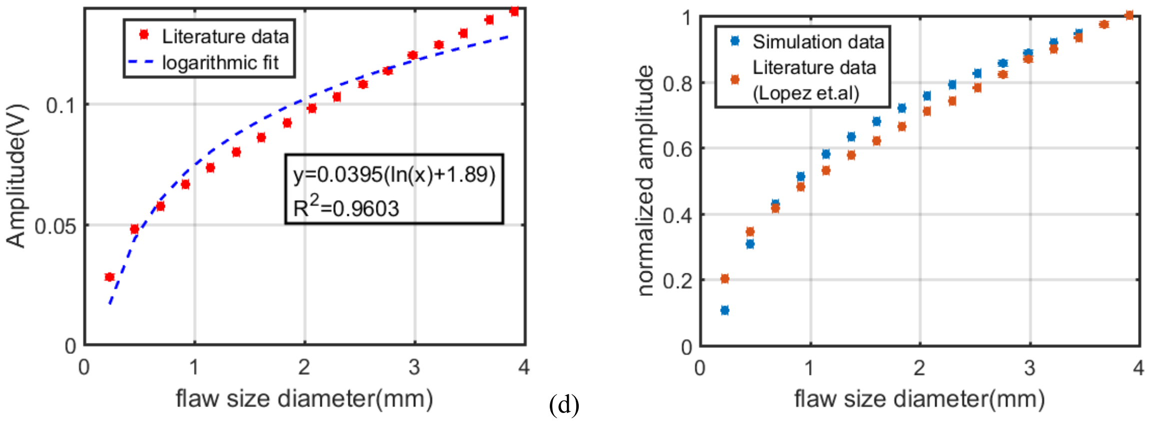

(c) (d)

Figure 7.3 P-wave Scattering amplitude for a) Experimental data b) Simulation data c) Literature model data [Lpoez et al.(2005)] d) Comparison of normalized FE simulation and literature model data

Fig.7.3(b) shows FE model based P-wave scattering amplitude as a function of SDH diameter. Fig. 7.3(c) shows scattering amplitude model data for SDH reported by Lopez et al. (2005). The increase in the normalized scattering amplitude as a function of flaw size is in good agreement with literature data as shown in Fig.7.3(d). For Fig.7.3(a) through Fig.7.3(c) scattering amplitude can be fitted logarithmically in the form given by $y = m[\ln(x) + c]$. The experimental data shown in Fig.7.3(a) acquired in terms of voltage amplitude is dependent upon the excitation pulse using the pulsar receiver circuit. The scattering amplitude from the FE simulation is dependent on the amplitude of the input mechanical displacement to the model. As shown in Table I, this is expressed as the multiplier factor m_i in the fitted equations

Table 7.1 Logarithmic Fitting of the data

Data	Equation	m_i	R^2
Experimental data	$y=0.0663(\ln(x)+1.7)$	0.0663	0.95
FE model data	$y=2e\text{-}8(\ln(x)+1.5)$	2e-8	0.99
Literature model data	$y=0.0395(\ln(x)+1.89)$	0.0395	0.96

This effect needs to be compensated to compare to model and experimental data. The scattering amplitudes from experiment and models, corrected for the multiplier effect are thus given by

$$y'_{sim} = \frac{y_{sim}}{m_1} = \frac{y_{sim}}{2e-8} \approx \ln(x) + 1.5 \tag{7.19}$$

$$y'_{\exp} = \frac{y_{\exp}}{m_2} = \frac{y_{\exp}}{0.0663} \approx \ln(x) + 1.7 \tag{7.20}$$

$$y'_{lit} = \frac{y_{lit}}{m_3} = \frac{y_{lit}}{0.0395} \approx \ln(x) + 1.89 \tag{7.21}$$

Fig.7.4(a-b) shows a good agreement between model and experimental data for 0.4< d/λ<1 using the corrected scattering amplitudes of the SDHs from equation (7.19) through (7.21).

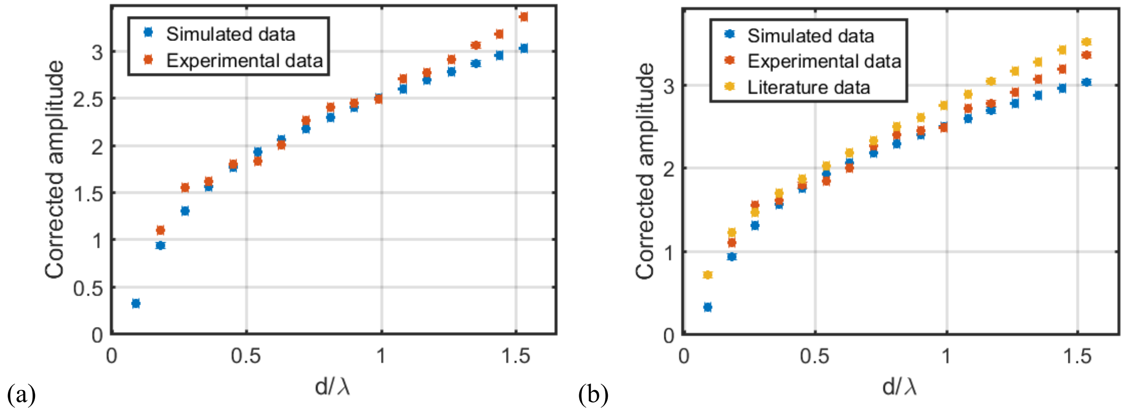

Figure 7.4 (a-b) Comparison of corrected P-wave scattering amplitudes from simulation data, experimental data and previous published model data [Lopez et al.(2005)] for SDH

For the d/λ greater than 1, the experimental scattering amplitude shows divergence from the FE model data. The transfer factors m_1 and m_2 from equation (7.19) and (7.21) will be used to transform temperature effect from physics based model to the experimental POD.

7.1.9 Model data for scattering amplitude variation due to temperature dependency of transducer material (PZT-5A)

In this model case, the transducer elements are modeled and temperature dependency is assigned to the piezoelectric material matrix, S, shown in equation (7.5) The material coefficients for PZT-5A corresponding to a particular temperature are based upon the temperature dependent material coefficients given in the literature [Sabat et al. (2007)]. The calculated change in the flaw response as a function of the temperature dependent response of the transducer is shown in Figure 7.5.

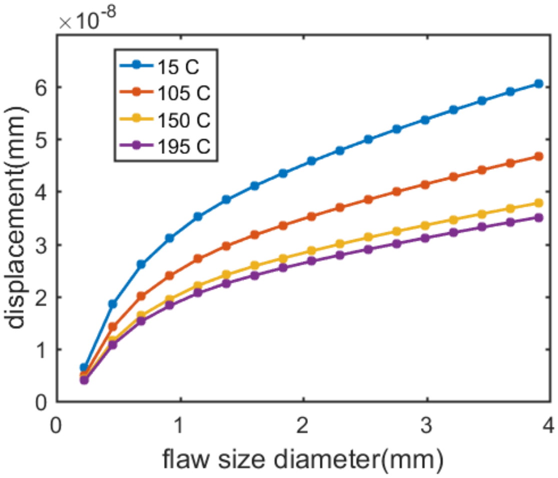

Figure 7.5 Displacement versus flaw size (diameter) when using temperature dependent experimental data values for the piezoelectric material coefficients for PZT-5A at a series of temperatures

According to the experimental data [Sabat et al. (2007)], the magnitudes of $s_{11}, s_{13}, s_{33}, s_{44}$ coefficients reduce whereas d_{33}, d_{31}, $\varepsilon_{33}, \varepsilon_{11}$ increase as a function of temperature from 15C to

195C due to the extrinsic and intrinsic contributions in the piezoelectric ceramic[Sabat et al. (2007)]. Magnitude change in each of the material coefficients as a function of temperarture contributes to the change in total mechanical strain S_i and dielectric displacement D_m as described by equation (7.3) through (7.5). This influence of temperaure on piezoelectric effect is related to the P-wave scattering amplitude reduction through equation (7.6) and (4.8). The logarithmic fitting of the simulated data in the form of equation (7.12) is shown in Table 7.2 where a is the simulated reflected echo amplitude from SDH and a is the true size of the SDH

Table 7.2 Logarithmic fitting of the simulated data

Temperature	**Equation**	**β_1**	**β_0**
15 C	$\hat{a} = 1e-8(2*\ln(a)+3)$	2e-8	3e-8
105 C	$\hat{a} = 1e-8(1*\ln(a)+3)$	1e-8	3e-8
150 C	$\hat{a} = 1e-8(1*\ln(a)+2)$	1e-8	2e-8
195 C	$\hat{a} = 1e-8(1*\ln(a)+2)$	1e-8	2e-8

As the temperature increases from 15 to 105 C, the regression parameter β_1 reduces by 50% and β_0 remains unchanged. Increasing temperature of the PZT-5A from 105C to 150C reduces the value of β_0 by 66% while the value of β_1 remains unchanged. It should be noted that from 150 to 195 C there is no change in the equation used for logarithmically fitting the data.

7.1.10 Probability of detection (POD) curve with temperature dependence of the transducer active element

Using equations (7.11) through (7.18), POD values are calculated and the resulting data is plotted from the physics based model data for different temperatures. The detection threshold is expressed as the amplitude of vertical component of the mechanical displacement field u from the model data.

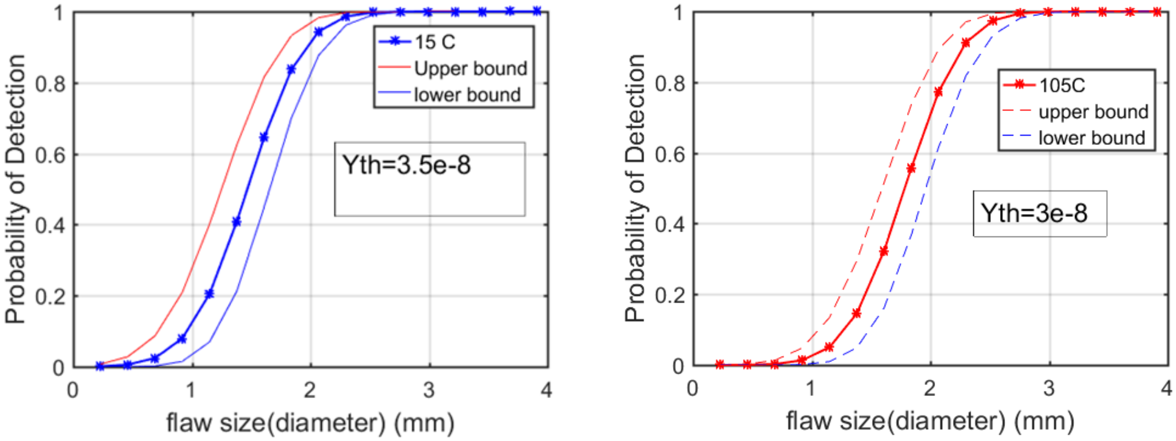

Figure 7.6 Probability of detection for SDH: a) 15 C b) 105 C for the predefined detection threshold Y_{th}

Fig7.6 (a) through Fig.7.7(b) show POD values for 15C, 105C,150C, and 195C. It should be noted that as the temperature is increased, the detection threshold needed to be lowered.

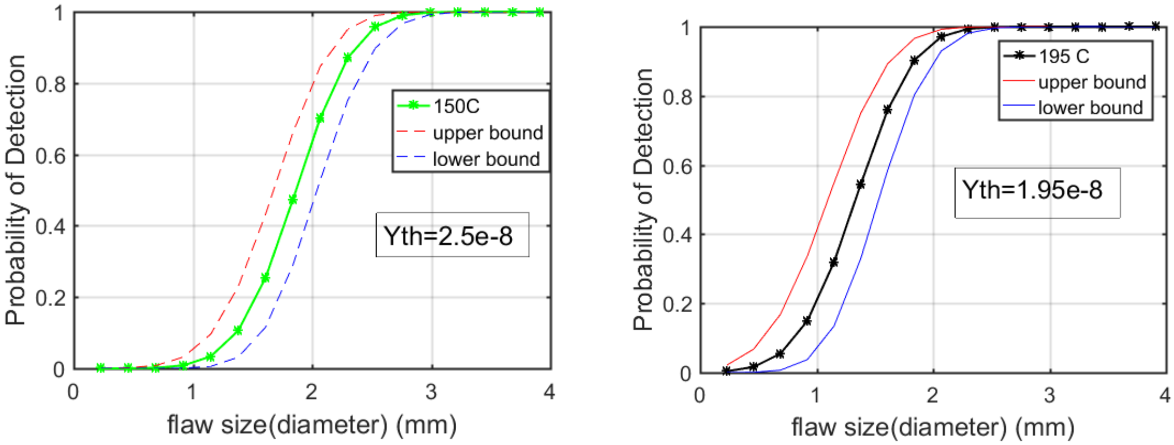

Figure 7. 7 Probability of detection at: a) 150 C *b) 195 C for the predefined detection threshold Yth*

However, the detection threshold is generally a system limitation which should be unmodified for all the temperatures at which data are measured. Hence, Y_{th} is selected as 3.5e-8 mm which corresponds to the threshold at 15 C.

The model based POD due to temperature dependence of PZT-5A for the case of SDH in low carbon steel and a fixed threshold is given in Fig.7.8. For the given decision threshold, the flaw size with POD =1 at 15C reduces significantly at 195C as shown in Fig. 7.8. Hence, the current study can help determine the flaw sizes which see a reduction in probability of detection due to the temperature dependent response of the piezoelectric element in a transducer. It can be seen from Fig. 7.8 that, an increase in the temperature of the transducer introduces a considerable source of change in the POD for a given flaw size. Here, the model based POD reduces significantly for SDHs with a diameter between wavelength 0.5λ (1.4mm) and 1.17λ (3mm) in low carbon steel, at a resonance frequency of 2.25MHz.

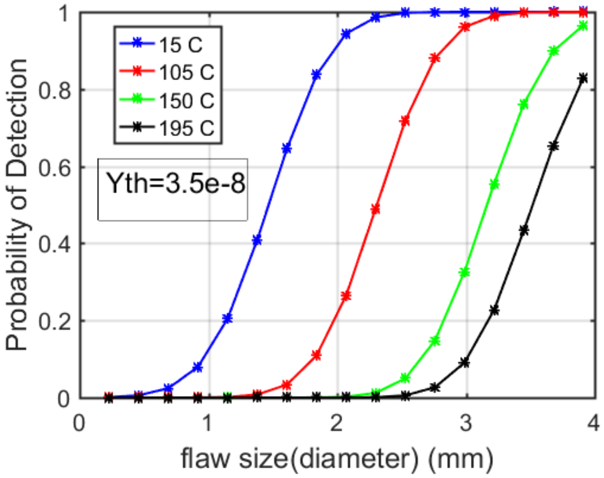

Figure 7.8 Effect of temperature dependence of capability of a piezoelectric transducer fabricated with PZT -5A and the POD curve for SDH in steel.

The effect of the temperature dependency for PZT-5A piezoelectric material properties at 2.25 MHz on the POD values are shown in Table 7.3. For artificial defects such as SDH's in steel with a diameter corresponding to size 1.1λ, a 97% reduction in the POD value between 15 and 195 C can be seen due to the temperature effect on the piezoelectric material.

Table 7.3 Model based data for POD as a function of transducer temperature and flaw size

SDH (d) (mm)	**d/λ**	**POD (Y_{th}=3.5e-8)**			
		15 C	**105 C**	**150 C**	**195 C**
0.23	0.09	0.001	0	0	0
0.46	0.18	0.005	0	0	0
0.69	0.27	0.024	0	0	0
0.92	0.36	0.08	0.0001	0	0
1.15	0.45	0.21	0.001	0	0
1.38	0.54	0.41	0.008	0	0
1.61	0.63	0.64	0.033	0	0
1.84	0.72	0.84	0.11	0	0
2.07	0.81	0.94	0.26	0.002	0
2.3	0.9	0.99	0.49	0.012	0
2.53	0.99	1	0.72	0.05	0.006
2.76	1.08	1	0.88	0.15	0.03
2.99	1.17	1	0.96	0.33	0.091
3.22	1.26	1	0.99	0.55	0.23
3.45	1.35	1	1	0.76	0.43
3.68	1.44	1	1	0.9	0.65
3.91	1.53	1	1	0.96	0.83

7.1.11 Temperature correction Factor K

The FE model presented in Section 7.1.7 was used to give results for the temperature dependent scattering amplitudes of SDH in a 1018 low carbon steel and a correction factor *K* for the temperature effect of the piezoelectric material is proposed. The effect of the temperature dependent coefficients on the scattering amplitude of SDHs in in a 1018 low carbon steel is quantified by the use of a finite element model and the resulting simulated data are shown in Figs 7.5 and 7.8. In sections 7.2.1 through 7.2.3, the material coefficients for PZT-5A are altered based on the temperature dependent experimental data (Sabat et al.,2007) at corresponding temperatures. According to the experimental data [Sabat et al. (2007)], the magnitudes of s_{11},s_{13},s_{33},s_{44} coefficients reduce whereas d_{33}, d_{31}, ε_{33},ε_{11} increase as a function of temperature from 15C to 195C due to the extrinsic and intrinsic contributions in the piezoelectric ceramic [Sabat et al. (2007)]. The correction factor is calculated by dividing the scattering amplitudes at 15C by the scattering amplitude at corresponding higher temperatures. The numerical uncertainty in the correction factor is estimated as *K* ± 0.02 with maximum deviation at SDH of 0.23mm diameter. From the data given Fig. 7.9(b), the value of K at corresponding temperatures is the magnitude by which scattering amplitude needs to be compensated to match POD at 15C

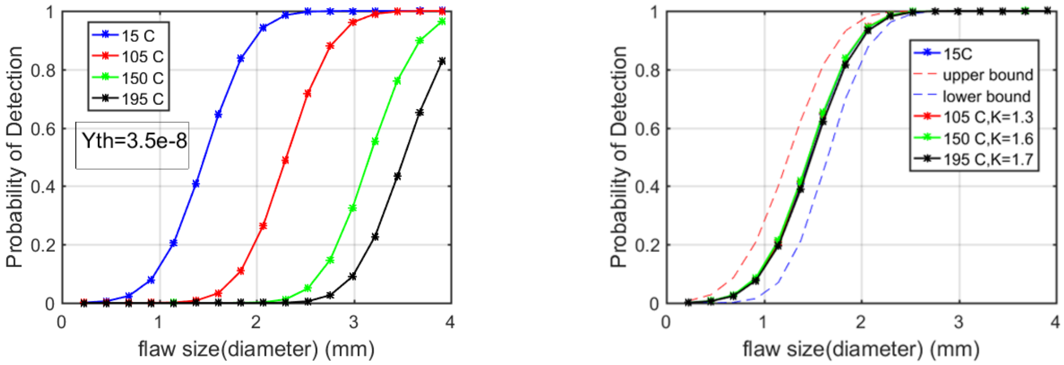

Figure 7.9 Model based POD for SDH in steel a) Without correction factor b) With PZT-5A temperature correction factor K. (dashed line (red, blue) indicate 95% confidence bounds for POD curve at 15 C

In order to develop and apply a temperature correction determined using the results from the physics based model, to the experimental data, the detection threshold voltage for the experimental derived POD is formulated as

$$V_{th} = \frac{Y_{th}}{m_1} * m_2 = 0.1160 \approx 0.12V \tag{7.22}$$

where Y_{th} =3.5e-8 (mm) is detection threshold for the model data and the transfer factors m_1, m_2 were obtained from equations (7.19) and (7.20). One example of the POD for experimental data for scattering by a series of SDH at a depth of 25mm in a low carbon steel block measured with a 2.25 MHz pulse-echo compression wave transducer at room temperature are given as one curve(blue dashed line) in Fig 7.10. Using the temperature specific factor *K*, a reduction in the scattering amplitudes of the room temperature experimental data is calculated for the cases of 105, 150 and 195C. Using this methodology the estimation of high the temperature (HT) POD, for the same frequency transducer (2.25 MHz) on a low carbon steel block using room temperature experimental data, with correction factor K and transfer factors m_1,and m_2., is shown in Fig 7.10.

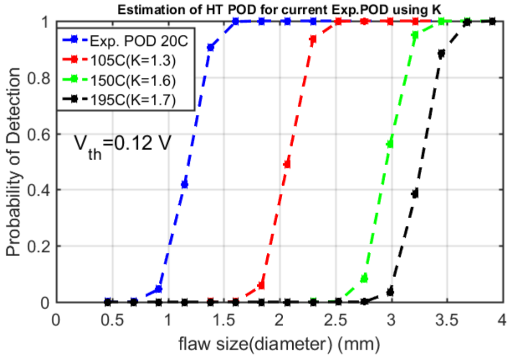

Figure 7.10 Estimation of the High temperature (HT) POD obtained using room temperature results obtained with a 2.25 MHz transducer on a low carbon steel block containing SDH (dashed blue line) together with temperature correction factor for PZT-5A material data, obtained from the physics based model

As shown in Fig. 7.10, 97% reduction in the POD of room temperature experimental data is estimated at 195C for SDHs of diameter from 1.5 mm to 2.8 mm using this MAPOD approach.

8. Conclusion

New insights into the causes of limited S:N performance in a research transducer developed at PNNL were obtained. The importance of boundary (interface layers) and interfaces on transducers were highlighted and some of the causes of non-ideal performance quantified. It was found that d_{33} is an inadequate metric for use in predicting tranbsducer performance and making material selection. The full matrix of material properties is needed. The new material BS-PT offers enhanced performance and this material should be considered in an air-backed transducer design. A methodology was developed and is reported for prediction of temperature effects on reduction of POD at elevated temperature.

Temperature dependence of piezoelectric material and bonding agent is one of the critical variables which needs to be analyzed for development and troubleshooting of high temperature ultrasonic transducers. A physics based modeling and design of experiments approach was demonstrated to analyze the interaction of transducer elements that reduce signal strength at an elevated temperature.

The transduction ability of the active element in an ultrasonic transducer is due to the piezoelectric effect and is usually considered in terms of the d_{33} coefficient. Transducer materials have multiple constants which contribute to estimating transducer performance. A finite element model was developed to study effect of temperature dependent material coefficients on the ultrasonic signal. Moreover, it was demonstrated that, the acoustic impedance mismatch between piezoelectric material and the faceplate due to the bonding agent results in a bimodal frequency response which distorts the time domain signal that is used ultrasonic imaging.

The piezoelectric material BS-PT (xBiScO3-(1-x)PbTiO3) is proposed for use and it has a Curie temperature in excess of 400C. In-situ pulse-echo contact measurements were performed up to 260C which is the hot stand by temperature for liquid metal cooled reactors, to study the performance of the acoustic coupling agent and the BS-PT piezoelectric material bonded to a low-carbon steel specimen. Experimental measurements indicated a 6dB reduction in amplitude of the first back-wall echo for contact measurement from 20 to 260C. At 2.25 MHz, in reviewing the data, a 0.1 MHz reduction in peak frequency is seen for the spectral content of the first back-wall echo. An ultrasonic C-scan of the interface did not indicate any significant dis-bonding.

A BS-PT based 2.25 MHz air-backed, single element immersion prototype transducer was developed. The temperature dependence of the proposed ultrasonic NDT system was evaluated in water up to 92C for three thermal cycles and in silicone oil up to 142C for five thermal cycles. Time of flight was observed to be linearly dependent with the increase in temperature of the oil for each cycle. The experimental mean value for speed of sound in silicon oil reduced by 23% when temperature was increased from 22C to 142C. Sensitivity of the transducer was also computed for each thermal cycle. The newly developed transducer was tested for robustness through 8 thermal cycles resulting into total 27 hours of operation to a maximum temperature of 142C.

In a final activity a novel model assisted POD approach (MAPOD) was demonstrated to estimate POD at high temperature using the room temperature experimental data. The source of variability for the MAPOD approach was the uncertainty in the piezoelectric effect with the increasing temperature. The methodology estimated a significant increase in the 95% POD for defect size in moving from room temperature to 195C when using 2.25 MHz ultrasonic transducers.

For the future work, the effect of gamma and neutron flux on BS-PT (xBiScO3-(1-x)PbTiO3) needs to be studied before it can be further considered as a transducer material for in-reactor deployment.

References

Abboud, N. N., Wojcik, G.L., Vaughan, D.K., Mould, J. Powell,D.J. and Nikodym, L. "Finite element modeling for ultrasonic transducers." In *Medical Imaging'98*, 19-42. International Society for Optics and Photonics, (1998).

Aldrin, J. C., Medina, E. A., Lindgren, E. A., Buynak, C. F., and Knopp, J. S. Protocol for reliability assessment of structural health monitoring systems incorporating model-assisted probability of detection (MAPOD) approach. Air Force Research Lab Wright-Patterson AFB OH, Materials and Manufacturing Directorate (2011). ADA585081.

Amini, M. H., Sinclair, A. N., and Coyle, T. W. "A New High-Temperature Ultrasonic Transducer for Continuous Inspection". *IEEE Transactions on Ultrasonics, Ferroelectrics, and Frequency Control*, ***63***(3), 448-455. (2016).

Augereau, F. P., Ferrandis, J. Y., Villard, J. F., Fourmentel, D., Dierckx, M., and Wagemans, J., "Effect of intense neutron dose radiation on piezoceramics", *Journal of the Acoustical Society of America*, ***123***(5), 3928 (2008).

Baptista, F. G., Budoya, D. E., de Almeida, V. A., and Ulson, J. A. C. "An experimental study on the effect of temperature on piezoelectric sensors for impedance-based structural health monitoring" *Sensors*, ***14***(1), 1208-1227 (2014).

Bar-Cohen, Y., Bao, X., Badescu, M., Sherrit, S., Lee, H.J., Zacny, K., Kumar, N. and Mumm, E., Drilling and Sample Transfer Mechanisms for Potential Missions to Venus. In Inner Solar System ,163-187, Springer International Publishing. (2015)

Bilgunde, P. N. and Bond, L. J., "Analysis of High Temperature Ultrasonic Transducer Performance in Small Modular Reactors," In *Proc., NPIC & HMIT 2015 Conference, February 23–26, 2015, Charlotte, North Carolina*, American Nuclear Society,742-751 (2015a).

Bilgunde, P. N., and Bond, L. J. "A 2D finite element simulation of liquid coupled ultrasonic NDT system." In *Review of Progress in QNDE: Volume 34* ,Vol. 1650, 1543–1552, AIP Publishing. doi:10.1063/1.4914773 (2015b).

Bilgunde, P. and Bond, L. J., "Effect of Thermal Degradation on High Temperature Ultrasonic Transducer Performance in Small Modular Reactors", *Physics Procedia*, Volume 70, 2015, 433-436 (2015)

Bilgunde, P. and Bond, L. J., "Progress towards development of high temperature using single element transducer", (Fall ANS Meeting) In *Trans. Am. Nuclear Soc.*, Vol. 115,352-355 (2016)

Bilgunde, P. and Bond, L.J. "Development of BS-PT based high temperature ultrasonic transducer", In *Proc. SPIE 10170, Health Monitoring of Structural and Biological Systems 2017, 1017014 (2017/04/05*); doi: 10.1117/12.2260324; http://dx.doi.org/10.1117/12.2260324

Bond, L.J. , High Temperature Ultrasonic Transducers for In-Service Inspection of Liquid Metal Fast Reactors, Presentation, Department of Aerospace Engineering Seminar, Iowa State University (2013)

Bond, L. J., Griffin, J. W., Posakony, G. J., Harris, R. V., and Baldwin, D. L. , "Materials issues in high temperature ultrasonic transducers for under-sodium viewing". In *AIP Conference Proceedings*, Vol. 1430, No. 1, 1617-1624, AIP Publishing (2012)

CEA "4th-generation sodium-cooled fast reactors The ASTRID Technological Demonstrator," Direction de l'énergie nucléaire (nuclear energy division), Centre de Saclay, CEA (2012)

Chen, J., Cheng, J., and Dong, S. "Review on high temperature piezoelectric ceramics and actuators based on $BiScO_3$–$PbTiO_3$ solid solutions". *Journal of Advanced Dielectrics*, ***4***(01), 1430002. (2014).

Chen, J., Shi, H., Liu, G., Cheng, J., and Dong, S. "Temperature dependence of dielectric, piezoelectric and elastic properties of $BiScO_3$–$PbTiO_3$ high temperature ceramics with morphotropic phase boundary (MPB) composition". *Journal of Alloys and Compounds*, ***537***, 280-285. (2012).

Chillara, V. K., Ren, B., and Lissenden, C. J. "Guided wave mode selection for inhomogeneous elastic waveguides using frequency domain finite element approach". *Ultrasonics*, ***67***,199-211. (2016).

Chung, J., and Hulbert, G.M. "A time integration algorithm for structural dynamics with improved numerical dissipation: the generalized-α method." *Journal of Applied Mechanics* ***60***, no. 2, 371-375. (1993)

Cobb, A. C., Fisher, J., and Michaels, J. E. "Model-assisted probability of detection for ultrasonic structural health monitoring". In *Proc. 4th European-American Workshop on Reliability of NDE*. (2009).

COMSOL User's guide 4.4-COMSOL Multiphysics reference Manual (2014) www.comsol.com

Cotronics Corporation (http://www.cotronics.com/vo/cotr/ea_ultratemp.htm)

Courant, R, Kurt, F., and Hans,L. "Über die partiellen Differenzengleichungen der mathematischen Physik." *Mathematische Annalen* ***100***, no. 1 (1928): 32-74.

Day, C. K., and Smith, R. W., Under sodium viewing, Report No. HEDL-SA—615, Hanford Engineering Development Lab., Richland, Washington. (USA). (1973).

Dhutti, A., Tumin, S. A., Mohimi, A., Kostan, M., Gan, T. H., Balachandran, W., and Selcuk, C. “Development of Low Frequency High Temperature Ultrasonic Transducers for In-service Monitoring of Pipework in Power Plants”. *Procedia Engineering*, ***168***, 983-986 (2016).

Dierckx, M., Van Dyck, D., Vermeeren, L., and Bogaerts, W. “Research towards ultrasonic systems to assist in-vessel manipulations in liquid metal cooled reactors” *IEEE Transactions on Nuclear Science*, ***61***(4), 2024-2033 (2014).

Eitel, R. E., Randall, C. A., Shrout, T. R., and Park, S. E. “Preparation and characterization of high temperature perovskite ferroelectrics in the solid-solution (1-x) BiScO3–xPbTiO3”. *Japanese Journal of Applied Physics*,***41***(4R), 2099. (2002)

Eitel, R. E., Randall, C. A., Shrout, T. R., Rehrig, P. W., Hackenberger, W., and Park, S. E. “New high temperature morphotropic phase boundary piezoelectrics based on Bi (Me) O3–PbTiO3 ceramics.” *Japanese Journal of Applied Physics*, ***40***(10R), 5999. (2001).

Foust, O. J. Sodium-NaK Engineering Handbook, **1,** Gordon and Breach, Science Publishers, Inc., New York (1972).

Gianneo, A., Carboni, M., and Giglio, M. Feasibility study of a multi-parameter probability of detection formulation for a Lamb waves–based structural health monitoring approach to light alloy aeronautical plates. *Structural Health Monitoring*, Vol. ***16*** (2),225-249,(2017).

Gianneo, A., Carboni, M., Müller, C., and Ronneteg, UPAUT inspection of copper canister: Structural attenuation and POD formulation. In *Review of Progress in QNDE*, Vol 35, D. E. Chimenti, and L. J. Bond (Eds.), AIP Conference Proceedings # 1706, paper 200005). AIP Publishing. (2016).

Giurgiutiu, V., Xu, B., and Liu, W. “Development and testing of high-temperature piezoelectric wafer active sensors for extreme environments”. *Structural Health Monitoring*,***9***(6),513-525 (2010).

Gotmare, S. W., Leontsev, S. O., and Eitel, R. E. “Thermal Degradation and Aging of High-Temperature Piezoelctric Ceramics”. *Journal of the American Ceramic Society,* ***93***(7), 1965-1969. (2010).

Gotmare, S. W., "Thermal Degradation and Aging of High Temperature Piezoelectric Ceramics" (2008). University of Kentucky Master's Theses. paper564.

Griffin, J. W., Peters, T. J., Posakony, G. J., Chien, H. T., Bond, L. J., Denslow, K. M., Sheen, S. H. and Raptis, P. "Under-Sodium viewing: a review of ultrasonic imaging technology for liquid metal fast reactors," PNNL-18292, Pacific Northwest National Laboratory, Richland, WA (2009).

Griffin, J. W., Posakony, G. J., Harris, R. V., Baldwin, D. L., Jones, A. M., and Bond, L. J. "High temperature ultrasonic transducers for in-service inspection of liquid metal fast reactors." In *Ultrasonics Symposium (IUS), 2011* IEEE International ,1924-1927, IEEE. (2012)

Gubinyi Z, Batur C, Sayir A., and Dynys F., "Electrical properties of PZT piezoelectric ceramic at high temperatures," *Journal of Electroceramics*, ***20***(2), pp. 95-105 (2008).

Haun, M. J., Furman, E., Jang, S. J., McKinstry, H. A., and Cross, L. E. "Thermodynamic theory of PbTiO3*" Journal of Applied Physics*, ***62***(8), 3331-3338. (1987).

Hooker M. W., "Properties of pzt-based piezoelectric ceramics between-150 and 250c," NASA/CR-1998-208708, National Aeronautics and Space Administration, Langley Research Center (1998).

Jaffe, B., Cook, Jr., W. R., and Jaffe, H. "Piezoelectric ceramics," *Academic Press*, London (1971).

Janapati, V., Kopsaftopoulos, F., Li, F., Lee, S. J., and Chang, F. K., Damage detection sensitivity characterization of acousto-ultrasound-based structural health monitoring techniques. *Structural Health Monitoring*, ***15***(2), 143-161. (2016).

Jansen, K. E., Whiting, C. H., and Hulbert, G. M. "A generalized-α method for integrating the filtered Navier–Stokes equations with a stabilized finite element method" , *Computer Methods in Applied Mechanics and Engineering*, ***190***(3), 305-319 (2000).

Jensen, F., Mahaut, S., Calmon, P., and Poidevin, C. Simulation based POD evaluation of NDI techniques. In Proc 10th European Conference on Non-destructive Testing, Moscow. (2010).

Jordan, T. L. and Ounaies, Z. 2001 Piezoelectric ceramics characterization. NASA/CR-2001-211225 *ICASE Report No* 2001-28

Kazys, R., Voleisis, A. and Voleisiene, B. "High Temperature Ultrasonic Transducers: Review," Ultragarsas (Ultrasound), ***63***, 7–17 (2008).

Kibe, T., Inoue, T., Namihira, T., and Kobayashi, M. High-temperature-immersion ultrasonic probe without delay line using PbTiO3/Pb (Zr, Ti) O3 ultrasonic transducer. *Japanese Journal of Applied Physics*, ***54***(7S1), 07HB09 (2015).

Kim, T., Kim, J., Dalmau, R., Schlesser, R., Preble, E., and Jiang, X. “High-temperature electromechanical characterization of AlN single crystals”. *IEEE Transactions on Ultrasonics, Ferroelectrics, and Frequency Control*, ***62***(10), 1880-1887 (2015).

Kino, G. S. *Acoustic waves: devices, imaging, and analog signal processing*. Vol. 107. Prentice-Hall (Englewood Cliffs, NJ), 1987.

Kinsler, L. E., and A. R. Frey. Fundamentals of Acoustics"." John Wiley & sons, New York, p25 (1962)

Krimholtz R, Leedom,D.A. and Matthaei,G.L. "New Equivalent Circuits for Elementary Piezoelectric Transducers," *Electron. Lett.,* 6 (6) 398-399. (1970)

Lee, H. J. Bar-Cohen, Lih, S.S., Badescu, M., Bao, X. Sherrit, S. Takano, N., Ostlund, P. and Blosiu, J. "High temperatures health monitoring of the condensed water height in steam pipe systems," In *SPIE Smart Structures and Materials: Nondestructive Evaluation and Health Monitoring*, International Society for Optics and Photonics, pp. 869514-869514 (2013).

Lee, H. J., Zhang, S., Bar-Cohen, Y., and Sherrit, S. “High temperature, high power piezoelectric composite transducers”. *Sensors*, ***14***(8), 14526-14552. (2014)

Leibowitz, L., Chasanov, M. G. and Blomquist, R. "Speed of sound in liquid sodium to 1000 C," *Journal of Applied Physics*, ***42***(5), 2135-2137 (1971).

Lerch, R.,“Simulation of piezoelectric devices by two-and three-dimensional finite elements” *IEEE Transactions on Ultrasonics, Ferroelectrics and Frequency Control*, ***37***(3) 233-247 (1990)

Li Y. H., Kim, S. J., Salowitz, N., and Chang, F. K, “Development of High-Performance BS-PT Based Piezoelectric Transducers for High-Temperature Applications”. In *EWSHM-7th European Workshop on Structural Health Monitoring*. (2014)

Li, M., Meeker, W. Q., and Thompson, R. B. Physical model-assisted probability of detection of flaws in titanium forgings using ultrasonic nondestructive evaluation. *Technometrics*, ***56***(1), pp 78-91. (2014).

Li, S., Cao, W., and Cross, L. E. “The extrinsic nature of nonlinear behavior observed in lead zirconate titanate ferroelectric ceramic”. *Journal of Applied Physics*, ***69***(10), 7219-7224. (1991).

Lopez-Sanchez, A. L., Kim, H. J., Schmerr, L. W., and Sedov, A. “Measurement models and scattering models for predicting the ultrasonic pulse-echo response from side-drilled holes” *Journal of Nondestructive Evaluation*, ***24***(3), 83-96 (2005).

Medina, J.E.S.M., Buiochi, F. and Adamowski, J.C. "Numerical modeling of a circular piezoelectric ultrasonic transducer radiating water." In *ABCM symposium Series in Mechatronics*, vol. 2, 458-464. 2006

Meeker, W. Q. ,RB Thompson's contributions to model assisted probability of detection. In *Review of Progress in QNDE*, Volume 31, AIP Conference Proceedings # 1430, No. 1, 83-94. AIP Publishing. (2012)

Massacret, N., Moysan, J. , Ploix, M. A., Jeannot, J. P. and G. Corneloup, "Modelling of ultrasonic propagation in turbulent liquid sodium with temperature gradient," *Journal of Applied Physics*, ***115***(20), 204905 (2014).

MIL-HDBK-1823 A (2010) MIL-HDBK-1823A, DEPARTMENT OF DEFENSE HANDBOOK: NONDESTRUCTIVE EVALUATION (NDE) SYSTEM, RELIABILITY ASSESSMENT , DOD.

OECD "*Technology roadmap update for generation IV nuclear energy systems*," OECD Nuclear Energy Agency for the Generation IV International Forum (2014). https://www.gen-4.org/gif/upload/docs/application/pdf/2014-03/gif-tru2014.pdf

Parks, D. A., and Tittmann, B. R. "Ultrasonic NDE in a reactor core" In *Sensors, 2011 IEEE* ,618-622, IEEE. (2011).

Parks, D. A., Zhang, S., and Tittmann, B. R. "High-temperature (> 500/spl deg C) ultrasonic transducers: an experimental comparison among three candidate piezoelectric materials". *IEEE Transactions on Ultrasonics, Ferroelectrics, and Frequency Control*, ***60*** (5), 1010-1015. (2013).

Pavlovi, M., Takahashi, K., and Müller, C. Probability of detection as a function of multiple influencing parameters. *Insight-Non-Destructive Testing and Condition Monitoring*, ***54***(11), 606-611. (2012).

Piezo Technologies (http://www.piezotechnologies.com/)

Randall, C. A., Kim, N., Kucera, J. P., Cao, W., and Shrout, T. R. "Intrinsic and extrinsic size effects in fine-grained morphotropic-phase-boundary lead zirconate titanate ceramics". *Journal of the American Ceramic Society*, ***81***(3), 677-688. (1998).

Roy, S., Lonkar, K., Janapati, V., and Chang, F. K., "A novel physics-based temperature compensation model for structural health monitoring using ultrasonic guided waves". *Structural Health Monitoring*, ***13***(3), 321-342. (2014).

Sabat, R. G., Mukherjee, B. K., Ren, W., and Yang, G. "Temperature dependence of the complete material coefficients matrix of soft and hard doped piezoelectric lead zirconate titanate ceramics" Journal of Applied Physics, 101(6), 06411 (2007).

Salmanpour, M. S., Khodaei, Z. S., and Aliabadi, M. H. “Guided wave temperature correction methods in structural health monitoring”. *Journal of Intelligent Material Systems and Structures*, 28(5), 604-618.,(2017). https://doi.org/10.1177/1045389X16651155

Sarkar, P., Meeker, W. Q., Thompson, R. B., Gray, T. A., and Junker, W. “Probability of detection modeling for ultrasonic testing”. In *Proc. Review of Progress in Quantitative Nondestructive Evaluation*, vol.17, Plenum press, New York , 2045-2052 (1998).

Schmerr, L.W. *Fundamentals of Ultrasonic Nondestructive Evaluation: a Modeling Approach*, New York: Plenum, (1998).

Searfass, C. T., Pheil, C., Sinding, K., Tittmann, B. R., Baba, A., and Agrawal, D. K., “Bismuth Titanate Fabricated by Spray-on Deposition and Microwave Sintering for High-Temperature Ultrasonic Transducers”. *IEEE transactions on Ultrasonics, Ferroelectrics, and Frequency Control*, ***63***(1), 139-146. (2016).

Sherrit, S., and Mukherjee, B. K., Characterization of Piezoelectric Materials for Transducers, [in:] Dielectric and Ferroelectric Reviews, S.N. Srowthi, Bharadwaja and Robert A. Dorey [Eds.], Research Singpost, 175-244.(2012)

Smith, K. D. “POD Transfer Function Approach”. In *MAPOD Working Group Meeting* (Vol. 4). (2005, February).

Smith, K., Thompson, B., Meeker, B., Gray, T., and Brasche, L. “Model-Assisted Probability of Detection Validation for Immersion Ultrasonic Application”. In D. O. Thompson, & D. E. Chimenti (Eds.), AIP Conference Proceedings (Vol. 894, No. 1,1816-1822) (2007).

Subair, S. M., Balasubramaniam, K., Rajagopal, P., Kumar, A., Rao, B. P., and Jayakumar, T., “Finite element simulations to predict probability of detection (PoD) curves for ultrasonic inspection of nuclear components”. *Procedia Engineering*, ***86***, 461-468. (2014)

Tang, L., and Cao, W. “Temperature dependence of self-consistent full matrix material constants of lead zirconate titanate ceramics”. *Applied Physics Letters*, ***106***(5), 052902. (2015)

Thompson, R. B. A Unified Approach to The Model-Assisted Determination Of Probability of Detection. In D. O. Thompson, & D. E. Chimenti (Eds.), AIP Conference Proceedings (Vol. 975, No. 1, 1685-1692). (2008).

Wang, Y., Gao, L., Yuan, S., Qiu, L., and Qing, X. “An adaptive filter–based temperature compensation technique for structural health monitoring”., *Journal of Intelligent Material Systems and Structures*, ***25***(17), 2187-2198. (2014)

Wirdelius, H., and Persson, G. “Simulation based validation of the detection capacity of an ultrasonic inspection procedure” *International Journal of Fatigue*, ***41*** , 23-29. (2012).

Yusa, N., Chen, W., and Hashizume, H. “Demonstration of probability of detection taking consideration of both the length and the depth of a flaw explicitly”. *NDT&E International*, ***81***, 1-8. (2016).

Zhang, S. and Fapeng, Y. "Piezoelectric materials for high temperature sensors," *Journal of the American Ceramic Society*, ***94*** (10) , 3153-3170 (2011).

Zhu, Jie. “Optimization of matching layer design for medical ultrasonic transducer”. The Pennsylvania State University, PhD Thesis (2008)

NEUP – Final Report

Advance High Temperature Inspection Capabilities for Small Modular Reactors

Part 2 – Eddy Current Inspection under Conductive Liquid Coolant

John R. Bowler and Tau Wu

PI Leonard Bond

Center for Nondestructive Evaluation
Iowa State University

Applied Sciences Complex II
1915 Scholl Road
Ames, IA 50011-3042

Tel. 515-294-8152

Program RCD&D: Instrumentation, Control Human Machine Interface
Nuclear Energy University Program – Project # RPA-13-5150,

U.S. Department of Energy

Introduction

This document: Eddy Current Inspection under Conductive Liquid Coolant, is Part 2 of the final report on the NEUP project on Advanced High Temperature Inspection Capabilities for Advanced Small Modular Reactors, project RPA-13-5150, carried out at the Center for Nondestructive Evaluation, Iowa State University.

The overall aim of the project is to investigate the development of non-destructive evaluation techniques for the inspection of advanced small modular reactors (SMR) and to examine the potential effectiveness of inspection technologies needed to inform the design, maintenance and reliability of the reactor operation.

Two inspection technologies were investigated to assess their effectiveness in sodium cooled SMR's under standby conditions. The first focused on high temperature ultrasonic transducers development, the results of which were given earlier in Part 1 of this report. Here, in Part 2, we report on eddy current inspection capabilities. For both inspections types, the primary aim is to assess the potential for developing in-service inspection techniques that can be carried out under standby condition in a sodium cooled fast reactor at a temperature of approximately 250°C in the presence of the coolant in its liquid state. The goal is to extend our understanding of the methods that may be used and to aid in the formation of an inspection strategy that will ensure the safe operation of the reactor between scheduled inspections carried out under standby conditions.

CONTENTS

Statement of the Project Objectives

- **Task 1 investigation of performance of ultrasonic transducers at temperature and in conductive and low-conductivity environment.**

    - **Year 1**. Models and experiments would be initiated in year 1. The liquid metal/molten salt room temperature EMI test cell would be designed and built in year 1.
    - **Year 2**. Tests would continue into year 2. The insights gained would be used to guide development of novel screened transducers.
    - **Year 3** could involve transducer testing at temperature in oil.

- **Task 2 would be an investigation of the potential NDE options employing ultrasound and eddy current in a liquid metal and molten salt.**

    - **Year 1**. Application of NDE simulation codes to a range of configurations, and inspection variants.
    - **Year 2.** Data generation and preliminary POD estimation. Experiments would be performed using the liquid metal and molten salt surrogate to obtain 'filled" fatigue crack reflectivity data.
    - **Year 3.** More formal POD estimation, including potentially additional data collection for crack detectability.

- **Task 3 would focus on assessment of novel ISI capabilities for advanced small modular reactors.**

    - Mainly a year 2-3 activity that would consider both sensors and the use of models.

- **Task 4: Assessment of in-service (ISI) capabilities for advanced small modular reactors.**

    - This will be initiated in Year 2 and be completed in Year 3**.**

Abstract

The eddy current activities reported here assess the fundamental limiting factors of eddy current inspection in a sodium cooled fast reactor under standby conditions. These factors are critically dependent to on the extent to which the eddy current signal due to a flaw in the structure is reduced when the inspection takes place under liquid metal. As a surrogate for liquid sodium at a stand-by temperature of 250°C, a gallium-indium-tin mixture, was used at room temperature. Eddy current inspection at 250° is not does not usually present a major problem due to the temperature in itself since on-site industrial eddy current inspections up to 400°C are routinely performed.

In the case of molten salt reactors the standby or inspection conditions are not extensively discussed. With the salt melting temperature typically above 400ºC and inspection using eddy current with an immersed probe is unlikely to be viable with existing technology. One would not however rule out the possibility that probes operating in the range from 400ºC-800ºC could not be produced. An alternative strategy is to drain the reactor for inspection and maintenance in which case the conditions for successful inspections is dependent, amongst other things, on the salt residue.

Experiments were carried out to determine the signal variation with probe lift-off and determined probability of detection (PoD) data from the measurements. The probe signal level can be reduced by an order of magnitude or more when an inspection takes place in immersion conditions using standard coil inspection. The probe lift-off is a critical parameter due to absorption of the electromagnetic field in the intervening coolant. However, even a reduction in signal by a factor of ten, which can observed in these circumstances does not mean that eddy current inspection would not be effective but it does imply that the inspection is likely to take longer than one in which the conductive coolant was absent.

Traditional heat exchanger tube eddy current inspections in a pressurized water reactor are performed rapidly in order that a reactor is off-line for a relatively short period. However, a similar inspection with sealed probe modules immersed in liquid metal will take a longer time and require close coupling with the tube wall to reduce signal attenuation in the coolant. Measurements with small ferrite cored probes at the surface produces the best performance and to speed up the inspection process these could be used in arrays to reduce inspection times.

Typical eddy current nuclear reactor tube inspections are carried out with a differential or absolute bobbin coil probes but the response varies only in the axial direction. Essentially then, this is a one dimensional scan but it can be carried out is such a way as to minimize the coil “lift-off” i.e. the gap between coil and metal surface. If the lift-off gap is filled with liquid sodium, the effect would be to limit the field transmitted from probe to flaw and back and hence significantly attenuate the probe flaw signal. However, the absorption can be minimized by making this gap small using a thin ware-resistant coating on the coil. One possibility is to spring load the coated coil onto the tube wall to minimize attenuation in the coolant. Given that we observe cracks even in the presence of a liquid metal surrogate, minimizing the “gap” offers a viable solution. Predictions of signal response to flaws can be made using the probe-flaw interaction models developed and adapted for this project.

1. Eddy Current testing in a Fast Reactor

1.1 Technical Considerations

The fundamental challenges faced in using eddy current testing to evaluate the condition of metallic structures in a fast reactor environment are related to the high temperatures encountered and the presence of conductive coolant. The operational challenges are related to the need to monitor and control the probe position both when moving it into position and while acquiring data. There is also a need to transmit the data, perhaps over a distance of several meters, to a collection point for analysis. The transmission requirement must overcome potential problems of electromagnetic interference with a weak signal which cannot be easily amplified at its source due to limitations on the use of electronic circuits at high temperatures.

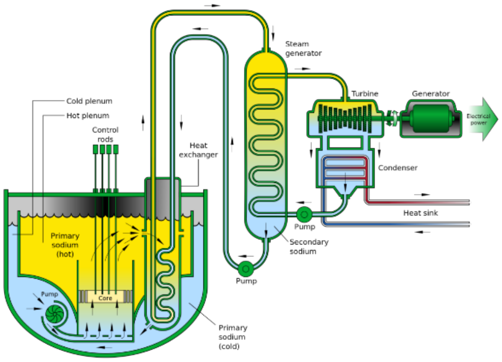

Figure 1: GE-Hitachi PRISM, metal fueled 311 MW [1].

.

We focus on the fundamentals of inspection technologies, since these relate directly to the viability of inspecting a fast reactor under standby conditions without having to speculate on the specific circumstances of a particular inspection. In the case of the liquid sodium cooled fast reactor, an eddy current inspection technique is sought that will be effective with the liquid metal present at a standby temperature of 250°C (melting temperature 97.2°C). Under these circumstances it is not self-evident that eddy-current inspection would be effective but it is of value to resolve this question.

To seek a resolution we note that an eddy current probe induces current in the coolant between it and the material under test which means that coolant acts as a shield to reduce the current induced in the underlying structure. Interaction of induced current with a defect influences the probe impedance from which the presence and even the geometry of the defect: both size and shape, can be inferred.

In the case of inspections under liquid sodium, the coolant conductivity is several times that of the structural steels that are commonly used or are candidates for use in fast reactors (Table 1). This implies that the amount of coolant between the probe and the workpiece needs to be small; say less than 1.0 mm thick. In addition, the skin effect implies that optimum conditions for flaw detection include operating at a relatively lower frequencies if a layer of intervening coolant present.

The material to be used for heat exchanger tubes in sodium cooler reactors remains a subject for continuing research with several countries, including France, India, Canada, and the US pursuing differing paths. The fact that ferritic steels in particular cannot be ruled out is significant for the present discussion since it would be easier to detect defects using eddy currents if a ferritic steel were to be used for the heat exchanger tubes [2]. A crack produces a discontinuity in conductivity and permeability in a ferromagnetic material which is present below the Curie temperature of the material. This means that there are two physically distinct contributions to the eddy current probe response to a flaw in a ferromagnetic material which is likely to lead to an increase in the detection probability [3].

1.2 Initial Preparations

1. A new three axis scanning system was installed and tested in a CNDE laboratory with the aim of carrying out measurements at room temperature using a liquid metal surrogate for liquid sodium. Although the liquid metal was not considered to be a hazardous material, the experiments were carries out in a fume cupboard and protective gloves were worn as precautionary measures against contamination through contact with the liquid.

2. In addition, another scanning system with six degrees of freedom, three Cartesian, a rotary stage and two manually operated tilt stages for fine sample adjustments, has been used for carrying out independent reference measurements on samples in air. Its role is mainly to corroborate model predictions against experiments. The rotary stage is used to scan tubes and pipes internally or externally in the azimuthal or axial direction.

3. In order to perform the eddy current measurements of probe impedance variations due simulated cracks, a high sensitivity electronic system was needed to detect signals and provided a means to make a well-founded assessment of the feasibility of using eddy current testing in a fast reactor. This was accomplished using a high performance commercial lock-in amplifier from Zurich Instruments [4] covering the frequency range from DC to 5.0 M Hz. This allows access to analog and digital signals, connects to a personal computer and includes signal display software.

4. The lock-in amplifier provides accurate measurements of the amplitude and phase of an alternating current signal over a range of frequencies to 5 MHz and can deliver a superior signal to noise performance compared to that of a commercial eddy current test instrument. In fact we verified that its signal to noise performance exceeded that of an Agilent Impedance analyzer [5]. In addition, the lock-in has in-built software that can be accessed by interfacing it with a computer. Thus data acquisition is controlled automatically to provide high resolution two dimensional scans over selected defects.

5. A range of test samples, details given in the Appendix, were designed and ordered from VM Products. This company has previously supplied controlled test specimens and precision eddy current probes to CNDE that have been used for controlled eddy current testing and for benchmark measurement that are used to validate theoretical predictions of probe signals for comparison with experimental measurements.

1.3 Experiment and Simulations

2. A program of sample testing has been carried out in which probe impedance measurements were made under controlled conditions in air and under a Ga-In-Sn liquid metal to (a) validate computer models of eddy current probe-flaw interactions (b) determine the performance of the eddy current measurement system and (c) establish a procedure for carrying out probability of detection studies for flaws immersed in liquid metal coolant.

3. A set of samples containing accurately made artificial defects were used to carry out a testing program on a range of simulated flaws in materials chosen to match those used in the past for nuclear reactor structures.

4. In-house model development has been carried for example to investigate the interaction of a probe at an arbitrary angle to a tube to detect the tube orientation [6] and to correlate predictions with measurements using a code EC Sim and with the results of commercial code (Comsol Multi-Physics [7]).

2.0 Measurements

2.1 Probe Impedance Data Acquisition

Eddy current test instruments operate typically over a frequency range from 100 Hz to 5 MHz by measuring the potential drop, both in phase and quadrature components, across a probe consisting of a coil with a possibly a ferrite core. For research purposes it is better to use a lock-in amplifier to get precise probe impedance data but this must be used with an add-on circuit to get calibrated data on the current through the probe and the potential drop across it. There-bye one obtains probe impedance changes.

Figure 2: Zurich instruments lock-in amplifier for measurement of the amplitude and phase of signal voltages in the range up to 5 MHz [4].

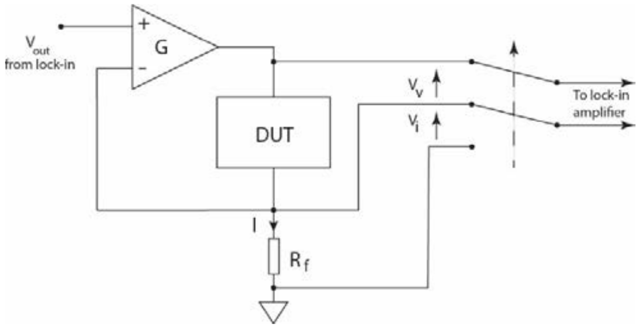

Figure 3: The trans-conductance amplifier G provided current to the device under test (DUT). The lock-in measures both the potential drop across the DUT and the voltage drop across the standard resistor to determine the impedance.

The lock-in amplifier determines the amplitude and phase of a voltage measured with respect to an internal phase reference but in order to determine eddy current probe impedance, we measure both the voltage across a standard resistor in series with the eddy current probe to infer the probe current and the potential difference across the probe itself. Dividing the latter by the current gives the probe impedance. The two measurement required are made by switching the lock-in amplifier input between the standard resister, R_f and the device under test, labeled DUT in Figure 3.

We designed an add-on system 2, Figure 4, and a more advanced add-on circuit (System 3) should it be needed. In System 2, a digital signal is measured by the lock-in and fed back via a direct digital synthesizer to remove a background signal voltage across the eddy current prone (DUT). In this way one creates a null signal when the DUT output and the reference feed are the same. This means one can measure the flaw signal with the background signal subtracted and thereby get a more accurate measure of the flaw signal. System 3 was held in reserve in case we needed to reduce errors in the performance of System 2 but was not needed.

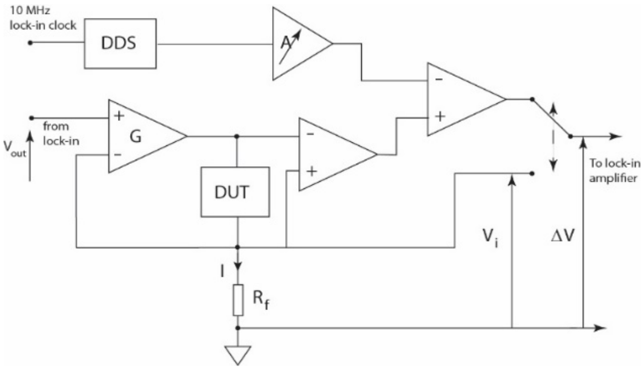

Figure 4: System 2 shows the feed-back of a digital reference signal which is synthesized and subtracted from the voltage from the DUT (i.e. the eddy current probe).

2.2 Measurement of Material Properties of Steel

In order to predict the eddy current probe signals due to notches in ferromagnetic material it is necessary to know both the electrical conductivity and the magnetic permeability of the material. Although the austenitic steel is expected to have a relative permeability close to 1.0, see Table 1, this needs to be confirmed. Measurement of permeability have being carried out on all test specimens using an alternating current potential drop instrument with a four point probe, *Fig.5*. The theory for establishing reliable permeability as well as conductivity data from the measurements was developed at CNDE [8-10].

A prototype circuit board for measuring both steel material properties is shown in *Fig. 6*. The add-on for converting the lock-in amplifier to an impedance measuring unit is also included in this prototype board. We have recently reconfigured this system as separate circuits and carry out modification to improve on the performance in order to establish an estimate of the state of the art limits of PoD for cracks including those immersed in liquid metal.

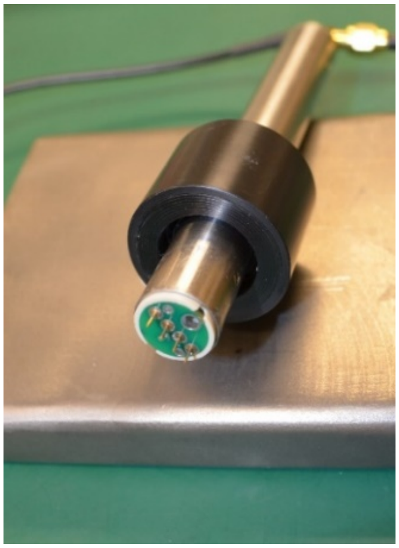

Fig. 5: Four point probe for accurate measurement of permeability and conductivity.

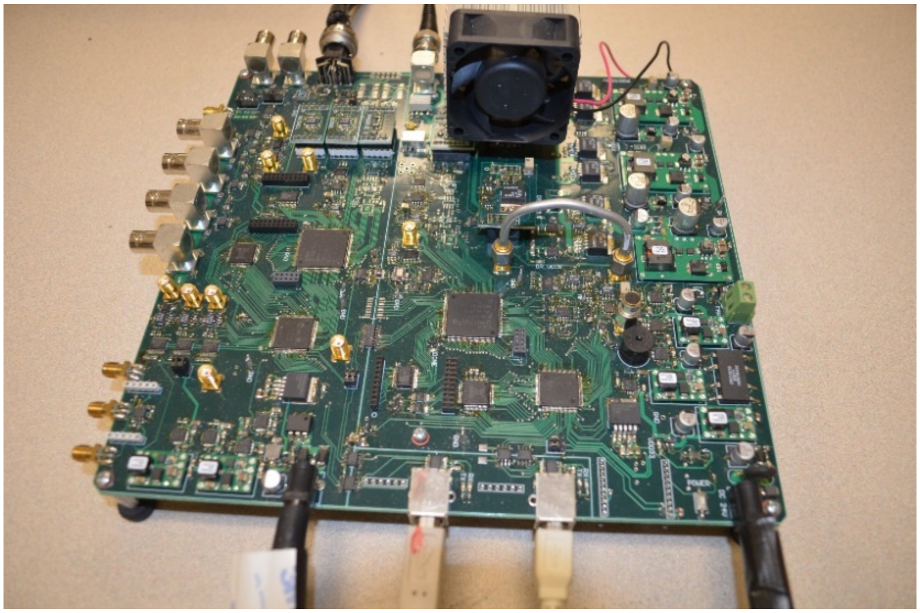

Fig. 6: Circuit board which includes an add-on circuit for use with the Zurich lock-in amplifier on the left side of the circuit board and on the right a prototype an alternating current potential drop (ACPD) measurement circuit. At the top of the picture, the large object is a heat sink for a trans-conductance amplifier (TCA) which provides a predefined current to the probe at frequencies below 10 kHz. A smaller TCA provide current at frequencies from 10 kHz to 100 kHz.

The performance of the measurement system has been compared with that of an Agilent Impedance Analyzer 4297. Sample results, in Fig7, show that the enhanced Zurich lock-in based system has a signal to noise performance that is significantly better than that of the Impedance Analyzer.

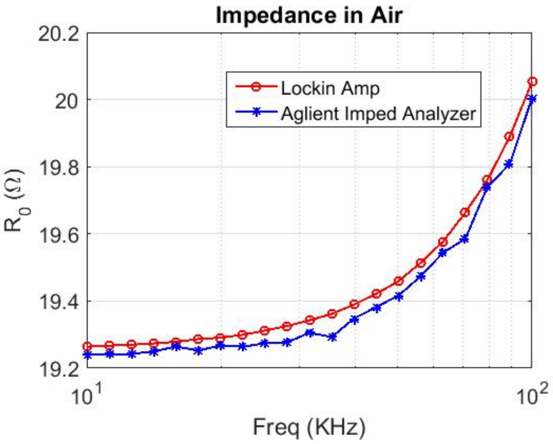

Fig. 7: Variation of an eddy current probe resistance with frequency. (a) In red, using measurements made with an enhanced Zurich Instruments lock-in and (b) in blue, using an Agilent Impedance Analyzer.

3. Test samples and measurements.

3.1 Procedures

Our aim was to complete a feasibility study on the effectiveness of using eddy current testing to assess the condition of fast reactor structures under standby conditions. Although we do not carry out measurement at 250º C, it is not uncommon for commercial organizations to carry out inspections at this temperature or higher. In a reactor environment such measurements can be perform with the probe module a few meters of the test instrument. An immersed module with a passive probe could certainly operate at this temperature. The probe signal would then be transmitted to the measuring instrument. Under these circumstances measurement at high temperature would not have a major effect on the ability to resolve a flaw signal.

Eddy current measurements on steels samples have been carried out in a liquid metal environment using a surrogate fluid (Ga-In-Sn alloy) to mimic the effects of liquid sodium. The measurements were taken on a range of samples with notches to simulate cracks in the material. Although it may be argued that realistic cracks could have provide a better test, we were primarily aiming to establish the feasibility range of eddy current testing and use validated models to predict additional results. The models can include the effects of narrowing or the closing the simulated crack. It seemed reasonable therefore, to consider only artificial flaws and to use validated models to investigate configurations that will not be addressed in the experimental program.

Three types of steel was used for testing: 316 SS and 304 SS plus a 400 series ferritic stainless steel. The aim being to acquire initial data that could be used in assessing inspection capabilities on tubes and at support structures. The ferritic steel is include since its properties are somewhat similar to those of possible choices for fuel cladding, for example, oxide dispersion strengthen (ODS) steel are expected to be used for this purpose because of the tolerance the fast a fast neutron flux [11,12]. In addition ferritic steels are being considered for heat exchangers and remain a possible option for SMR's. It was not necessary to use an actual ODS steel, although it is available through Ames Lab at Iowa State. Instead we used instead 400 series stainless steel with similar electromagnetic properties.

A significant property of ferromagnetic steel is that it will exhibit a large material contrast in permeability with respect to the liquid coolant. For 316 and 304 SS the permeability is so close to 1.0 that the magnetic contribution to the eddy current signals is small. The permeability of ferritic steel provides an enhanced mechanism for the detection of cracks/notches that is not present in a non-ferrous metal. Clearly this is of particular interest in this context since it improves the probability of detection.

The samples chosen were plates and tubes. Tubes can be inspected both externally and from the inside and by using the remote field techniques [13-15]. Both plates and tube have been modeled using integral equation methods applied to both ferromagnetic and non-ferromagnetic steels [16-19]

Reactor (Country)	Fuel Cladding	Vessel	Primary/Secondary Piping	IHX	Steam Generator
EBR-II (USA)	316	304	304/304	304	Fe 2¼Cr 1 Mo
Super Phenix (France)	Fe-15Cr-15Ni-Mo-Ti-Si	316	316/316	316L(N)	Alloy 800
Monju (Japan)	316	304	304/304	304	Na-air exchanger
JSFR (Japan)	ODS Ferritic	316FR	9Cr or 12Cr steel		12 Cr steel

Table 1: Materials used in a sodium cooled fast reactors.

3.2 Model Developments

The modeling software we have developed is based on semi-analytical methods for predicting the response of an eddy current coil due to cracks and corrosion in tubes and plates. This software is far easier to use than finite element codes such as Comsol Multiphysics and two to three orders of magnitude faster for performing similar calculations. For example, it will compute the signal due to a notch in a tube, in less than half a second. The program, however, is limited in flexibility at present in that tube expansion regions cannot be modelled currently, nor can a complex tube support structure. This limitations can however be overcome in the future. The EC Sim (Eddy Current Simulation) model can handle arbitrary flaw geometry using volume elements. Because the flaw is small, few elements are needed and the computation is fast.

The advantage of such models is that the user set-up time and computational cost is low and accuracy relatively easy to control. Our codes are similar to those developed by the group of researchers at CEA at Saclay, near Paris, with which we have a long term collaboration and who are largely responsible for developing the commercial CIVA codes.

The semi-analytical approach taken here and in the CIVA codes is based on integral methods which basically means that an integral equation is defined whose solution represents the effective electric and magnetic sources in the flaw region that are excited by the eddy current probe. If the material is not ferromagnetic, the magnetic source is not needed. Once the source densities distributed over the flaw region are known, the impedance change due to the flaw can be calculated using a relationship derived using a reciprocity theorem.

The integral kernels used are analytical forms each dedicated to a particular structure such as a tube, plate or an object having a more complex geometry. In these circumstances, only the flaw region needs to be rendered in discrete form. The codes are used to calculate the electromagnetic source densities represented as electric and magnetic dipole densities which give rise to the perturbed field due to flaws. The region of the flaw is often very small. Consequently only a few unknowns are needed to represent the dipole distribution in the flaw region which leads to fast calculations, typically two of three orders of magnitude faster than a typical finite element code. The disadvantage of the approach, at present, is that it can only be used for canonical structures that are relatively simple to handle analytically because they conform to a particular coordinate system. For example a tube is simply defined in terms of cylindrical polar co-ordinates as is the co-responding integral kernel for the structure.

To solve a more general problem further development are taking place to maintain the speed of calculation for complex structures by segmenting a particular problem at surface boundaries. At the boundary, a solution in one localized coordinate system is matched with the solution in another though a predefine matrix. Thus an arbitrary structure can be modelled by segmenting it into regions defined in terms of a fundamental coordinate system.

For plates and tubes and, and in particular, for the specimens that we are using in this project, the approach used in EC sim is more than adequate and has been tested for ferromagnetic and non-ferromagnetic materials both for flaws in plates and for flaws in tubes.

3.3 Experiments for code validation

Typical eddy current nuclear reactor tube inspections are carried out with a differential or absolute bobbin coil probes but the response varies only in the axial direction. Essentially then, this is a one dimensional scan but it can be carried out is such a way as to minimize the coil “lift-off” i.e the gap between coil and metal surface. If the lift-off gap is filled with liquid sodium, the effect would be to limit the field transmitted from probe to flaw and back and hence significantly attenuate the probe flaw signal. However, the absorption can be minimized by making this gap small. This may be done using a thin ware-resistant coating on the coil. By spring loading the coated coil onto the tube wall the attenuation can be minimised. In addition, the signal due to lift off variation would be minimised especially if the internal surface of the tube is smooth.

Experiments with a rotary probe, Figs. 9 and 12, locate the defect on the surface and can be used to provide better test for a model that predicts the characteristic size and shape of the probe response. A critical parameter is the probe lift off which is determined by fitting a multi-frequency signal simulation to the observed data, Figure 10 and 11. An example of the results of a validation study is shown in Figure 13 where experimental results, determined in this case using an Agilent Impedance Analyser are compared with experiment thus validating the predictions.

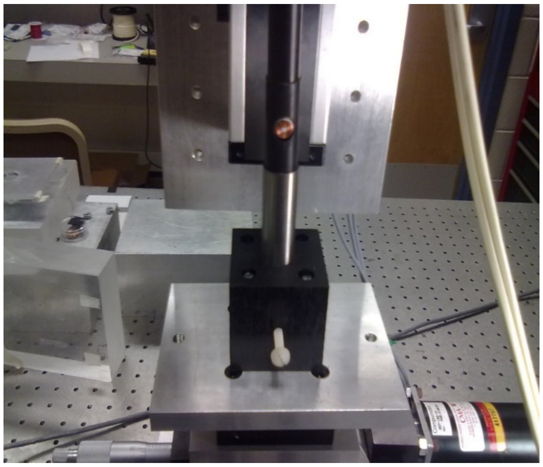

Figure 9: Rotary probe inserted into an Inconel tube contain a notch

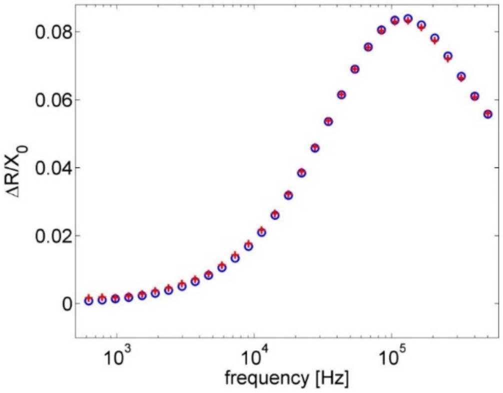

Figure 10: Variation of probe resistance with frequency, normalized to the free-space reactance Xo. Theory, red circles, has been fitted to the data to determine conductivity and lift-off.

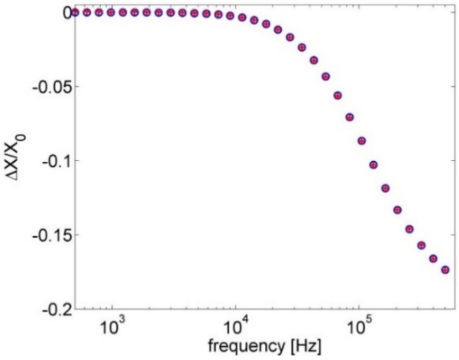

Figure 11: Variation of probe reactance with frequency normalized to the free-space reactance Xo. Theory, red circles, has been fitted to the data to determine conductivity and lift-off.

Figure 12 shows a rotary probe coil which is used as a benchmark study to test a modelling code for its ability to predict the impedance variation of the coil due to a through wall notch. The probe can be rotated in the tube and translated in the axial direction to get a complete coverage of the tube wall. In this case, the predictions are compared with measurement, Figure 13, acquired using an axial scan with the coil axis in the plane of the notch.

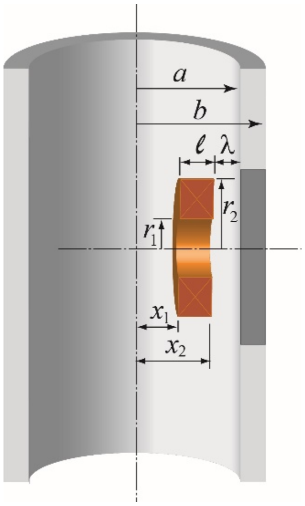

Figure 12: Rotary probe coil interacting with a through wall notch.

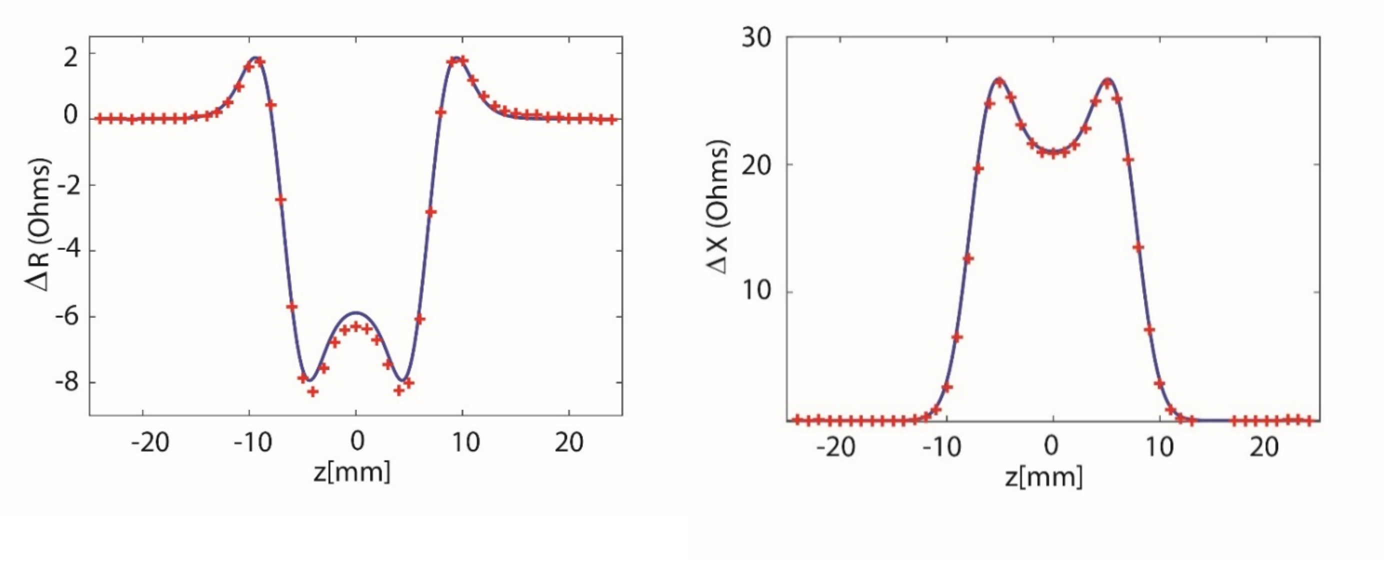

Figure 13: Comparison of the reactance variation and resistance variation of a rotary coil with position, due to a longitudinal notch in an inconel tube.

3.4 Material Properties

Liquid-Metal	Electrical Resistivity	Conductivity (rel. permeability)
Lead-bismuth eutectic [1]	112 μΩ-cm	0.89 MS/m
Sodium (@400K)	14.8 μΩ-cm	6.8 MS/m
Molten salt	6.6 mΩ-m	0.02 MS/m
316 SS (68°C)	74 μΩ-cm	1.35 MS/m (1.02)
304 SS (68-1200°C)	72 - 116 μΩ-cm	1.39 - 0.86 MS/m (1.04)
Lead (600K) [2]	94 μΩ-cm	1.06 MS/m
Ga-In-Sn (300 K, 27°C) [3]	25 μΩ-cm	4.0 MS/m

Table 2: Some relevant material properties are listed here. In particular, note that the listed electrical conductivity of Ga-In-Sn at room temperature is somewhat lower than that of sodium at room temperature but of similar magnitude.

	Material properties of test specimens			
Material	**Young's Elastic Mod. (GPa)**	Density (Kg/m^3)	Relative Permeability	Conductivity MS/m
316 SS	198 (Ref. 3)	8000	1.003-1.05	1.334 (Ref. 1)
304 SS	200 (Ref. 3)	8030	1.003-1.05	1.450 (Ref. 1)
440 SS	200	7650 (Ref 2)	62 (max)	1.667 (Ref 2)

Table 3: Properties of materials used for eddy current testing

1. http://hypertextbook.com/facts/2006/UmranUgur.shtml
2. http://www.azom.com/article.aspx?ArticleID=1024
3. http://pubs.acs.org/doi/full/10.1021/je400882q?src=recsys&

3.5 Eddy Current Probes

In this project we have used basic absolute probe coils without ferrite cores. This is in fact in line with traditional tube inspection in the nuclear industry. The coils are sealed in such a way as to ensure the lift-off, which is the minimum distance for the coil to the surface of the structure under test, is small. It is notable however that ferrite cores that are suitable for use at the target operating temperature of 250°C and have a relative permeability of 40, are available. In general then it is possible to obtain high performance ferrite [20] for high temperature applications.

3.6 Measurement of the Conductivity and Permeability of the test samples

The material parameters, electrical conductivity and magnetic permeability of all test samples, was measured to ensure that these parameters can be used in modeling and simulation of the flaw interaction with the probe. Although eddy current measurements of conductivity can be done reliably for non-magnetic material, conductivity measurement has inherent uncertainties for magnetic material. This is due to the fact that eddy current probe impedance changes on an unflawed plate at moderate and high frequencies depends on the product of the conductivity and permeability. At low frequencies the parameters are to some extent separable, but the eddy current signal weakens and becomes less easy to measure accurately at low frequencies. This is because the induced current is depends on the rate of change of the field which diminishes as the frequency is decreased.

A more effective way of finding both electrical conductivity and magnetic permeability accurately is by using a four point probe [8-10]. Because the current is injected via two contact pins from a trans-conductance amplifier, there is a negligible variation in the current as a function of frequency. Furthermore, measurement can be carried out with a DC current, or preferably at very low frequency to eliminate thermal-electric effects. The measurements of potential drop using two pick-up pins at low frequency is then dependent on conductivity, with a negligible contribution from the permeability. This happens when the skin depth is much greater that the pin separation. At high frequency, the pick-up voltage is like the eddy current measurement in that it is dependent on the electrical conductivity and permeability, but as one approaches the high frequency limit, where the skin depth is much smaller that the pin separation, it is dependent on the product of electrical conductivity and magnetic permeability. By using the low frequency value of conductivity, the permeability can be found from the higher frequency measurements. Thus if the variation of permeability with frequency is small as is usual at say, less than 10 MHz, then both conductivity and permeability can be found accurately using alternating current potential drop measurements.

Reactor (Country)	**Fuel Cladding**	**Vessel**	**Primary/ Secondary Piping**	**IHX**	**Steam Generator**
EBR-II (USA)	316	304	304/304	304	Fe 2¼Cr 1 Mo
Super Phenix (France)	Fe-15Cr-15Ni-Mo-Ti-Si	316	316/316	316L(N)	Alloy 800
Monju (Japan)	316	304	304/304	304	Na-air exchanger
JSFR (Japan)	ODS (Ferritic)	316FR	9Cr or 12Cr steel		12 Cr steel

Table 4: Materials used in a sodium cooled fast reactors.

A range of test samples prepared from the materials referred to in Table 4 were designed for benchmark testing for validation of models and for estimating probability of detection under liquid metal. These had electrical discharge machined (EDM) notches of various sizes to simulate cracks. Both flat plate and tubes samples were obtained together with a set of precision manufactured coils which could be accurately modelled using an eddy current computer code EC sim to simulate probe-flaw interactions in plates and tubes. We have written several conference articles on the underlying theory that forms the basis for the code [3, 6, 17-19]. In addition three journal articles have been drafted. At the time of writing the first of these has been accepted, subject to modifications suggested by the reviewers. Also further measurements are being carried out to be used for future articles.

Recent developments have made extensive use of these samples by testing them in air and under liquid metal, using a surrogate fluid (Ga-In-Sn alloy) that can be used at room temperature to mimic the effect of sodium coolant and in particular to investigate the effect of the liquid metal on the strength of the signals obtained using eddy current inspection techniques. We have also developed a probability of detection (PoD) procedure that can be adapted for fast reactor inspection under liquid metal during standby conditions.

		Material properties of test specimens materials (online references)		
Material	Young's Elastic Mod. (GPa)	Density (Kg/m^3)	Relative Permeability	Conductivity MS/m
316 SS	198 (Ref. 3)	8000	1.003-1.05	1.334 (Ref. 1)
304 SS	200 (Ref. 3)	8030	1.003-1.05	1.450 (Ref. 1)
440 SS	200	7650 (Ref 2)	62 (max)	1.667 (Ref 2)

Table 5: Material properties of 316 304 and 440 steel according to the on-line references below.

1. http://hypertextbook.com/facts/2006/UmranUgur.shtml
2. http://www.azom.com/article.aspx?ArticleID=1024
3. http://web.ornl.gov/info/reports/1979/3445605704100.pdf

4 Model Validation

4.1 Experiments on a Notch in Ferritic Steel

The comparison of model predictions and the results of controlled experiments validate the models [19]. In the case of ferromagnetic materials, this is a challenging exercise because the permeability of the material may be non-uniform in the region of a notch due to the heating effects of spark-erosion or due to other factors such as residual stress variations. We have developed a model for predicting the impedance variation of a coil due to a flaws in ferromagnetic steel such as 440 SS, in which the effect of the simulated flaw is represented by an electrical and a magnetic dipole distributions. The dipole densities in the flaw region are calculated and the probe impedance expressed in terms of these source densities using an expression derived using a reciprocity theorem.

Coil Inner Radius	2.82 mm	Notch Width	0.16 mm
Coil Outer Radius	4.51 mm	Semi-Ellipse Notch Dimensions	8.029 x 1.999 mm
Coil Width	1.78 mm	440 SS Specimen Thickness	13 mm
Number of Turns	306	Conductivity	1.41 MS/m
Liftoff	0.82 mm	Relative Permeability	70.3

Table 6: Test Specimen and Notch Parameters

Measurements have been made to obtain a set of results for a particular 8 mm long semi-elliptical notch, at 5 kHz, on the sample shown the Appendix, *Fig. A2*. This is a ferromagnetic sample: 440 SS. The resistance and reactance components of the flaw signal are shown in *Fig.14* for a scan in the direction perpendicular to the plane of the notch. For a scan with the coil axis in the plane of the notch, the corresponding results are shown in *Fig. 15*. On the whole agreement with experiment is good although the results for the reactive component when traversing over the length of the notch show some small discrepancies between theory and experiment.

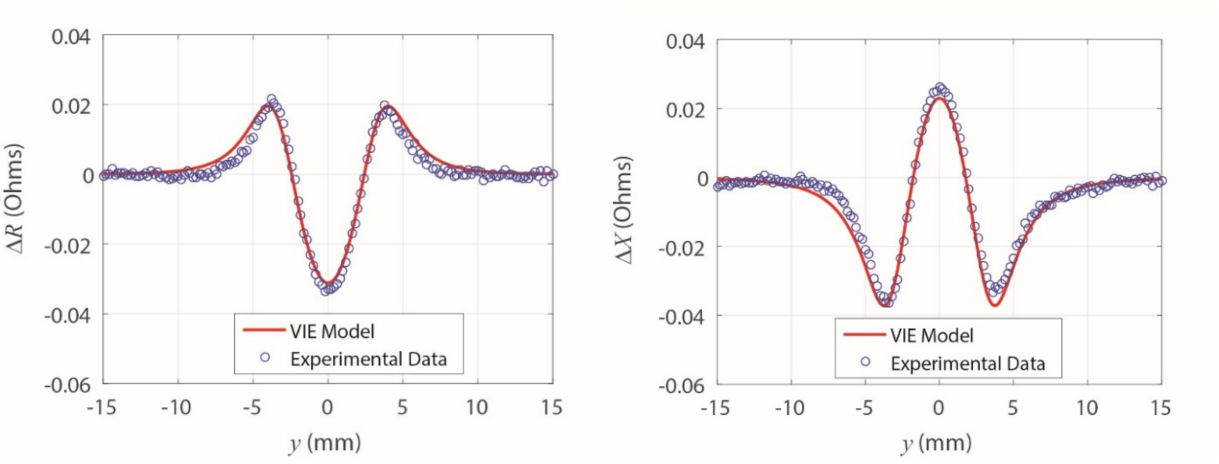

Fig 14: Variation of coil resistance and reactance as it traverses a notch in the direction perpendicular to the notch plane: comparison of model predictions and experimental measurements.

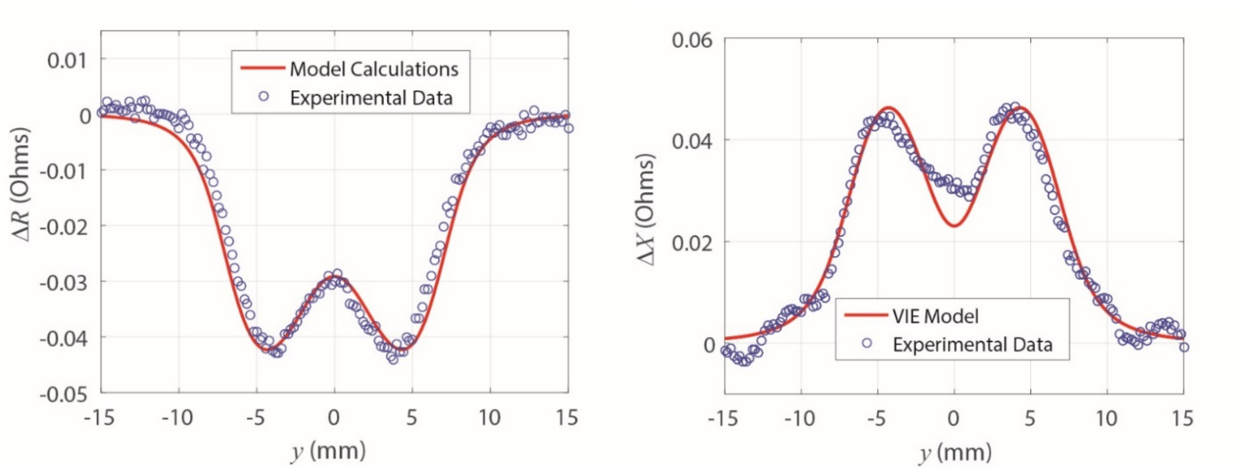

Fig 15: Variation of coil resistance and reactance as it traverses a notch in the notch plane: comparison of model predictions and experimental measurements.

The model predictions of the resistive and reactive response acquired over a rectangular area with the notch at its center are shown in the form of a color coded contour maps in Figs. 16 through 20. *Figs. Fig. 16* and *Fig. 18* show the characteristic four lobe response of a flaw in a ferromagnetic material of resistive and reactive components respectively, using material properties of 440 SS to compute the data. *Fig. 17* and *Fig.19*, respectively resistive and reactive components, shows the results for austenitic steel.

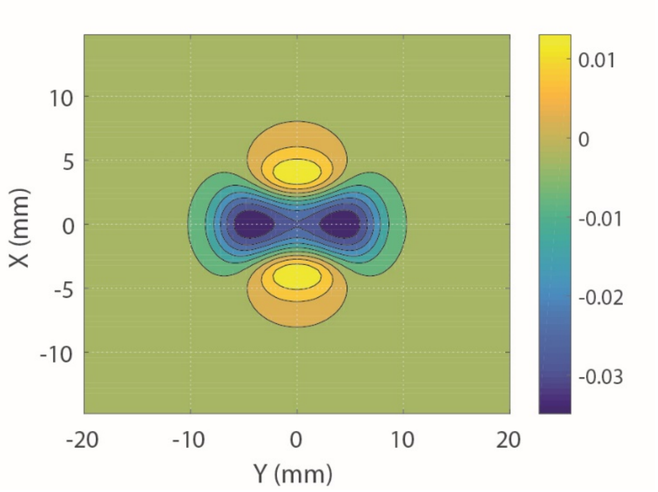

Fig. 16 Model prediction for the variation of the resistive component of the coil impedance change with position. For a ferromagnetic specimen, relative permeability 70.3 and conductivity 1.41 MS/m, with an 8 mm semi-elliptical notch. The frequency of the inspection is 5.0 kHz.

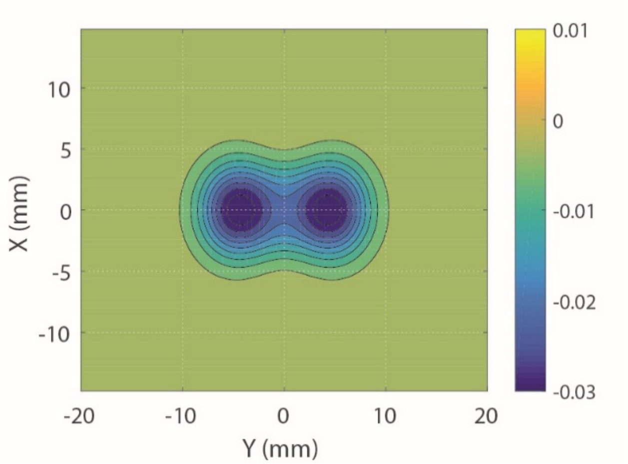

Fig 17: Model prediction for the variation of the resistive component of the coil impedance change with position. For an austenitic steel specimen, relative permeability 1.0 and conductivity 1.41 MS/m, with an 8 mm semi-elliptical notch. The frequency of the inspection is 5.0 kHz.

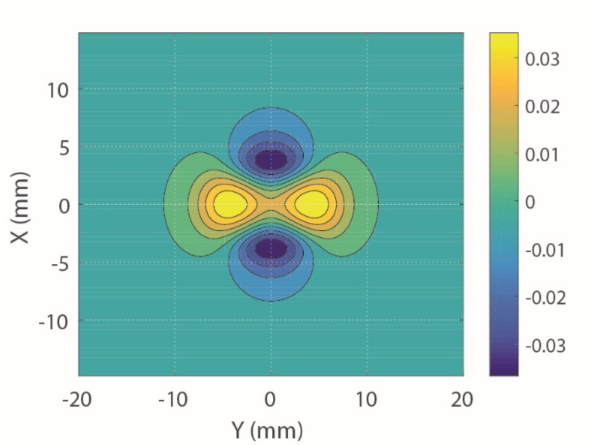

Fig. 18: Model prediction for the variation of the reactive component of the coil impedance change with position. For a ferromagnetic specimen, relative permeability 70.3 and conductivity 1.41 MS/m, with an 8 mm semi-elliptical notch. The frequency of the inspection is 5.0 kHz.

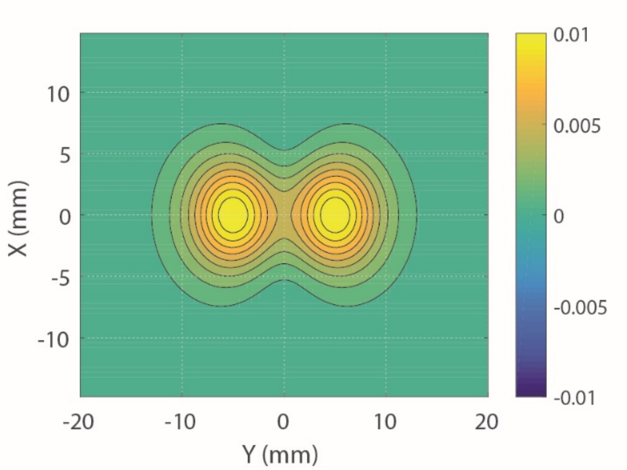

Fig 19: Model prediction for the variation of the reactive component of the coil impedance change with position. For an austenitic steel specimen, relative permeability 1.0 and conductivity 1.41 MS/m, with an 8 mm semi-elliptical notch. The frequency of the inspection is 5.0 kHz.

The four-lobe pattern of the ferritic steel response is characteristic of a probe-flaw interaction which is predominantly an electric interaction when the probe coil axis is in the plane of the flaw but magnetic when the probe is moved away from the flaw in a direction perpendicular to this plane. With the coil axis passing through the notch center, the induced electric current circulates such that the natural current flow is normal to the notch plane and is therefore strongly disrupted by the flaw. The magnetic flux in this case is tangential to the flaw and is not significantly disrupted. As the probe coil axis is moved off the flaw in a direction perpendicular to the flaw plane, the electric field approaches a point where it is tangential to the flaw surface while the magnetic field, which is in the radial direction at the surface of the plate, tends towards being perpendicular to the plane of the flaw. Hence the rolls of the two interactions become reversed when testing a ferromagnetic material. The magnetic interaction initially increases and the electric interaction decreases as the coil axis is move away from the center of the flaw.

4.2 Measurements on an immersed plate with a notch.

A fundamental question that is considered in this work is how much in the eddy current signal due to a flaw is suppressed by the effect of a liquid metal covering the flawed metal surface.

		Material properties of test specimens		
Material	**Young's Elastic Mod. (GPa)**	Density (Kg/ m^3)	Relative Permeability	Conductivity MS/m
316 SS	198 (Ref. 3)	8000	1.003-1.05	1.334 (Ref. 1)
304 SS	200 (Ref. 3)	8030	1.003-1.05	1.450 (Ref. 1)
440 SS	200	7650 (Ref 2)	62 (max)	1.667 (Ref 2)

Table 7

http://hypertextbook.com/facts/2006/UmranUgur.shtml
http://www.azom.com/article.aspx?ArticleID=1024
http://web.ornl.gov/info/reports/1979/3445605704100.pdf

The eddy current measurement on the chosen notch in air yielded the results shown in *Fig. 20* and *Fig. 21*. With a layer of liquid metal, gallium-indium-tin, between the probe base and the flaw signal was reduced as shown in *Fig. 22* and *Fig. 23*. The overall effect of the liquid metal in this case was to reduce the magnitude of the resistive component signal variation by a factor of 5 and the reactive part by a factor roughly 15. In this case the lift-off, defined as the distance between the base of the coil and the surface of the metal was 1.53 mm and measurements were made on a 440 SS plate.

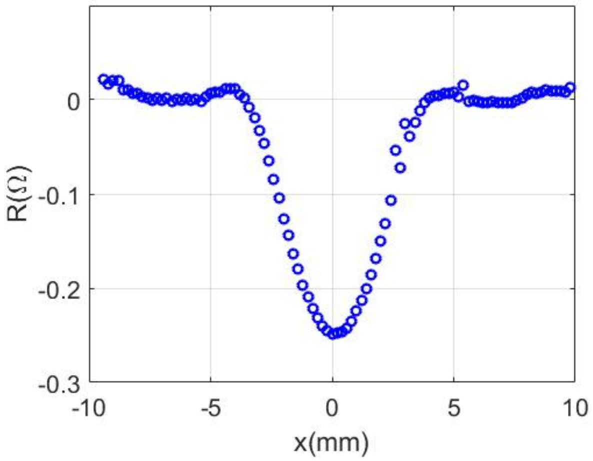

Figure 20: The resistance part of impedance variation at 50 kHz in the absence of liquid metal

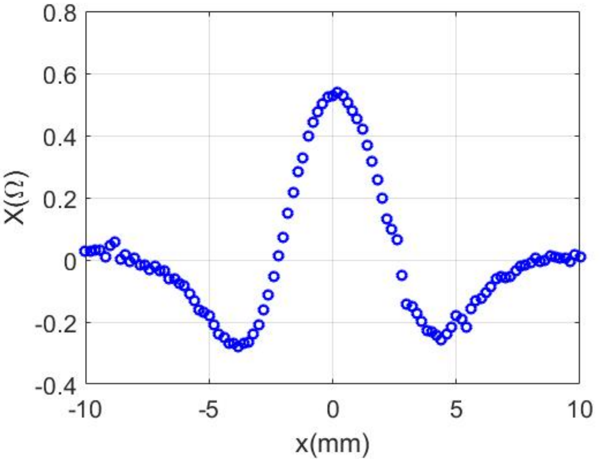

Figure 21: The reactance part of impedance variation at 50 kHz in the absence of liquid metal.

Liquid Ingredient:	**CAS#**:	**%**:	**EC#**:
Gallium	7440-55-3	66.5	231-163-8
Indium	7440-74-6	20.5	231-180-0
Tin	7440-31-5	13	231-141-8

Table 8: Liquid metal composition. CAS# is the Chemical Abstracts Service reference number

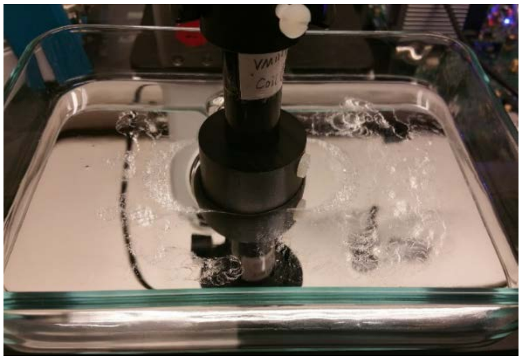

Figure 21: Liquid indium-gallium-tin covering a test specimen with a simulated crack.

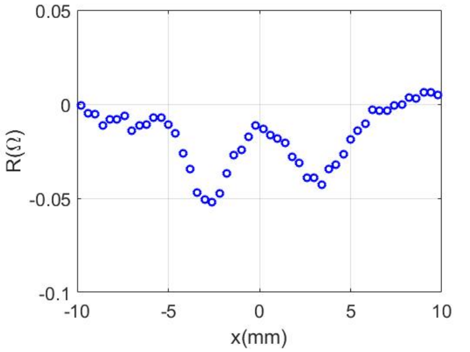

Figure 22: The resistance part of the probe impedance variation at 50 kHz in the presence of liquid metal.

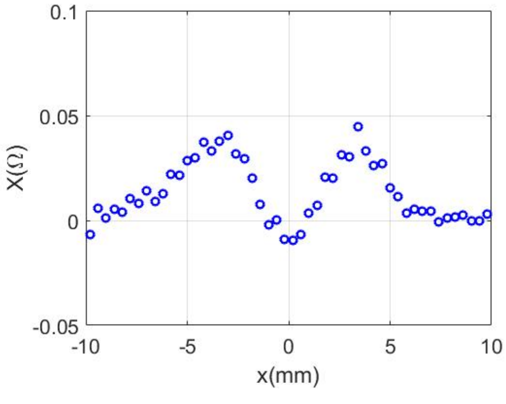

Figure 23: The reactance part of the probe impedance variation due to a notch in liquid metal measure at 50 kHz in the presence of liquid metal.

5 Probability of detection study

Of value in assessing a level of confidence in reactor inspection can be obtained from estimates of the probability of detection (PoD) of a given defect from the inspection conditions that prevail under standby conditions in a fast reactor. That goal is not within our reach since we can only draw conclusions from laboratory experiment. We can at least provide some insight into the procedures needed and the limitations of an inspection in the presence of conductive coolant. This has be done by carrying out a study using eddy current test measurements on a single notch immersed our surrogate liquid metal, Fig 21 with the probe lift-off value as a variable. This is not the standard way of presenting PoD data which usually is based on a relationship with flaw size but it has the advantage that it quantifies detection probability of an eddy current inspection of a sample under liquid metal.

An extensive study would include several notches and attempt to determine the probability of detection as a function of all key variables but this not usually done. Instead we follow a one variable analysis and write the detection probability as $\mathrm{PoD}(y(x))$. In this case, we access probability as a function of the probe lift-off, x, via a chosen function $y(x)$.

Fig. 23 and *Fig. 24,* show the data captured with a substantial lift-off. In both cases it is possible to respond to the question of the flaw detectability positively. The data set that is used contains images that are indistinct and some where there is no sign of a flaw present.

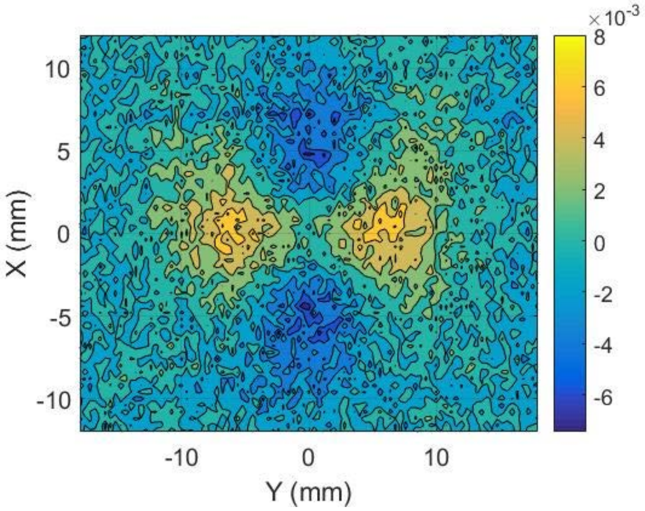

Figure 23: The imaginary part of impedance variation contour with liftoff No.5

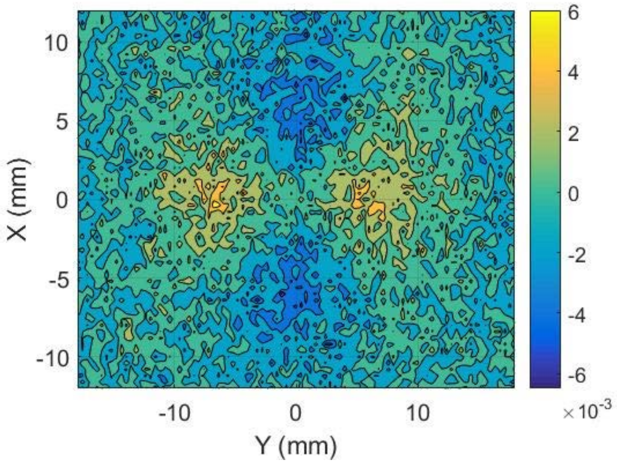

Figure 24: The imaginary part of impedance variation contour with liftoff No.6

In a typical binary regression probability with a single variable, the PoD can be chosen to have the form [21, 22]

$$PoD(y) = \frac{\exp(\beta_0 + \beta_1 y)}{1+\exp(\beta_0 + \beta_1 y)} \qquad (1)$$

Where β_0 and β_1 are regression coefficients for a binary model system. These are found from a suitably large set of binary data from the operator. In this case, the probability of detection will tend to 1 as y tends to infinity, with β_1 a positive real number. This is plausible if $y(x) = 1/x$, because it implies that the detection probability is 1.0 if the lift-off, x, is zero. On the other hand, we need the detection probability to go to zero as $x \to \infty$ and as hence $y(x) \to 0$.

This implies that $\exp(\beta_0) \ll 1$.The coefficients can be estimated as the well-known linear regression estimates [21, 22] gives rise to the probability of detection curve shown in *Fig. 26*.

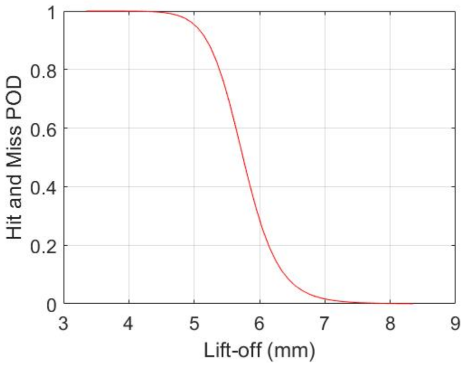

Figure 26: The PoD log regression estimate as a function of liftoff.

The 8 mm long flaw, Fig A2 (Appendix) that we used for the test can easily be detected even with a substantial lift off. We plan to repeat the process for other flaws as part of a follow up to the current program which will lead some new publications based. Some further comments on the direction that probability of detection should take are given in the following conclusion.

6 Conclusions

Using well-characterized eddy current probes, we have performed a number of controlled experiments to determine the impedance variation of the probes due to notches in austenitic and ferromagnetic steel specimens. Although much of the steel that is used in a sodium cooled fast reactor is austenitic, some components are likely to be ferromagnetic including, for example, fuel cladding and possibly heat exchanger tubing.

In assessing probability of detection we have carried out a limited demonstration since the numerical results we can gather can only be indicative and clearly do not reflect all conditions found in a liquid metal reactor under standby conditions. The indications are that eddy current testing can be used to detect immersed flaws and especially if the probe lift-off is small. The detectable flaws may be of the order of 1 mm or less, again dependent on lift-off.

The measurement system we have developed consists of a commercial high performance lock-in amplifier with our own add-on circuit for obtaining the current through the probe as well as the voltage across it. It is calibrated to measure probe impedance changes due to flaws which enables us to make measurement on known flaws and check that model predictions are correct by comparison with experiment. In addition, it is possible to determine the size and shape of a flaw from impedance measurement by using a solution procedure to the inverse problem. This process can be used to determine the length depth and opening of a flaw or the overall shape.

In a practical situation the inspections have to be carried on a time-scale that is likely to be highly limited but it would be possible to use an automated flaw analysis that (1) identifies flaws objectively (2) determines an estimate of the flaw parameters with error bounds by using model based inversion techniques [23]. The prior knowledge and data require could be established as data is gathered for estimating probability of detection in a realistic setting.

REFERENCES

1. http://www.theenergycollective.com/dan-yurman/2406166/nrc-license-sought-geh-prism-advanced-reactor.

2. T. Yamaguchi and O Mihalachi Development of a hybrid ECT sensor for the Japan sodium cooled fast reactor steam generator double-wall tubes, Journal of Nuclear Science and Technology Vol. 54 Issue 11 2017.

3. Tao Wu and John R. Bowler, Evaluation of eddy-current probe signals due to cracks in ferromagnetic parts of fast reactor Tao Wu, and John R. Bowler, AIP Conference Proceedings 1806, 110001 (2017).

4. https://www.zhinst.com/

5. https://www.keysight.com/en/pc-1000000382%3Aepsg%3Apgr/impedance-analyzers?cc=US&lc=eng

6. Tao Wu and John R. Bowler, *Limitations of eddy current testing in a fast reactor environment*, Review of Quantitative NDE, AIP Conference Proceedings, 1706, 170007, Eds. D. E. Chimenti, L. J. Bond (2016).

7. https://www.comsol.com/

8. N. Bowler, Y. Huang, Model-based characterization of homogeneous metal plates by four-point alternating current potential drop measurements, IEEE Transactions on, Magnetics, 41, pp.2102–2110, 2005.

9. N. Bowler, *Theory of four-point alternating current potential drop measurements on a metal half-space*, Journal of Physics D: Applied Physics, 39, 2006a 584–589, 2006.

10. J.R. Bowler, N. Bowler, *Theory of four point alternating current potential drop on conducting plates*, Proceedings of the Royal Society Volume: 463 Issue: 2079 817-836, March 2007.

11. **S**tructural Materials for Generation IV Nuclear Reactors, edited by Pascal Yvon.

12. S. Ukai, M, Harada, H. Okada, M. Inoue, T. Nishida and M. Fujiwara, *Alloying design of oxide dispersion strengthened ferritic steel for long life FBRs core materials*, Journal of Nuclear Materials 204, 6.5-73, (1993).

13. H.Fukutomi and M.Nishikawa, *Remote field eddy current technique applied to non-magnetic steam generator tubes*, NDT & E International,Volume 34, Issue 1, January 2001, Pages 17-23

14. Noriyasu Kobayashi, Souichi Ueno, Satoshi Nagai, Makoto Ochiai, Noboru Jimbo, *Remote field eddy current testing for steam generator inspection of fast reactor*, Nuclear Engineering and Design**,** Vol. 241, No. 12, pp 4643–4648, Dec. 2011.

15. Xiaojie Xu 1, Ming Liu, Zhanbin Zhang and Yueling Jia, A Novel High Sensitivity Sensor for Remote Field Eddy Current Non-Destructive Testing Based on Orthogonal Magnetic Field, Sensors 14, 24098-24115, 2014.

16. John R. Bowler and Tao Wu, *Eddy current tube inspection using a rotary probe*, Review of Quantitative NDE, AIP Conference Proceedings, 1706, 090009, Eds. D. E. Chimenti, L. J. Bond (2016).

17. Tao Wu and John R. Bowler, *Electromagnetic Modeling of Flaw Detection in Ferromagnetic Metal Slab by Volume Integral Equation Formulation*, Review of Quantitative NDE, AIP Conference Proceedings, Eds. D. E. Chimenti, L. J. Bond (2017).

18. Tao Wu and John R. Bowler, *Electromagnetic Modeling of an Eddy-Current Position Sensor for Use in a Fast Reactor*, Review of Quantitative NDE, AIP Conference Proceedings, Eds. D. E. Chimenti, L. J. Bond (2017).
19. Tao Wu and John R. Bowler, *Ferromagnetic, integral equation, moment method, eddy current, scalar decomposition, slab, nondestructive evaluation,* to be published.
20. https://www.mag-inc.com/Design/Design-Guides/Designing-with-Magnetic-Cores-at-High-Temperatures
21. M Li and W Q Meeker, *A Noise Interference Model for Estimating Probability of Detection for nondestructive Evaluations*, Review of Quantitative NDE, Donald O Thompson and Dale E Chimenti Eds., AIP conference proceedings , p.1769-1776, Vol.1096 (1), 2009.
22. Ming Li, William Q. Meeker, and Peter Hovey, *Joint Estimation of NDE Inspection Capability and Flaw-Size Distribution for In-Service Aircraft Inspections,* Research in Nondestructive Evaluation Vol. 2, 2012.
23. Stephen J. Norton and John R. Bowler, *Theory of eddy current inversion,* Journal of Applied Physics **73**, 501 (1993).

7. Project publications

1. Quddes, M.R., Bond L.J. and Bowler, J.R., "**Numerical Study of Eddy Current Flaw Detection Techniques in Liquid Metal Reactor**" Transactions of the American Nuclear Society, **111**, pp 624-626 (2014).
2. Quddes, M.R., Bond L.J. and Bowler, J.R., "**Measurement Challenges due to the Noise Effect for an Eddy Current Probe**" Proc. 9th International Conference on Nuclear Plant Instrumentation, Control & Human-Machine Interface Technologies (NPIC & HMIT), February 23-26, 2015, Charlotte, North Carolina, American Nuclear Society [in press] (2015).
3. Bowler, J. R., Wu, T., Xie, H. and Ji, Y., **Eddy Current Tube Inspection Simulation Using a Rotary Probes**, Proceedings of the Review of Progress in Quantitative Nondestructive Evaluation, 2016,
4. Bowler, J. R. and Wu T., **Limitations of Eddy Current Testing in a Fast Reactor Environment**, Review of Progress in Quantitative Nondestructive Evaluation, 2016.
5. Bilgunde, P. N., & Bond, L. J. (2015). **A 2D finite element simulation of liquid coupled ultrasonic NDT system**. Proc. *41ST ANNUAL REVIEW OF PROGRESS IN QUANTITATIVE NONDESTRUCTIVE EVALUATION: Volume 34* (Vol. 1650, pp. 1543–1552). AIP Publishing. doi:10.1063/1.4914773.
6. Bilgunde, P. N. and Bond, L. J., "**Analysis of High Temperature Ultrasonic Transducer Performance in Small Modular Reactors,**" Proc., NPIC & HMIT 2015 Conference, February 23–26, 2015, Charlotte, North Carolina, American Nuclear Society (2015).

7. Bilgunde, P. N. and Bond, L. J., "**Effect of Thermal Degradation on High Temperature Ultrasonic Transducer Performance in Small Modular Reactors**" 2015 International Congress on Ultrasonics, 2015 ICU Metz, May 10–14, 2015, Metz, France, Physics Procedia (2015).

Journal Article Submitted:

1. Wu T and Bowler, J. R. **Impedance of a Circular Coil of Arbitrary Orientation in a Tube,** submitted J. Phys. Comm.

Journal Articles in Preparation

1. Wu T and Bowler, J. R., **Impedance of a Circular Coil of Arbitrary Orientation in a Tube,** IEEE Sensors Journal.

2. Xie, H., Ji Y. and Bowler, J.R. **Eddy Current Coil Impedance Changes due to Flaws in Tubes,** J. Appl. Phys. IEEE Sensors Journal.

Appendix

Eddy Current Test Specimens with Simulated Cracks

These specimens are being used in ongoing work for testing, inversion and model validation for publications in 2018.

Actual dimensions of the simulated cracks in the form of spark eroded notches, have been calculated and recorded with the use of an Optical Comparator ID No. 146011789 which is traceable to the National Institute of Standards and Technology (NIST).

Item	*Specimen Ref.*	*Material*	*Dimensions (mm)*	*Tube Notch Type* *I internal X external* *L Longitudinal* *T Transverse*	*Length and depth of notches (mm)*	*Notch Width (mm)*
1	*NEUP316-P1*	*316 SS plate*	*100 x 100 x 12.5*	*rectangle*	*100 x 0.498* *100 x 1.006* *100 x 1.988*	*0.184* *0.186* *0.192*
2	*NEUP304-P1*	*304 SS plate*	*100 x 100 x 12.5*	*rectangle*	*100 x 0.498* *100 x 1.008* *100 x 2.024*	*0.208* *0.204* *0.210*
3	*NEUP-TA1*	*304 SS tube*	*100 x 25 OD x 21 ID*	*Semi-ellipse IL*	*6.0274x 1.4961*	*0.1702*
4	*NEUP-TA2*	*304 SS tube*	*100 x 25 OD x 21 ID*	*Semi-ellipse XL*	*6.0681x 1.5318*	*0.2438*
5	*NEUP-TA3*	*304 SS tube*	*100 x 25 OD x 21 ID*	*Semi-ellipse IT*	*6.0935x 1.4986*	*0.1473*
6	*NEUP-TF1*	*440 SS tube*	*100 x 25 OD x 21 ID*	*Semi-ellipse IL*	*6.0300x 1.4961*	*0.1651*
7	*NEUP-TF2*	*440 SS tube*	*100 x 25OD x 21 ID*	*Semi-ellipse XL*	*6.0647 x 1.5063*	*0.2337*
8	*NEUP-TF3*	*440 SS tube*	*100 x 25OD x 21 ID*	*Semi-ellipse XT*	*6.0325 x 1.4935*	*0.1346*

Table A1: Plate and tube specimens and notch dimensions.

TA1

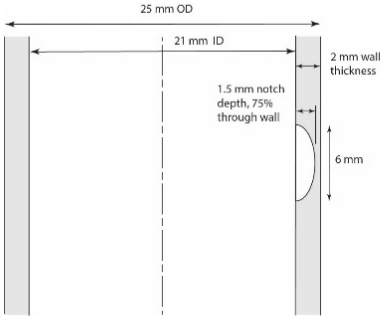

TA2

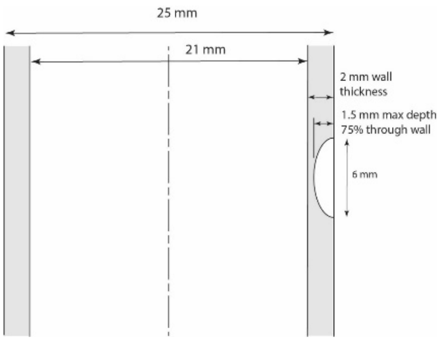

TA3

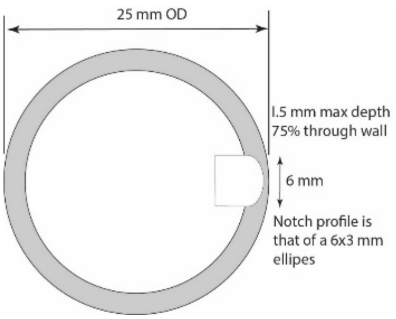

Figure A1: Test specimens TA1, TA2 and TA3, are SS 304, 10 cm tubes 25 mm OD and 2 mm wall thickness.

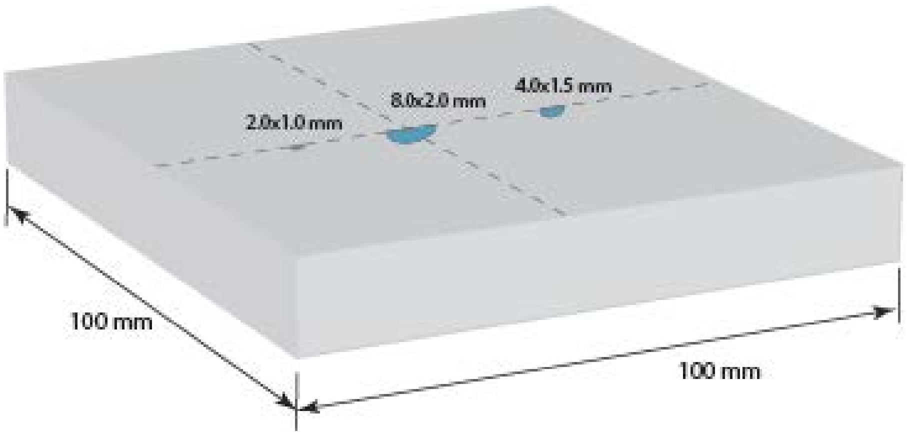

Figure A2: PoD Test specimen CRC_F_3_4_5. This is a 1.25 cm thick plate in SS 440 with 3 notches as shown. The 8 mm notch was used in the PoD test.

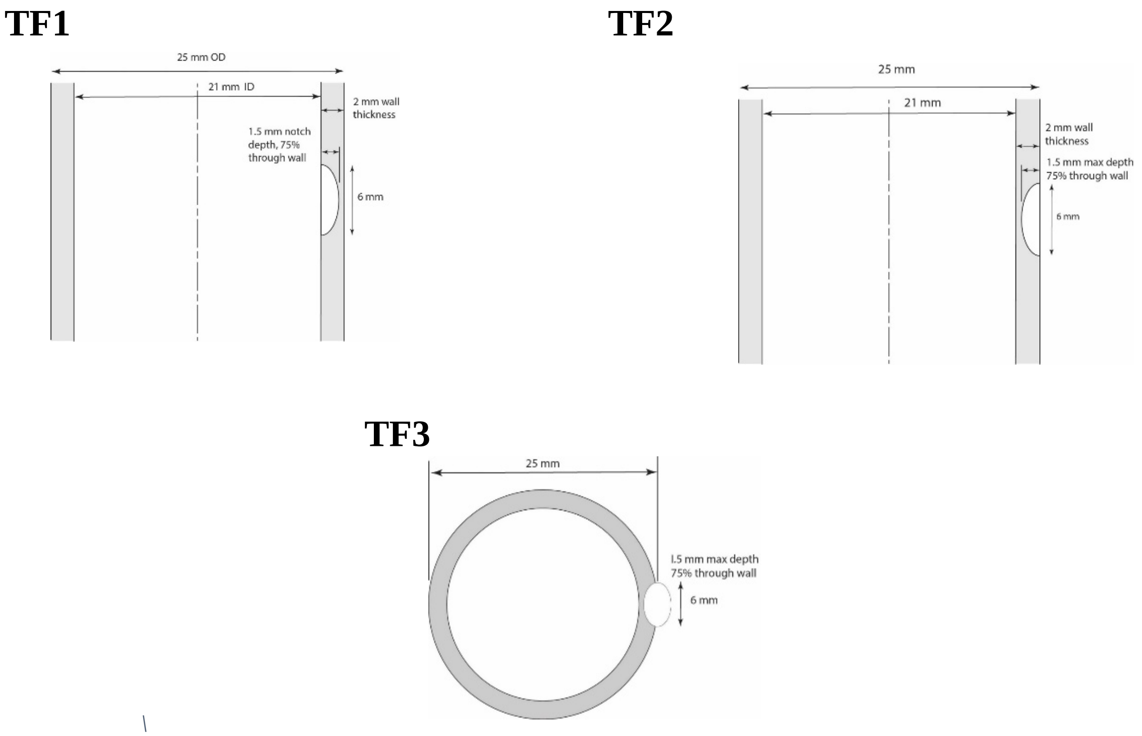

Figure A3: Test specimen TF1, TF2 and TF3, are SS 304, 10 cm tubes 25 mm OD and 2 mm wall thickness.

part #	Bobbin ID (mm)	Coil ID (mm)	Bobbin OD (mm)	Coil Width W (mm)	Radial depth of windings (OD-ID)/2 (mm)	40 AWG width turns W/TD	40 AWG radial turns (OD-ID)/(2*TD)	Turns
VM110	2.11	2.54	4.95	1.93	1.21	20.00	12.50	240
VM112	4.78	5.64	9.02	1.78	1.69	18.42	17.50	306
VM113	6.05	6.60	11.56	2.16	2.48	22.37	25.66	550
VM114	7.67	8.28	14.99	2.92	3.35	30.26	34.74	1020
VM200	2.11	2.54	8.00	1.20	2.73	12.43	28.28	336

Table A2: Precision coils for eddy current probes.